fibers

Glass Fibers 2018

Edited by
Edith Mäder and Christina Scheffler

Printed Edition of the Special Issue Published in *Fibers*

www.mdpi.com/journal/fibers

MDPI

Glass Fibers 2018

Glass Fibers 2018

Special Issue Editors

Edith Mäder
Christina Scheffler

MDPI • Basel • Beijing • Wuhan • Barcelona • Belgrade

Special Issue Editors
Edith Mäder
Leibniz-Institut für Polymerforschung Dresden
Germany

Christina Scheffler
Leibniz-Institut für Polymerforschung Dresden
Germany

Editorial Office
MDPI
St. Alban-Anlage 66
4052 Basel, Switzerland

This is a reprint of articles from the Special Issue published online in the open access journal *Fibers* (ISSN 2079-6439) from 2018 to 2019 (available at: https://www.mdpi.com/journal/fibers/special_issues/glass_fibers_2018).

For citation purposes, cite each article independently as indicated on the article page online and as indicated below:

LastName, A.A.; LastName, B.B.; LastName, C.C. Article Title. *Journal Name* **Year**, *Article Number*, Page Range.

ISBN 978-3-03936-914-0 (Hbk)
ISBN 978-3-03936-915-7 (PDF)

Cover image courtesy of Leibniz-Institut für Polymerforschung Dresden.

Contents

About the Special Issue Editors

Edith Mäder worked as Scientist and Head of the Department of Composites in the Institute of Polymeric Materials of the Leibniz-Institut für Polymerforschung Dresden (IPF) until her emeritation in 2017. She is involved in education as Honorary Professor at Technische Universität Dresden, Faculty of Mechanical Engineering, Institute of Materials Science. She has obtained more than 30 years' experience in the field of material science, textiles and composites, and especially on the topics of fibre/matrix interfaces in fibre-reinforced composite materials, interphase design, multifunctional interphases, development of continuous fibre-reinforced thermoplastics based on hybrid yarns, improving the aging behaviour and enhancing the durability by interface modification (nanostructured sizing, polymeric coatings). An important focus of her work is in the surface modification of reinforcement fibres and micromechanical testing. She has (co)authored over 150 scientific papers in SCI-indexed journals and has (co)authored 14 chapters in books and more than 400 conference papers

Christina Scheffler has worked as Scientist in the Department of Composites under the supervision of Prof. Edith Mäder. She submitted her doctoral thesis (Dr.-Ing./PhD) in 2009 on the topic "Evaluation of AR-Glass Fibres in an Alkaline Environment" and became the leader of the work group Reinforcing Fibres and Interphase Characterization at Leibniz-Institut für Polymerforschung Dresden (IPF) in 2014. In 2016, she was awarded as a "Young Investigator" at the Faculty of Civil Engineering of the Technische Universität Dresden which enabled her to supervise doctoral candidates in the field of fibre-reinforced concrete. Her current interests include: modification of glass, carbon and basalt fibre surface, interphase characterization by single-fibre pull-out test, micromechanical tests, continuous glass fibre spinning, simultaneous spinning of glass/polymer filaments (hybrid yarn); commingled carbon fibre/polymer filament yarns for continuous fibre reinforced thermoplastics; mechanical performance of fibre-reinforced thermoplastics; reinforcing fibres and interphases in fibre-reinforced concrete, aging behaviour of glass fibres in an alkaline environment.

Preface to "Glass Fibers 2018"

Glass fibres are melt-spun, silica-based inorganic materials, which have been known about and comprehensively used for many years. Their main application is in glass fibre-reinforced composites, which account for more than 90% of all fibre-reinforced composites currently produced. Nevertheless, the improvement of fibres, interfaces, and composites in key areas remains a great challenge. The objective of this preprint is to focus on actual research topics related to glass fibres comprising multifunctional nanostructured surfaces, which can address anything from insulating to electrically conductive fibres and their interphases in composites that are capable of uptake under a variety of mechanical, chemical, humidity, and thermal conditions for in situ sensing and photocatalytic functions. Glass fibre size includes lubricants, binders, and/or coupling agents to help protect the filaments from failure during processing, resulting in fibres with improved wetting as well as strengthening of the adhesive bond at the fibre–matrix interphase. Graphene, as an interphase, not only improves the mechanical performance of fibre-reinforced polymer composites but also induces functional properties like electrical conductivity, thus providing the possibility of strain monitoring in real time. The piezoresistivity of the composites was monitored under flexural loading under isothermal conditions, and strain/damage monitoring was evaluated at different temperatures through the change in electrical resistance with applied strain. In composites, a strong interphase between the components is essential for determining the mechanical properties. The interphase may be varied, by suppressing or promoting heterogeneous nucleation of a thermoplastic matrix. In the latter case, three-dimensional transcrystallised interphases with properties differing from those of the bulk matrix are formed. Polypropylene–glass fibre composites are prepared as single-fibre model composites with (a) a size that either induces or suppresses the transcrystalline interphase, (b) different amounts of modifier maleic acid anhydride-grafted polypropylene, and (c) matrix polymer of different molecular weights. These are studied in quasi-static or cyclic load tests. Static tests permit insights into the interfacial characteristics, such as critical interface energy release rate, adhesion strength, and frictional stress. Cyclic tests on these model composites can be used to study the nature of dissipative processes and damage behaviour. The transcrystalline layer can indeed improve the mechanical parameters through increased strength and toughness, depending on the molecular weight of the matrix polymer at low modifier concentrations. Another study shows that chitosan could be highly useful as a coupling agent in phosphate glass fibre/polycaprolactone (PGF/PCL) composites as it improved the interfacial shear strength by up to 78%. Tensile and fragmentation tests were conducted to obtain the mechanical properties of the single fibres and interfacial properties of the PGF/PCL composites, respectively. It was observed that post-cleaning, the tensile strength of treated fibres was reduced by around 20%.Plasma-synthesized interphases, in the form of variable materials from polymer-like to glass-like films with a Young's modulus of 10–52 GPa, were deposited on unsized glass fibres used as reinforcements in glass fibre/polyester composites. Modulus mapping was successfully used to examine the mechanical properties across the interphase region on cross-sections of the model composite in order to distinguish the fibre, interphase, and modified and bulk polymer matrix. The interfacial shear strength for plasma-coated fibres in glass fibre/polyester composites, determined from the nanoindentation test, was up to 36% higher than those of commercially sized fibres. A number of analytical techniques were applied to investigate changes to the surface of unsized boron-free E-glass fibres after thermal conditioning at temperatures up to 700 °C. Novel systematic studies were carried out to investigate the fundamental strength loss

from thermal conditioning. Surface analyses were conducted using X-ray photoelectron spectroscopy and atomic force microscopy and showed a consistent increase in the surface concentration of calcium with increasing conditioning temperature as well as an increase of surface roughness. Although surface roughness did not correlate precisely with fibre strength, there was a clear inverse relationship at temperatures exceeding 400 °C

Edith Mäder, Christina Scheffler
Special Issue Editors

fibers

MDPI

Article

Temperature Dependent Strain/Damage Monitoring of Glass/Epoxy Composites with Graphene as a Piezoresistive Interphase

Haroon Mahmood [1,2,*], Andrea Dorigato [1,2] and Alessandro Pegoretti [1,2,*]

[1] Department of Industrial Engineering, University of Trento, via Sommarive 9–38123 Trento, Italy; andrea.dorigato@unitn.it

[2] National Interuniversity Consortium of Materials Science and Technology (INSTM), via Giuseppe Giusti 9–50121 Florence, Italy

* Correspondence: haroon.mahmood@unitn.it (H.M.); alessandro.pegoretti@unitn.it (A.P.); Tel.: +39-0461-283728 (H.M.); +39-0461-282452 (A.P.)

Received: 19 November 2018; Accepted: 15 February 2019; Published: 21 February 2019

Abstract: Graphene as an interphase not only improves the mechanical performance of fiber reinforced polymer composites but also induces functional properties like electrical conductivity, thus providing the possibility of strain monitoring in real time. At this aim, graphene oxide (GO) was electrophoretically deposited at different applied potentials on glass fibers to create a uniform coating and was subsequently chemically reduced to obtain a conductive layer of reduced graphene oxide (rGO). After the optimization of the deposition process, composite laminates were prepared by hand lay-up with an epoxy resin, followed by curing in vacuum bag. The deposited rGO interphase improved the dynamic moduli (storage and loss modulus), the flexural strength (+23%), and interlaminar shear strength (ILSS) (+29%) of the composites. Moreover, laminates reinforced with rGO-coated glass fibers showed an electrical resistivity in the order of ~10^1 Ω·m, with a negative temperature coefficient. The piezoresistivity of the composites was monitored under flexural loading under isothermal conditions, and strain/damage monitoring was evaluated at different temperatures through the change of the electrical resistance with the applied strain.

Keywords: composites; glass fibers; graphene; interphase; strain monitoring

1. Introduction

Structural fiber reinforced polymer composites have received wide attention from both academic and industrial communities for their advantages in several applications because of their high strength-to-weight ratio, better corrosion resistance with respect to metallic materials, excellent impact strength, and durability [1]. However, the utmost requirement that is first evaluated for the applicability of such materials is the mechanical performance, which in turn has a great dependence on the fiber/matrix interfacial adhesion. In other words, the effective load transfer from the matrix to the fibers is the primary factor on which the mechanical performance is determined [2]. Researchers are constantly looking for better design, material selection, and production systems in order to assure optimal load transfer [3]. In recent years, this issue has been successfully faced by the use of nanostructured materials dispersed in the matrix or deposited on the fiber surface, which are able to create a better interphase for the load transfer mechanism [3].

Recent years have seen an enormous rise in the use of nanomaterials in polymer composites, due to their remarkable effect on the physical properties of the resulting materials [4–9]. The inclusion of carbonaceous nanomaterials (carbon nanotubes (CNTs), graphene), for example, has successfully modified the properties of both thermoplastic and thermosetting matrices [10–12], including the

enhancement of the electrical conductivity [13–15]. In particular, the use of graphene in polymer composites could lead to the development of multifunctional materials that could be applied for innovative applications [16–18]. In the case of fiber reinforced polymer composites, several studies have been conducted to prove the positive impact of nanoparticles in enhancing the mechanical properties, either by dispersing them in the polymer matrix or depositing nanofillers on the fiber surface as a fiber/matrix interphase [3,19,20]. In the past, graphene oxide (GO) has been reported to be extremely effective in not only improving the fiber/matrix load transfer mechanism [21,22], but also in promoting the use of composite structures in strain monitoring sensors [23,24].

The topic of strain monitoring of structural materials has taken a great deal of attention in the past decade, mainly because of the possibility to obtain information about the damage evolution within the materials in real time conditions. Fiber reinforced polymer (FRP) structures, being particularly sensitive to intrinsic damage mechanisms (i.e., delamination or matrix cracking), are thus ideal candidates for real time damage monitoring and detection [25]. It is thus clear that the in-situ monitoring of damage is a useful tool to increase the reliability and lifetime of composite structures, also making the maintenance of structural components less challenging [26]. In the past, graphene has been used extensively in polymer composites. Strain monitoring sensitivities up to 16,400 were obtained by using functionalized graphene nanoplatelets as coating on glass fiber fabric [27]. Moreover, in epoxy matrix, a gauge factor of around 750 was achieved by the addition of graphene nanoplatelets (GNPs) [24]. Similarly, it was proven that functionalized graphene in polyvinylidene fluoride (PVDF) performed better as a strain sensor compared to carbon nanotube polymer composite [28].

Recently, fiber reinforced polymer composites have been developed using various "built-in sensors" that have the capability to monitor their structural health [26]. In particular, carbon fibers have been used as a multifunctional element, primarily for their structural capabilities as well as for their elevated electrical conductivity, which qualifies the composite itself for damage monitoring by the phenomenon of piezoresistivity, i.e. the change of electrical resistance of an element due to an application of a certain stress (or strain) [29]. In this sense, the use of glass fibers (GF) reinforced laminates for these applications is strongly limited, because of the intrinsic insulating properties of both the fibers and the polymer matrix. To achieve elevated electrical conductivity in glass fiber-based composites, several techniques have been utilized in the past [30–33]. Böger et. al [34] dispersed carbonaceous nanofillers in an epoxy matrix to perform load and strain monitoring of glass/epoxy composites. In the same way, Gao et. al [35] utilized multi-walled carbon nanotubes in an epoxy matrix reinforced with glass fibers, in order to evaluate the mechanisms of damage sensing under cyclic loading conditions. The difficulty in the dispersion of nanofillers in epoxy matrix arises from the fact that an increase of the nanofiller loading causes an increase in the viscosity [36,37], thus leading to processability problems that could potentially impair the mechanical performances of the resulting materials [38].

In order to overcome these problems, researchers tried to implement a selective deposition of nanofillers on the fiber surface through various techniques, such as dip coating [27], chemical vapor deposition (CVD) [39], chemical grafting [40], and electrophoretic deposition (EPD) [41]. EPD has recently proved to be a practical technique when depositing large amounts of nanosized particles on various substrates [42–44]. In a recent work, Mahmood et al. [25] investigated the strain monitoring capability of glass/epoxy composites, in which a graphene interphase was created between the matrix and the reinforcement through EPD, starting from a GO water suspension with a concentration of 1 mg/mL (equivalent to 0.1 wt%), deposited applying an electrical field of 10 V/cm. GO was then chemically reduced to reduced graphene oxide (rGO) by lowering the oxygen content as low as 10% in the rGO sheets. Such continuous deposition on GF provided an improvement of about 70% of the fiber/matrix interfacial shear strength. Interestingly, the produced rGO based epoxy/glass composites were characterized by a volume resistivity as low as 4.5 Ω·m. However, in that work, the process parameters of the EPD were not optimized, and their influence on the physical properties of the coating and of the resulting composites was not determined.

On the basis of these considerations, the current work is focused on the investigation of the optimal parameters of the EPD technology (applied electric field and concentration of GO dispersion required to create a uniform and continuous deposition of rGO on GF), to develop electrically conductive glass/epoxy composites. Moreover, considering that no papers can be found in the literature on the temperature-dependent health monitoring capability of nanomodified hybrid epoxy composites, the piezoresistive response of the resulting laminates at three different temperatures (i.e., 0 °C, 23 °C, and 50 °C) was investigated.

2. Materials and Methods

2.1. Materials

A dispersion of 4 mg/mL of graphene oxide in water was purchased from Graphenea SA (San Sebastian, Spain). According to the producer's datasheet, this dispersion has a GO monolayer content of more than 95%. A unidirectional fabric of glass fibers (UT-E500), having a surface density of 500 g/m^2, was provided by Gurit (Wattwil, Switzerland). A bicomponent epoxy resin, constituted by an epoxy base (EC157) and an aminic hardener (W342), was provided by Elantas Europe Srl (Parma, Italy). As reported in the producer's datasheet, this system presents a glass transition temperature (T_g) of around 88 °C after a curing cycle of 24 h at room temperature, followed by 15 h at 60 °C. All the materials were used as received.

2.2. Samples Preparation

In the electrophoretic deposition (EPD) process, two electrodes were inserted in a conductive suspension and connected together using a direct current power supply. GF were mounted on a steel frame (as shown in Figure 1a) and were placed in front of the anode during EPD, due to the fact that GO is negatively charged.

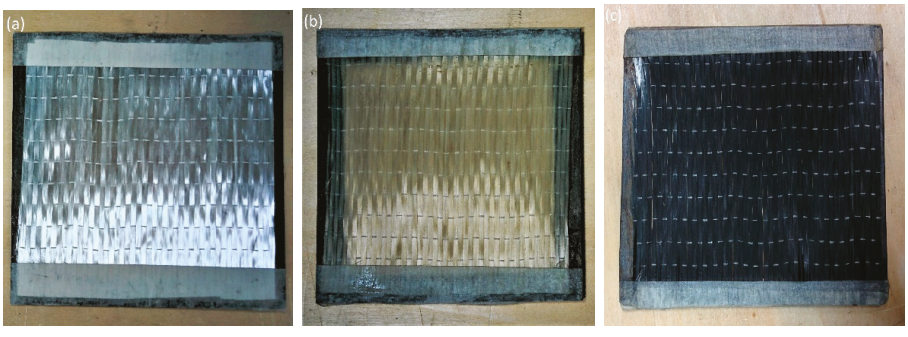

Figure 1. Representative images of glass fibers (GF) (**a**) as received, (**b**) after the EPD process, and (**c**) after chemical reduction.

Through the application of an electrical potential between the electrodes, GO is forced to migrate towards the anode, thus depositing on the GF. In order to optimize the EPD parameters, various concentrations of GO solution (ranging from 0.005 wt% to 0.02 wt%) and different electric field intensities (from 0.5 to 1.5 V/cm) were applied. In this work, the electric field intensity was defined as the ratio between the voltage applied and the distance between the electrodes. During the EPD process, the distance between the electrodes was kept constant at 2 cm, and both sides of the glass fiber fabric were treated for 5 min. The configuration of the experimental equipment used in the EPD treatment was taken from the previous work of Mahmood et al. [25], in order to directly compare the results, while the deposition conditions (i.e., GO concentration and applied electric field) were

systematically modified. The complete list of the conditions of the electrophoretic deposition of GO on glass fibers is reported in Table 1.

Table 1. Conditions of electrophoretic deposition of graphene oxide (GO) on glass fibers.

Code.	GO Concentration in Water (wt%)	Applied Electric Field (V/cm)
0A	0.005	0.5
0B	0.005	1.0
0C	0.005	1.5
1A	0.01	0.5
1B	0.01	1.0
1C	0.01	1.5
2A	0.02	0.5
2B	0.02	1.0
2C	0.02	1.5

After the deposition, the GO-coated fibers were dried in an oven under vacuum at 50 °C for at least 12 h. The surface appearance of both uncoated and coated fabrics can be observed in Figure 1a,b, respectively. The treated fibers were then subjected to chemical reduction in an environment of hydrazine hydrate at 100 °C for 24 h to reduce GO to rGO. The details of the chemical reduction process can be found in the previous work of Mahmood et al. [25]. Regardless of the adopted parameters, the color of the fibers passed from light brown to black (Figure 1c) after the chemical reduction.

Both uncoated and rGO-coated fibers were used to fabricate unidirectional composites, with the epoxy resin as matrix. A hand lay-up method was adopted, stacking 4 laminae of the glass fabric. The system was then placed in a vacuum bag to remove the air bubbles and the excess resin. The curing process was performed according to the indications of the producer (i.e., 24 h at ambient temperature followed by 15 h at 60 °C). In this way, laminates having a dimension of 150 mm × 150 mm × 1.3 mm were prepared. On the other hand, for the short beam shear test (SBS), 12 laminas were stacked to create a thicker composite specimens (thickness of about 3.7 mm). The neat epoxy resin was designed as EP and the uncoated GF reinforced composite was denoted as EP-GF, while the laminate reinforced with rGO-coated fibers were coded as EP-rGO-GF. It is important to underline that, in the preparation of the composites, only the fibers coated with an optimized EPD condition (i.e., 2A of Table 1) were used.

2.3. Experimental Techniques

2.3.1. Characterization of the Fibers

The morphological analysis of both the uncoated and coated fibers was performed by scanning electron microscopy (SEM) using a Zeiss Supra 40 microscope (Zeiss, Oberkochen, Germany). Before observations, specimens were coated by a platinum/palladium alloy (80:20) thin layer with a thickness of about 5 nm.

Based on the electrical resistivity values of the investigated materials, two different resistivity measurement methods were utilized. For uncoated GF, whose resistivity level exceeds 10^5 Ω·m, the electrical resistivity was measured using a Keithley 8009 resistivity test chamber (Keithley Instruments, Cleveland, OH, USA) coupled with a Keithley 6517A high-resistance meter (Keithley Instruments, Cleveland, OH, USA) at 5 V applied voltage. On the other hand, the electrical resistivity at 23 °C of rGO-coated fibers at different EPD conditions was measured by using a Keithley 6517A electrometer in 4-point configuration (Keithley Instruments, Cleveland, OH, USA). Three different fiber strands (width 0.7 cm, length 4 cm) were tested for each sample, applying voltage levels from 0.1 V to 5 V (depending on the electrical resistivity of the fibers).

2.3.2. Characterization of the Composites

The density of the neat epoxy matrix and of the composites was measured at 23 °C by using a precision balance (Archimede Gibertini E42, Gibertini, Modena, Italy) which had a sensitivity of 10^{-4} g. The specimens were weighed in air and in ethanol, according to the ASTM standard D792-13. The density of the GF was measured by using a Micromeritics® Accupyc 1330 helium pycnometer (Micromeritics Instrument Corporation, Norcross, GA, USA) at ambient temperature 23 °C, using a testing chamber of 3.5 cm^3.

The fiber volume fraction (V_f) in the composites was evaluated by using the expression reported in the following Equation (1):

$$V_f = \frac{1}{1 + \frac{\rho_f}{\rho_m}\left(\frac{1}{W_f} - 1\right)} \quad (1)$$

where ρ_f and ρ_m are the densities of the fiber and matrix, while W_f is the fiber weight fraction.

The theoretical density (ρ_t) of the composite specimens was then estimated using Equation (2):

$$\rho_t = \rho_f \cdot V_f - \rho_m \cdot V_m \quad (2)$$

where V_m represents the matrix volume fraction.

It is possible to also estimate the volume fraction of the voids (θ_{voids}) in the specimen using Equation (3):

$$\theta_{voids} = \frac{\rho_t - \rho_{exp}}{\rho_t} \quad (3)$$

Optical microscope images of the cross section of the composite laminates were obtained through a Zeiss Axiophot optical microscope (EL-Einsatz 451887, Zeiss, Oberkochen, Germany), equipped with a Leica DC300 digital camera (Leica Microsystems Ltd., Heerbrugg, Switzerland). The specimens were polished using abrasive grinding papers with grit size P800, P1200, and P4000, sequentially.

The thermal stability of epoxy and glass/epoxy composites was assessed through thermogravimetric analysis (TGA) by using a Q5000IR thermobalance by TA Instruments (New Castle, DE, USA). Around 10 mg and 40 mg of the neat epoxy and of the composites were tested respectively, under a nitrogen flow of 100 mL/min. The tests were conducted between 25 °C and 700 °C, at a heating rate of 10 °C/min. The onset degradation temperature (T_{onset}) was computed by the intersection of the extrapolated TGA curve and the tangent line of the curve. Temperature corresponding to a weight loss of 5% ($T_{5\%}$) was also determined. The degradation temperature (T_d) was taken as the temperature associated with the maximum mass loss rate, and the residual mass at 700 °C (r_m) was also detected.

The viscoelastic behaviour of the composites was evaluated through dynamical mechanical analysis (DMA), by using a DMAQ800 machine, provided by TA instruments (New Castle, DE, USA), operating in dual–cantilever mode. Analysis was carried out in a temperature range between 0 and 150 °C at a heating rate of 3 °C/min and a frequency of 1 Hz.

Flexural mechanical properties of the composite laminates were determined by using an Instron® 5696 universal testing machine (Instron, Norwood, MA, USA), according to ASTM D790 standard. Rectangular specimens with dimension of 150 mm × 13 mm × 1.3 mm were tested, imposing a span to depth ratio of 60:1 and 40:1 for the measurement of flexural modulus and flexural strength, respectively. In order to apply a strain rate of 0.01 mm^{-1}, cross-head speeds of 7.8 mm/min for flexural modulus evaluation and 3.5 mm/min for flexural strength tests were selected. At least five specimens were tested for each composition. Interlaminar shear strength (ILSS) values of the composites were determined through a Short Beam Shear test (SBS), performed according to the ASTM D2344 standard, by using an Instron® 5969 tensile testing machine. Specimens with dimensions of 22.2 mm × 7.4 mm × 3.7 mm were tested under 3-point bending configuration at a speed of 1 mm/min. The ILSS was

determined from the maximum load sustained by the samples (F_{max}), by using the expression reported in the following Equation (4):

$$\text{ILSS} = 0.75 \times \frac{F_{max}}{b \times h} \quad (4)$$

where b and h are the width and the height of the specimens, respectively.

The electrical volume resistivity of the EP-rGO-GF composites was tested through a 6-1/2-digit electrometer (Keithley model 6517A) in a 2-point configuration at three different temperatures (0 °C, 23 °C, and 50 °C) under an applied voltage of 10 V. At least five specimens were tested for each composition. The piezoresistivity of the EP-rGO-GF composite was measured under flexural loading at three different temperatures (i.e., 0 °C, 23 °C, and 50 °C) by using an Instron® 5969 tensile testing machine. Rectangular samples with dimensions of 150 mm × 13 mm × 1.3 mm were mechanically tested at 3.5 mm/min, simultaneously measuring the electrical resistance through a Keithley 6517A electrometer under 2 contact points, setting a distance between the electrodes of 30 mm [25]. The temperature was controlled during the tests by conducting the experiments in a thermostatic chamber. The piezoresitivity of the EP-rGO-GF laminate was thus assessed through the variation of the relative electrical resistance ($\Delta R/R_0$, where R_0 is the initial resistance at the beginning of the test) as a function of the applied flexural strain.

3. Results and Discussion

3.1. Characterization of the Fibers

The electrical resistivity of the rGO-coated fabric was measured under a 4-point configuration, and the most important results are summarized in Table 2. It can be observed that by applying a higher electric field and/or by using a higher GO concentration, it is possible to reach a decrease of resistivity. With a GO concentration of 0.005 wt% (0A–0C fibers), it is possible to obtain a resistivity in the order of ~10^3 Ω·m, while by increasing the GO amount up to 0.01 wt%, it is possible to produce fibers with a resistivity of ~10^2 Ω·m, especially when increasing the applied voltage. A further enhancement of the GO concentration (i.e., 0.02 wt%) results in a further decrease of the resistivity up to ~10^1 Ω·m. In this condition, it is important to underline that an increase of the voltage does not promote a resistivity decrease. This is the reason why 2A fibers probably represent the best compromise between the requirements of elevated conductivity and mild deposition conditions. It could be interesting to note that in our previous papers the EPD process was performed by using a GO water suspension with a concentration of 1 mg/ml (i.e., 0.1 wt%), applying an electrical field of 10 V/cm [25]. The fibers treated according to 2A process parameters were then utilized to prepare composite laminates.

Table 2. Electrical volume resistivity of the treated fibers.

Sample	Resistivity (Ω·m)
Uncoated GF	1.5×10^{14}
0A	6449 ± 241
0B	5439 ± 368
0C	2073 ± 562
1A	1154 ± 146
1B	887 ± 203
1C	222 ± 54
2A	41 ± 7
2B	51 ± 18
2C	52 ± 14

Figure 2a shows the micrographs of the neat glass fibers, while Figure 2b–j reports the micrographs of the glass fibers coated with rGO under different experimental conditions (the complete list of the process parameters is reported in Table 1). In comparison to the neat fiber (Figure 2a), GF coated by

0A, 0B, and 0C parameters (Figure 2b–d) hardly showed any physical deposition of rGO, meaning that the conditions used to create rGO coating were not satisfactory. This was further confirmed in the resistivity test of coated GFs discussed above (see Table 2). Similarly, the case of GF coated with rGO by 1A, 1B, and 1C revealed slightly more deposition, with either grey colored flakes adhered to the fiber surface and/or some wrinkle features of graphene (ubiquitous phenomenon in two-dimensional membranes) visible in Figure 2e–g. Further increasing the concentration of the GO dispersion, i.e., 2A, 2B, and 2C, resulted in increased deposition, which then showed a signficant deposition of the rGO flakes pointed out by arrows in Figure 2h–j. Even if a fine deposition of rGO was observed by these micrographs, it was not possible to determine the thickness of the deposited layer. For such reasons, cross-sectional pictures of neat GF and rGO-coated GF (under deposition condition 2A only) were attempted by SEM and reported in Figure 3.

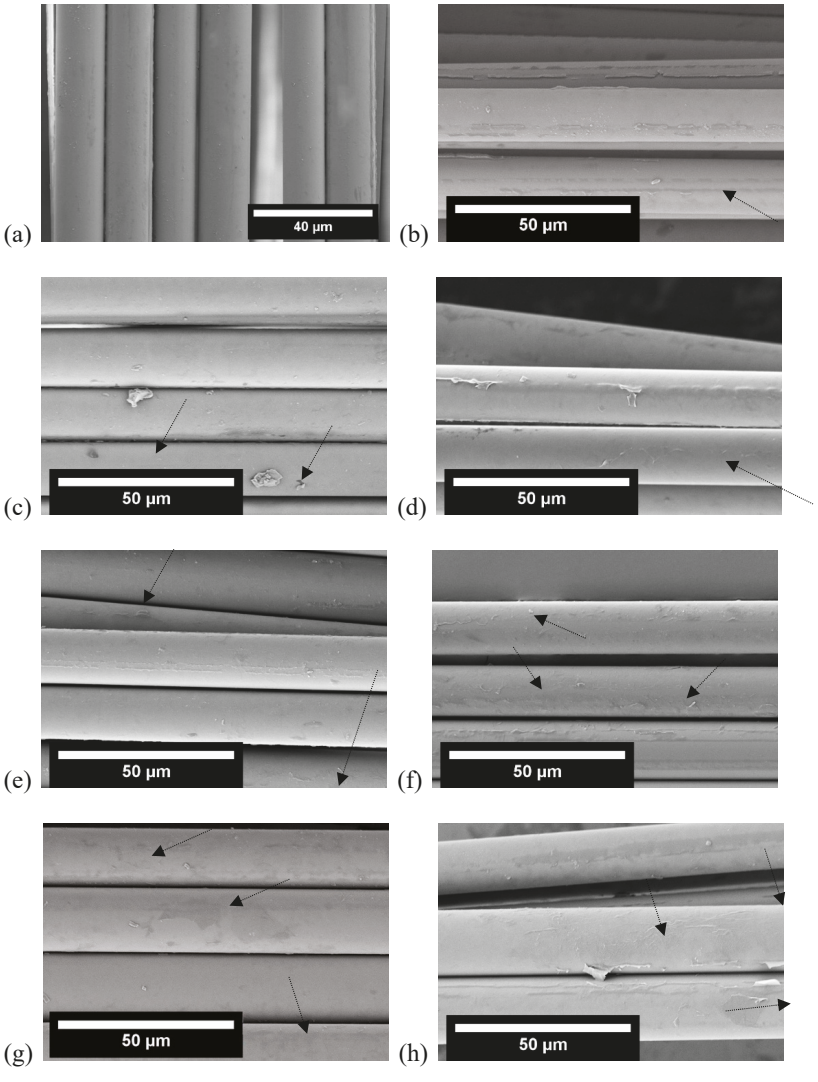

Figure 2. *Cont.*

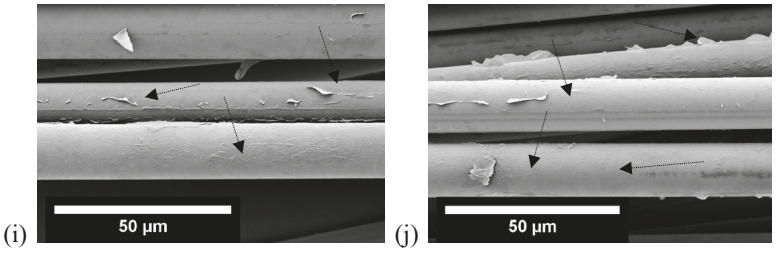

Figure 2. Scanning electron microscopy of (**a**) neat GF and GF-coated by reduced graphene oxide (rGO) under different processing conditions. (**b**) 0A, (**c**) 0B, (**d**) 0C, (**e**) 1A, (**f**) 1B, (**g**) 1C, (**h**) 2A, (**i**) 2B, (**j**) 2C.

In order to visualize the coating thickness on the GF, the neat GF and rGO-coated GF (only deposited under 2A conditions) were analyzed for their cross-section under SEM. Figure 3a,b show the neat GF under low and high magnification, and only a few particles (presumably of the sizing of GF) can be viewed. On the contrary, Figure 3c,d show the flakes of rGO on the GF, either adhered to the GF or partially hanging from the GF, which also can be seen in Figure 2h–j. These images reveal a very fine coating of rGO on the GF, deposited under 2A condition. The average thickness of the coating was measured by taking 5 measurements from one image of fiber and then taking similar measurements from other fiber images (in this case, 5 images were used in total) using ImageJ software. The average thickness of rGO coating was found to be about 45 $\pm$ 9 nm.

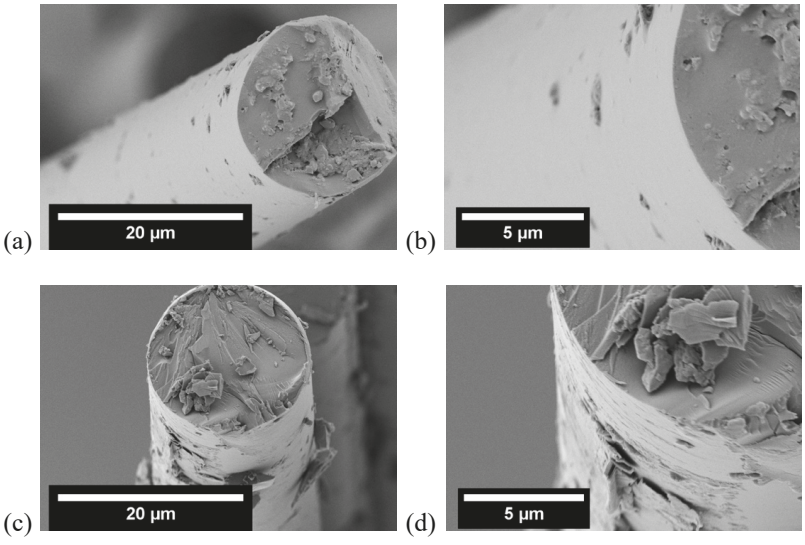

Figure 3. Scanning electron microscopy of cross-sectional view of neat GF (**a** and **b**) and GF-coated by rGO (**c** and **d**) under 2A processing condition.

3.2. Characterization of the Composites

In order to compare the properties of the produced laminates, it is important to evaluate their fiber content, density, and porosity. The fibers used to create the composite structure were weighed before composite fabrication with epoxy matrix, and the weight of composite prepared was measured after epoxy curing. The measured GF density was equal to 2.62 g/cm^3. By using the expression reported in Equation (1), an average fiber volume fraction of about 65 vol% was estimated for both EP-GF and EP-rGO-GF composites (see Table 3). Table 3 also reports the values of density and porosity of

neat epoxy, and of the prepared laminates (with either neat or rGO-coated fibers). It is interesting to note that, through a comparison between the theoretical and experimental (ρ_e) density values, EP-GF and EP-rGO-GF laminates present similar porosity values (around 4–5%, considering the associated standard deviation values).

Table 3. Density, porosity, and fiber content of the prepared composites.

Sample	Fiber Fraction (vol%)	Theoretical Density ρ_t (g/cm^3)	Experimental Density ρ_e (g/cm^3)	Void Content (vol%)
EP	-	1.1470	1.1470 ± 0.0014	-
EP-GF	65.0	2.1056	1.9960 ± 0.0068	5.20 ± 0.32
EP-rGO-GF	65.3	2.1095	2.0363 ± 0.0404	3.47 ± 1.91

The cross-sectional view obtained by using optical microscopy of the two tested composites (EP-GF and EP-rGO-GF) can be seen in Figure 4. Both specimens show a uniform distribution of the fibers within the matrix, and in the case of the EP-rGO-GF laminate, the rGO interphase cannot be distinguished because of the very low thickness of the deposited layer. These micrographs show that a good fiber–matrix interfacial adhesion can be detected in both composites, without the presence of microstructural defects. It can therefore be concluded that the samples are characterized by a similar morphology. As documented in a previous paper [45], even when observing the cross sections by SEM, it was not possible to get a reliable measure of the thickness of the rGO layer.

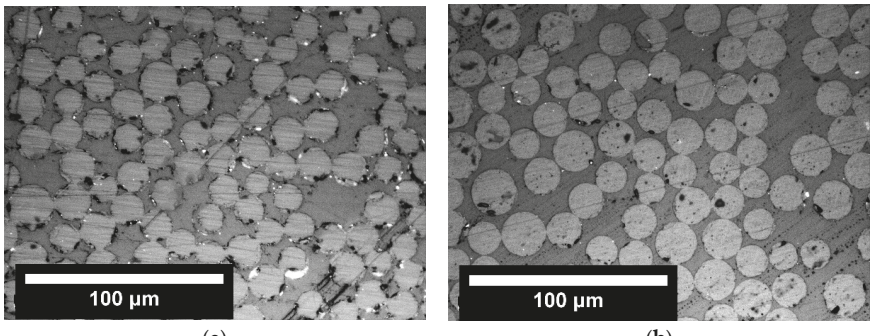

(**a**) (**b**)

Figure 4. Optical microscopy images of (**a**) EP-GF and (**b**) EP-rGO-GF composites.

Thermal stability of the composites was evaluated through thermogravimetric analysis (TGA), and the most important parameters are summarized in Table 4. It can be seen that the addition of rGO as a continuous interphase does not promote a real improvement of the thermal stability of the composites. In fact, EP-GF and EP-rGO-GF laminates present similar T_{onset}, $T_{5\%}$, and T_d values. On the other hand, it has to be considered that the mass loss in these laminates is mainly due to the degradation of the epoxy matrix, and the rGO coating around the fibers could not hinder the diffusion of the oxidation process within the samples. In other words, the initial stage of the matrix charring process is not promoted by the presence of the rGO layer around the glass reinforcement [46].

Table 4. Results of TGA analysis on neat epoxy and of the relative composites.

Parameter	EP	EP-GF	EP-rGO-GF
$T_{5\%}$	306.6	332.5	346.5
T_{onset}	335.1	347.0	332.1
T_d	346.7	375.7	367.3
r_m	7.35	77.4	81.6

$T_{5\%}$: temperature corresponding to 5% weight loss; T_{onset}: temperature corresponding to initiation of degradation; T_d: temperature corresponding to maximum mass loss rate; r_m: residual mass at 700 °C.

The thermograms of the storage modulus (E′), loss modulus (E″), and loss tangent (tanδ) are reported in Figure 5. When compared to the composite with uncoated fibers (EP-GF), EP-rGO-GF laminate presents slightly higher E′ values for $T < T_g$. From these plots, it is also interesting to notice that EP-rGO-GF sample has a lower T_g (about 20 °C of difference) with respect to the EP-GF laminate, as noticed from the peak of loss modulus and of loss tangent plots in Figure 5. This behaviour could be attributed to the fact that the presence of rGO on the surface of the fibers hinders and/or sets back the crosslinking process of the matrix during the curing process [47,48]. Moreover, it is worthwhile to note that the intensity of the loss tangent peak is higher for the EP-rGO-GF sample, thus indicating a stronger damping capability of these laminates induced by the presence of the rGO coating at the fiber/matrix interface. A detailed investigation on the interaction between the rGO layer and the glass fiber surface is reported in a recently published work [49].

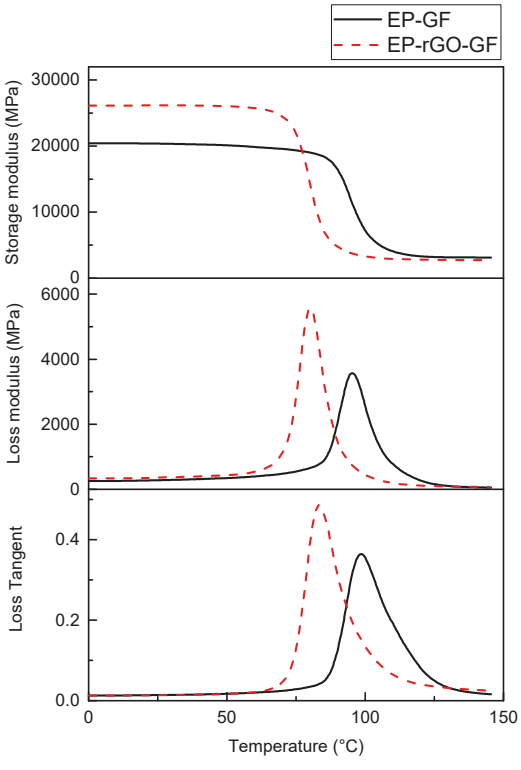

Figure 5. Storage modulus, loss modulus, and loss tangent curves from dynamic mechanical analysis (DMA) on the prepared composites.

The flexural properties of the prepared laminates under quasi-static conditions are compared in Table 5.

Table 5. Flexural properties and interlaminar shear strength (ILSS) values of the prepared composites.

Sample	Flexural Modulus (MPa)	Flexural Strength (MPa)	Flexural Strain at Break (%)	ILSS (MPa)
EP-GF	38.2 ± 0.7	687 ± 55	2.1 ± 0.2	44 ± 5
EP-rGO-GF	38.6 ± 0.8	888 ± 22	3.0 ± 0.1	57 ± 13

The elastic modulus is only slightly improved upon rGO coating of the glass fibers, while both the flexural strength and the strain at break are noticeably improved (+29 % and +43 %, respectively) compared to EP-GF laminate. This results can be explained considering that the failure mechanism of the composite laminates is strongly influenced by the fiber/matrix interfacial adhesion level. It can therefore be assumed that the presence of rGO layer at the interface could promote the stress transfer mechanism at the interface, thus promoting an increase of the failure properties of the material. In fact, a remarkable increse of the fiber/matrix adhesion has been measured in similar composites by the single fragmentation test [22]. For the same reason, it could be also hypothesized that the interlaminar shear resistance of the laminates could be improved upon rGO coating. In fact, as reported in Table 5, the ILSS value of EP-GF-rGO laminate are significantly higher than that of the EP-GF samples (+30%).

In order to evaluate the real electrical monitoring capability of the prepared laminates, electrical resisitivty measurements at three different temperatures (0 °C, 23 °C, and 50 °C) were performed by using a 2-point configuration. As shown in Figure 6, electrical volume resistivity of the EP-rGO-GF laminate is comparable to that of the rGO treated fibers (if produced according to 2A parameters shown in Table 2). This means that the presence of the matrix around the fibers does not substantially affect the conductivity behavior of the system. Considering the standard deviation values associated to these measurements, it can be concluded that the electrical resistivity of the laminates is only weakly influenced by the testing temperature with a slight decreasing trend. Therefore, the electrical behaviour of the EP-rGO-GF composite is characterized by a negative temperature coefficient (NTC) [50]. On the basis of the literature information, this behavior could be ascribed to the electron emission between the continuous interphase of rGO sheets [51–53]. It could be interesting to observe that, in the previous paper of our group [25], rGO based epoxy/glass composites characterized by a volume resistivity as low as 4.5 Ω·m were obtained by applying much harsher EPD conditions (i.e., GO concentration in water suspension of 0.1 wt%, applied electric filed of 10 V/cm).

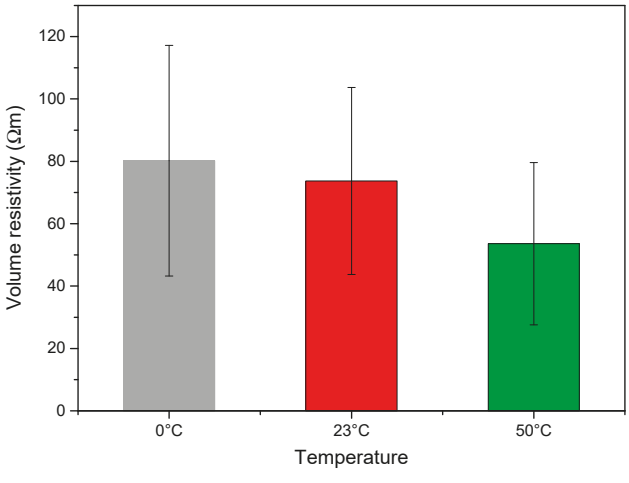

Figure 6. Electrical volume resistivity of EP-rGO-GF composite at different temperatures.

Finally, the strain/damage monitoring capabilities of EP-rGO-GF composites were tested under flexural conditions at three different temperatures. In Figure 7, the trends of the electrical resistance variation ($\Delta R/R_0$) and of the stress as a function of the applied strain are reported. It is interesting to note that as the temperature increases, the piezoresistivity of the samples is noticeably enhanced. At 0 °C and 23 °C, the resistance change is practically negligible until an applied strain of 2%. For higher strain levels, $\Delta R/R_0$ increases until the failure of the specimen occurs. At 50 °C, a more pronounced increase of $\Delta R/R_0$ with the strain can be observed, especially in the low deformation interval. These results can likely be explained by considering the NTC of EP-rGO-GF composites. In other words, a sample endowed with a higher conductivity is characterized by a better piezoresistive behaviour, and it could be thus applied for strain monitoring applications.

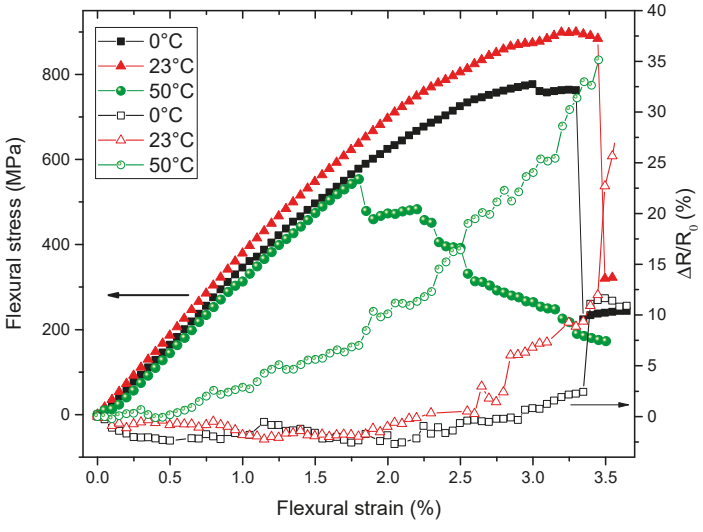

Figure 7. Piezoresistive behaviour of EP-rGO-GF composites under flexural conditions at three different temperatures (0 °C, 23 °C, and 50 °C). Full symbols: applied stress, open symbols: $\Delta R/R_0$ values.

4. Conclusions

In this work, glass fibers were treated through electrophoretic deposition by utilizing different processing parameters. The coated fibers were then subjected to chemical reduction in order to produce a conductive coating of reduced graphene oxide (rGO) on their surface. The fibers treated with the optimized parameters (i.e., by using 0.02 wt% of GO solution deposited at 0.5 V/cm) showed the highest electrical conductivity. These fibers were then utilized to prepare composite laminates through a hand lay-up technique by using an epoxy resin as matrix. The rGO deposition on the glass fibers was responsible for the slight increase of the dynamic moduli (E′, E″) of the composites, coupled with a noticeable enhancement of the flexural strength and of the delamination resistance. Furthermore, composites with rGO-coated glass fibers showed an electrical resistivity of about ~10^1 Ω·m. The EP-rGO-GF laminate was characterized by a good piezoresistive behavior under flexural conditions, and the strain monitoring sensitivity increased with the testing temperature. It was therefore demonstrated that, through a proper optimization of the EPD parameters, it is possible to produce rGO-coated glass fibers that permit the strain/damage monitoring in structural composites in a wide temperature range. Such findings could find their usefulness in applications where the temperature variation of structural composites, due to service conditions, could modify their behavior in terms of strain monitoring response.

Author Contributions: H.M., A.D., and A.P. conceived and designed the experiments; H.M. performed the experiments; H.M., A.D., and A.P. analyzed the data and wrote the paper.

Funding: This research activity has been financed by the Fondazione Cassa di Risparmio di Trento e Rovereto (CARITRO) within the project "Development of self-sensing/self-healing structural composites using graphene treated fibers" The work was also supported by the National Interuniversitary Consortium of Materials Science and Technology (INSTM).

Acknowledgments: Andrea Ruffini is gratefully acknowledged for his support to the experimental work.

Conflicts of Interest: The authors declare no conflict of interest.

References

1. Pegoretti, A.; Karger-Kocsis, J. Editorial corner—A personal view Interphase engineering in polymer composites: Challenging the devil. *Express Polym. Lett.* **2015**, *9*, 838. [CrossRef]
2. Jones, F.R. A Review of Interphase Formation and Design in Fibre-Reinforced Composites. *J. Adhes. Sci. Technol.* **2010**, *24*, 171–202. [CrossRef]
3. Karger-Kocsis, J.; Mahmood, H.; Pegoretti, A. Recent advances in fiber/matrix interphase engineering for polymer composites. *Prog. Mater. Sci.* **2015**, *73*, 1–43. [CrossRef]
4. Dorigato, A.; Brugnara, M.; Pegoretti, A. Novel polyamide 12 based nanocomposites for industrial applications. *J. Polym. Res.* **2017**, *24*, 96. [CrossRef]
5. Dorigato, A.; Pegoretti, A. Effects of carbonaceous nanofillers on the mechanical and electrical properties of crosslinked poly(cyclooctene). *Polym. Eng. Sci.* **2017**, *57*, 537–543. [CrossRef]
6. Dorigato, A.; Moretti, V.; Dul, S.; Unterberger, S.H.; Pegoretti, A. Electrically conductive nanocomposites for fused deposition modelling. *Synth. Met.* **2017**, *226*, 7–14. [CrossRef]
7. Pegoretti, A.; Dorigato, A.; Biani, A.; Slouf, M. Cyclic olefin copolymer-silica nanocomposites foams. *J. Mater. Sci.* **2016**, *51*, 3907–3916. [CrossRef]
8. Pedrazzoli, D.; Dorigato, A.; Conti, T.; Vanzetti, L.; Bersani, M.; Pegoretti, A. Liquid crystalline polymer nanocomposites reinforced with in-situ reduced graphene oxide. *Express Polym. Lett.* **2015**, *9*, 709–720. [CrossRef]
9. Dorigato, A.; Sebastiani, M.; Pegoretti, A.; Fambri, L. Effect of Silica Nanoparticles on the Mechanical Performances of Poly(Lactic Acid). *J. Polym. Environ.* **2012**, *20*, 713–725. [CrossRef]
10. Gupta, R.K.; Kennel, E.; Kim, K.-J. *Polymer Nanocomposites Handbook*; CRC Press: Boca Raton, FL, USA, 2009.
11. Hua, Y.; Li, F.; Liu, Y.; Huang, G.-W.; Xiao, H.-M.; Li, Y.-Q.; Hu, N.; Fu, S.-Y. Positive synergistic effect of graphene oxide/carbon nanotube hybrid coating on glass fiber/epoxy interfacial normal bond strength. *Compos. Sci. Technol.* **2017**, *149*, 294–304. [CrossRef]
12. Goh, G.D.; Dikshit, V.; Nagalingam, A.P.; Goh, G.L.; Agarwala, S.; Sing, S.L.; Wei, J.; Yeong, W.Y. Characterization of mechanical properties and fracture mode of additively manufactured carbon fiber and glass fiber reinforced thermoplastics. *Mater. Des.* **2018**, *137*, 79–89. [CrossRef]
13. Sun, X.; Sun, H.; Li, H.; Peng, H. Developing polymer composite materials: Carbon nanotubes or graphene? *Adv. Mater.* **2013**, *25*, 5153–5176. [CrossRef] [PubMed]
14. Chizari, K.; Arjmand, M.; Liu, Z.; Sundararaj, U.; Therriault, D. Three-dimensional printing of highly conductive polymer nanocomposites for EMI shielding applications. *Mater. Today Commun.* **2017**, *11*, 112–118. [CrossRef]
15. Cataldi, P.; Ceseracciu, L.; Marras, S.; Athanassiou, A.; Bayer, I.S. Electrical conductivity enhancement in thermoplastic polyurethane-graphene nanoplatelet composites by stretch-release cycles. *Appl. Phys. Lett.* **2017**, *110*, 121904. [CrossRef]
16. Kuilla, T.; Bhadra, S.; Yao, D.H.; Kim, N.H.; Bose, S.; Lee, J.H. Recent advances in graphene based polymer composites. *Prog. Polym. Sci.* **2010**, *35*, 1350–1375. [CrossRef]
17. Tan, L.; Wang, C.; Zeng, M.; Fu, L. Graphene: An Outstanding Multifunctional Coating for Conventional Materials. *Small* **2017**, *13*, 1603337. [CrossRef] [PubMed]
18. Cataldi, P.; Athanassiou, A.; Bayer, I. Graphene Nanoplatelets-Based Advanced Materials and Recent Progress in Sustainable Applications. *Appl. Sci.* **2018**, *8*, 1438. [CrossRef]
19. Chang, L.; Friedrich, K. Enhancement effect of nanoparticles on the sliding wear of short fiber-reinforced polymer composites: A critical discussion of wear mechanisms. *Tribol. Int.* **2010**, *43*, 2355–2364. [CrossRef]

20. Vlasveld, D.P.N.; Parlevliet, P.P.; Bersee, H.E.N.; Picken, S.J. Fibre-matrix adhesion in glass-fibre reinforced polyamide-6 silicate nanocomposites. *Compos. Part A Appl. Sci. Manuf.* **2005**, *36*, 1–11. [CrossRef]
21. Chen, J.; Zhao, D.; Jin, X.; Wang, C.C.; Wang, D.Z.; Ge, H.Y. Modifying glass fibers with graphene oxide: Towards high-performance polymer composites. *Compos. Sci. Technol.* **2014**, *97*, 41–45. [CrossRef]
22. Mahmood, H.; Tripathi, M.; Pugno, N.; Pegoretti, A. Enhancement of interfacial adhesion in glass fiber/epoxy composites by electrophoretic deposition of graphene oxide on glass fibers. *Compos. Sci. Technol.* **2016**, *126*, 149–157. [CrossRef]
23. Ali, M.A.; Umer, R.; Khan, K.A.; Samad, Y.A.; Liao, K.; Cantwell, W. Graphene coated piezo-resistive fabrics for liquid composite molding process monitoring. *Compos. Sci. Technol.* **2017**, *148*, 106–114. [CrossRef]
24. Moriche, R.; Sánchez, M.; Jiménez-Suárez, A.; Prolongo, S.G.; Ureña, A. Strain monitoring mechanisms of sensors based on the addition of graphene nanoplatelets into an epoxy matrix. *Compos. Sci. Technol.* **2016**, *123*, 65–70. [CrossRef]
25. Mahmood, H.; Vanzetti, L.; Bersani, M.; Pegoretti, A. Mechanical properties and strain monitoring of glass-epoxy composites with graphene-coated fibers. *Compos. Part A Appl. Sci. Manuf.* **2018**, *107*, 112–123. [CrossRef]
26. Pedrazzoli, D.; Dorigato, A.; Pegoretti, A. Monitoring the mechanical behaviour of electrically conductive polymer nanocomposites under ramp and creep conditions. *J. Nanosci. Nanotechnol.* **2012**, *12*, 4093–4102. [CrossRef] [PubMed]
27. Moriche, R.; Jiménez-Suárez, A.; Sánchez, M.; Prolongo, S.G.; Ureña, A. Graphene nanoplatelets coated glass fibre fabrics as strain sensors. *Compos. Sci. Technol.* **2017**, *146*, 59–64. [CrossRef]
28. Eswaraiah, V.; Balasubramaniam, K.; Ramaprabhu, S. Functionalized graphene reinforced thermoplastic nanocomposites as strain sensors in structural health monitoring. *J. Mater. Chem.* **2011**, *21*, 12626–12628. [CrossRef]
29. Pedrazzoli, D.; Dorigato, A.; Pegoretti, A. Monitoring the mechanical behavior under ramp and creep conditions of electrically conductive polymer composites. *Compos. Part A Appl. Sci. Manuf.* **2012**, *43*, 1285–1292. [CrossRef]
30. Wang, X.; Liu, H.; Fang, P.; Liao, L.; Pan, C.; Liew, K.M. Interface enhancement of glass fiber/vinyl ester composites with carbon nanotubes synthesized from ethanol flames. *J. Nanosci. Nanotechnol.* **2010**, *10*, 948–955. [CrossRef]
31. Zhang, J.E.; Zhuang, R.C.; Liu, J.W.; Mader, E.; Heinrich, G.; Gao, S.L. Functional interphases with multi-walled carbon nanotubes in glass fibre/epoxy composites. *Carbon* **2010**, *48*, 2273–2281. [CrossRef]
32. Lv, P.; Feng, Y.Y.; Zhang, P.; Chen, H.M.; Zhao, N.Q.; Feng, W. Increasing the interfacial strength in carbon fiber/epoxy composites by controlling the orientation and length of carbon nanotubes grown on the fibers. *Carbon* **2011**, *49*, 4665–4673. [CrossRef]
33. Tzounis, L.; Kirsten, M.; Simon, F.; Mader, E.; Stamm, M. The interphase microstructure and electrical properties of glass fibers covalently and non-covalently bonded with multiwall carbon nanotubes. *Carbon* **2014**, *73*, 310–324. [CrossRef]
34. Böger, L.; Wichmann, M.H.G.; Meyer, L.O.; Schulte, K. Load and health monitoring in glass fibre reinforced composites with an electrically conductive nanocomposite epoxy matrix. *Compos. Sci. Technol.* **2008**, *68*, 1886–1894. [CrossRef]
35. Gao, L.; Thostenson, E.T.; Zhang, Z.; Chou, T.W. Sensing of damage mechanisms in fiber-reinforced composites under cyclic loading using carbon nanotubes. *Adv. Funct. Mater.* **2009**, *19*, 123–130. [CrossRef]
36. Dorigato, A.; Pegoretti, A.; Bondioli, F.; Messori, M. Improving Epoxy Adhesives with Zirconia Nanoparticles. *Compos. Interface* **2010**, *17*, 873–892. [CrossRef]
37. Dorigato, A.; Pegoretti, A. The role of alumina nanoparticles in epoxy adhesives. *J. Nanopart. Res.* **2011**, *13*, 2429–2441. [CrossRef]
38. Shen, J.F.; Huang, W.S.; Wu, L.P.; Hu, Y.Z.; Ye, M.X. The reinforcement role of different amino-functionalized multi-walled carbon nanotubes in epoxy nanocomposites. *Compos. Sci. Technol.* **2007**, *67*, 3041–3050. [CrossRef]
39. Thostenson, E.T.; Li, W.Z.; Wang, D.Z.; Ren, Z.F.; Chou, T.W. Carbon nanotube/carbon fiber hybrid multiscale composites. *J. Appl. Phys.* **2002**, *91*, 6034–6037. [CrossRef]
40. Mei, L.; He, X.D.; Li, Y.B.; Wang, R.G.; Wang, C.; Peng, Q.Y. Grafting carbon nanotubes onto carbon fiber by use of dendrimers. *Mater. Lett.* **2010**, *64*, 2505–2508. [CrossRef]

41. Bekyarova, E.; Thostenson, E.T.; Yu, A.; Kim, H.; Gao, J.; Tang, J.; Hahn, H.T.; Chou, T.W.; Itkis, M.E.; Haddon, R.C. Multiscale carbon nanotube-carbon fiber reinforcement for advanced epoxy composites. *Langmuir* **2007**, *23*, 3970–3974. [CrossRef]
42. Besra, L.; Liu, M. A review on fundamentals and applications of electrophoretic deposition (EPD). *Prog. Mater. Sci.* **2007**, *52*, 1–61. [CrossRef]
43. Thomas, B.; Boccaccini, A.; Shaffer, M. Multi-Walled Carbon Nanotube Coatings Using Electrophoretic Deposition (EPD). *J. Am. Ceram. Soc.* **2005**, *88*, 980–982. [CrossRef]
44. Cho, J.; Konopka, K.; Rozniatowski, K.; Garcia-Lecina, E.; Shaffer, M.S.P.; Boccaccini, A.R. Characterisation of carbon nanotube films deposited by electrophoretic deposition. *Carbon* **2009**, *47*, 58–67. [CrossRef]
45. Mahmood, H.; Unterberger, S.; Pegoretti, A. Tuning electrical and thermal properties in epoxy/ glass composites by graphene-based interphase. *J. Compos. Sci.* **2017**, *1*, 12. [CrossRef]
46. Wang, X.; Yang, H.Y.; Song, L.; Hu, Y.; Xing, W.Y.; Lu, H.D. Morphology, mechanical and thermal properties of graphene-reinforced poly(butylene succinate) nanocomposites. *Compos. Sci. Technol.* **2011**, *72*, 1–6. [CrossRef]
47. Pissis, P. *Thermoset Nanocomposites for Engineering Applications*; iSmithers Rapra Publishing: Shawbury, UK, 2007.
48. Wei, J.; Vo, T.; Inam, F. Epoxy/graphene nanocomposites—Processing and properties: A review. *RSC Adv.* **2015**, *5*, 73510–73524. [CrossRef]
49. Tripathi, M.; Mahmood, H.; Novel, D.; Iacob, E.; Vanzetti, L.; Bartali, R.; Speranza, G.; Pegoretti, A.; Pugno, N. Nanoscale friction of graphene oxide over glass-fibre and polystyrene. *Compos. Part B* **2018**, *148*, 272–280. [CrossRef]
50. Traina, M.; Pegoretti, A.; Penati, A. Time-temperature dependence of the electrical resistivity of high density polyethylene—Carbon black composites. *J. Appl. Polym. Sci.* **2007**, *106*, 2065–2074. [CrossRef]
51. Shao, Q.; Liu, G.; Teweldebrhan, D.; Balandin, A.A. High-temperature quenching of electrical resistance in graphene interconnects. *Appl. Phys. Lett.* **2008**, *92*, 202108. [CrossRef]
52. Das, N.C.; Chaki, T.K.; Khastgir, D. Effect of processing parameters, applied pressure and temperature on the electrical resistivity of rubber-based conductive composites. *Carbon* **2002**, *40*, 807–816. [CrossRef]
53. Hao, B.; Ma, Q.; Yang, S.D.; Mader, E.; Ma, P.C. Comparative study on monitoring structural damage in fiber-reinforced polymers using glass fibers with carbon nanotubes and graphene coating. *Compos. Sci. Technol.* **2016**, *129*, 38–45. [CrossRef]

fibers

MDPI

Article

Investigation of Chemical and Physical Surface Changes of Thermally Conditioned Glass Fibres

Peter G. Jenkins [1,*], Liu Yang [1], James L. Thomason [1], Xinyong Chen [2], John F. Watts [3] and Steven J. Hinder [3]

[1] Department of Mechanical & Aerospace Engineering, University of Strathclyde, 75 Montrose Street, Glasgow G1 1XJ, UK; l.yang@strath.ac.uk (L.Y.); james.thomason@strath.ac.uk (J.L.T.)
[2] School of Pharmacy, University of Nottingham, University Park, Nottingham NG7 2RD, UK; x.chen@nottingham.ac.uk (X.C.)
[3] The Surface Analysis Laboratory, Department of Mechanical Engineering Sciences, Mail Stop A1, University of Surrey, Guildford, Surrey GU2 7XH, UK; j.watts@surrey.ac.uk (J.F.W.); s.hinder@surrey.ac.uk (S.J.H.)
* Correspondence: peter.jenkins@strath.ac.uk; Tel.: +44-141-574-5088

Received: 27 November 2018; Accepted: 8 January 2019; Published: 15 January 2019

Abstract: A number of analytical techniques were applied to investigate changes to the surface of unsized boron-free E-glass fibres after thermal conditioning at temperatures up to 700 °C. Novel systematic studies were carried out to investigate the fundamental strength loss from thermal conditioning. Surface chemical changes studied using X-ray photoelectron spectroscopy (XPS) showed a consistent increase in the surface concentration of calcium with increasing conditioning temperature, although this did not correlate well with a loss of fibre strength. Scanning electron microscopy fractography confirmed the difficulty of analysing failure-inducing flaws on individual fibre fracture surfaces. Analysis by atomic force microscopy (AFM) did not reveal any likely surface cracks or flaws of significant dimensions to cause failure: the observation of cracks before fibre fracture may not be possible when using this technique. Fibre surface roughness increased over the whole range of the conditioning temperatures investigated. Although surface roughness did not correlate precisely with fibre strength, there was a clear inverse relationship at temperatures exceeding 400 °C. The interpretation of the surface topography that formed between 400–700 °C produced evidence that the initial stage of phase separation by spinodal decomposition may have occurred at the fibre surface.

Keywords: glass fibre; heat treatment; strength loss; X-ray photoelectron spectroscopy (XPS); atomic force microscopy (AFM)

1. Introduction

Glass fibre is the predominate reinforcement material that is used in polymer composites, due its relatively high specific properties, low cost and a versatility, due to the ability for the surface to be chemically tailored for different polymer matrices; the annual consumption of E-glass fibres is in excess of 7 million tons [1]. Global glass fibre usage has continued to increase over the last few years, driven by a greater use of composites in established sectors as well as adoption in new markets [2]. However, a significant challenge facing the glass fibre and composites industries is the relative difficulty associated with the cost-effective recycling of glass fibre-reinforced polymer (GFRP) materials at the end of life. The issue is particularly acute with GFRP utilising thermosetting polymers, as opposed to thermoplastics, which retain an inherent recyclability, even when they are used to produce composites. Although some routes exist, such as mechanical grinding for use as a filler or incorporation in cement production [3,4], limitations to these processes mean that neither are likely to be able to accommodate the increasing volumes of end-of-life materials.

Alternative approaches to GFRP recycling are predicated on the benefits of separating the matrix, and any fillers, from the fibrous reinforcement. The glass fibres may be considered as the most valuable fraction [3] and its possible recovery and reuse in second-generation composites would produce major technological, economic and environmental impacts. The separation of fibres and matrix in GFRP requires the application of aggressive processes such as pyrolysis, solvolysis or thermal recycling in the presence of oxygen, for example by fluidised bed combustion (FBC) [5]. Of the existing technologies, there is a substantial body of research on the effect of thermal recycling on the properties of the recovered fibres [5–9]. A universal finding of this research is the large decrease in fibre tensile strength following thermal treatments or recycling, as summarised most comprehensively in [10].

Despite this phenomenon first being reported 60 years ago [11], a full and clear understanding of all the mechanisms that contribute to thermally-induced strength loss has yet to be presented in the literature. It is generally agreed that the failure of brittle materials such as glass fibres is controlled by the presence of flaws [12]: during a tensile test, for example, failure will occur at the most critical surface flaw when a corresponding critical stress is applied. This remains the case when fibres have been heat-treated or thermally recycled, as their brittle nature is preserved. Mechanically inflicted surface damage, creating larger critical flaws or enhancing those pre-existing flaws, can be invoked to explain the strength loss in cases such as the thermal treatment of sized fibres [9] or more aggressive processes like FBC recycling [5], in which some of the lowest reported normalised strength retention values (of the order of 5–10%) have been reported.

It is the case, however, that a significant decrease in glass fibre strength occurs due to exposure to elevated temperature, even in the absence of mechanical sources of surface damage [7,13,14]. This strength loss cannot be attributed to the degradation of surface sizing, as it was measured by using fibres intentionally produced without any surface sizing, referred to as bare- or water-sized. In these experiments, fibres were thermally conditioned individually, rather than in typical fibre bundles. The authors showed in previous work [7] that very careful handling throughout the thermal conditioning process produces higher retained fibre strengths when compared to the typically used method of removing single fibre test specimens from previously conditioned fibre bundles. Fibre handling damage, which occurs during fibre specimen extraction, was suggested as the source of additional mechanical handling damage. Significantly, this study also revealed that a fundamental thermal strength loss occurs that is not related to either the degradation of the fibre surface coating, or to mechanical damage. It is this fundamental thermal-based strength loss that is yet to be fully explained.

In the work presented here, this mechanism of strength loss was further explored by using water-sized E-glass fibres whose fundamental thermal strength loss has already been described in [7]. The investigation characterised the chemical and physical changes of thermally conditioned fibres, using X-ray photoelectron spectroscopy (XPS), atomic force microscopy (AFM) and scanning electron microscopy (SEM). To our knowledge, this is the first such systematic study of this type to be reported. The work is an important step in the development of a better understanding of the strength loss of heat-treated and recycled glass fibres.

2. Materials and Methods

Boron-free E-glass (Advantex) fibres manufactured by Owens Corning Vetrotex were investigated in this study. These fibre rovings were produced on a pilot scale bushing as 20 kg continuous single-end square edge packages. The nominal tex of the rovings was 1200 g/km, and the nominal single-fibre diameter was 17.4 ± 1.3 μm. The fibres used in the study had no sizing applied during the initial manufacturing, and instead, had only been water-sprayed, using the normal cooling sprays under the bushing. Fibre rovings were subsequently dried at 105 °C for 24 hr. These samples are referred to as bare- or water-sized, as it can be assumed that most of the water is removed during the subsequent drying step. Glassbond Saureisen Electrotemp Cement No. 8 was used to restrain fibres during high-temperature treatments where glue or epoxy-based adhesives were no longer sufficient.

During the course of the investigation, the various analyses that were performed required the heat treatment of samples to be carried out in different manners. Considerations such as the length and number of fibres needed, or furnace atmosphere were assessed, and an appropriate choice was made in each case. All heat treatments were performed under air; however, the moisture content within the treatment atmosphere varied slightly. A normal atmospheric relative humidity of 35–45% was measured; compressed air that was supplied to the thermo-gravimetric analyser (TGA) and thermo-mechanical analyser (TMA) had a relative humidity of no more than 5%.

The heat treatment of glass fibres for tensile testing was carried out by using a Carbolite CWF 12/13 furnace, preheated to between 200–700 °C. Fibres were heat-treated for 25 min (of which approximately the first 10 min was required for the furnace to equilibrate to its set temperature), then removed immediately to cool in room temperature air. All treatments were carried out by using fibres taken from a single bundle from the roving. Individual fibres were extracted from the bundle prior to any heating, and mounted onto wire frames using cement. Rather than being held tightly between the two fixing points, the fibres were mounted with some slack along the length. Any thermal expansion of the frames would not, therefore, induce the longitudinal tensile stress. Secondly, it was possible for fibres to flex when exposed to convective air currents; bending stresses caused by this would be concentrated mainly at the fibre ends, which did not form part of the tested gauge length.

Heat treatment of glass fibres to be analysed by XPS was carried out in a TA Instruments Q50 TGA. A short length of fibre bundle was placed in the centre of a platinum pan. A ramp rate of 10 °C/min was applied from room temperature to the target temperature; once this was reached, the program ended and the sample was allowed to cool naturally back to room temperature. The purge gas used was air at a flow rate of 50 mL/min.

Heat treatment of glass fibres to be analysed by Atomic Force Microscopy (AFM) or Scanning Electron Microscopy (SEM) was carried out in a TA Instruments Q400 TMA. A number of parallel fibres were affixed at one end only, in Glassbond cement. Once dry, the assembly was hung in the TMA furnace by using the slot in a film/fibre stage, with the fibres pointing downwards. Heat treatment of fibres was performed using a temperature range of 200–700 °C. The furnace was equilibrated to within 10% of the treatment temperature within the first minute, and to the precise temperature within approximately 5 min. A 15 min isothermal was then applied, after which the furnace was cooled to room temperature within no more than 10 min. The furnace was purged using air at a flow rate of 50 mL/min.

Single-fibre tensile properties were obtained according to the method described in ASTM C1557-03. The details of the procedure utilised are described comprehensively by Yang and Thomason [15]. All fibres were mounted at a gauge length of 20 mm. After each individual fibre diameter was measured by optical microscopy, the samples were tested using an Instron 3342 universal testing machine equipped with a 10 N load cell. An extension rate of 0.3 mm/min was used in all cases. The average strength values at each condition were based on at least 20 tensile tests. All tests were carried out at room temperature and at approximately 50% relative humidity.

Elemental surface compositions (of the outermost 6 nm approximately) were determined using a Thermo Scientific^{TM} (East Grinstead, UK) Theta Probe spectrometer. A monochromated Al Kα X-ray source (1486.6 eV) was employed for all spectra acquisitions. Survey spectra were acquired using a pass energy of 300 eV while high-resolution, core-level spectra were acquired using a Pass Energy of 50 eV. All spectra were acquired using an X-ray spot size of ~400 μm radius. Bundles of glass fibres were placed parallel to one another on the sample holder: the longitudinal axes of the fibre were aligned with the X-ray spots major axis. The insulating nature of the glass fibre samples required the utilisation of charge compensation using a low energy, electron flood gun. The charge compensation conditions were optimised for each sample individually. All spectra were charge-referenced against the C1s peak at 285 eV to correct for charging effects during acquisition. Quantitative surface chemical analyses were calculated from the high-resolution, core-level spectra following the removal of a non-linear

(Shirley) background. The manufacturer's Avantage software was employed, which incorporates the appropriate sensitivity factors and corrects for the electron energy analyser transmission function.

Glass fibre surfaces were imaged by using AFM and SEM. AFM topography images were obtained using a D3000 AFM (Bruker Nano GmbH, Karlsruhe, Germany). Height and phase data were collected in Tapping Mode® using a RTESPA-150 type tip with a cantilever spring constant of 5 N/m and a resonant frequency of approximately 300 kHz. At least two fibres were imaged for each condition and two images of approximately 3 μm × 3 μm were captured for each of these fibres. Images were obtained at a rate of 1.5 Hz with the fast scan direction being perpendicular to the longitudinal fibre axis. The roughness of each fibre surface image was quantified using root mean square (RMS) roughness, defined as the square root of mean square of the height deviation from the mean elevation plane, after removing the background curvature by polynomial fitting. All statistics generated from raw AFM data were produced using NanoScope Analysis software.

Fibres imaged by SEM were first sputter-coated with gold. Images were obtained by using a Hitachi SU6600 Field Emission SEM (FE-SEM), operated at an accelerating voltage of 15 kV and an extraction voltage of 1.8 kV. The fibre fracture surfaces were imaged perpendicular to the fracture face, but they were sputter-coated with it parallel to the target, in order to minimise the thickness of the coating deposited, and thus to reduce potential obscuring of surface features.

3. Results

3.1. Tensile Strength of Heat-Treated Fibres

Bare fibres were heat-treated in a furnace, using the method described, at temperatures between 200–700 °C. The average single-fibre tensile strengths (error bars show 95% confidence limits) measured at room temperature following heat treatment are presented in Figure 1.

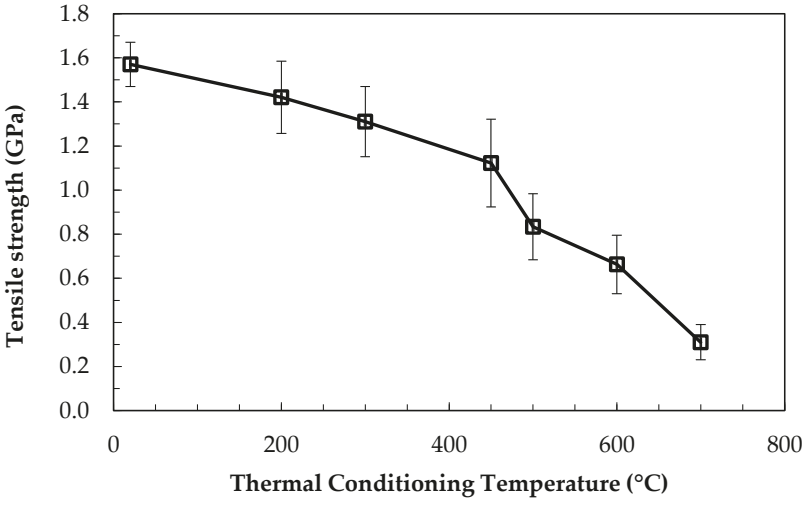

Figure 1. Tensile strengths of bare fibres after thermal conditioning at 200–700 °C for 25 min.

A trend of strength loss with increasing thermal conditioning temperature was found. A temperature of 300 °C was required for a significant decrease with respect to the initial strength of the fibres to occur, as measured by 95% confidence limits. The most significant strength loss occurred when the conditioning temperature exceeded 450 °C: after treatment at 500, 600, and 700 °C approximately 50, 40, and 20%, respectively, of the initial strength remained.

The strength values in Figure 1 represent the average of at least 20 individual tensile tests, with the exception of the data point at 700 °C. The retained strength of these heat treated fibres was very low, and it approaches the lower limit that was possible to measure when using the standard method. Many fibres break before testing at the points at which they are glued to tensile card templates; they are unable to withstand the minimal bending and twisting stresses related to the cutting of the card template that allows the fibre to bear load during testing. Additionally, some fibres failed at the edge of the gauge length, rather than in the middle portion. This is also likely to be attributable to slight bending at the beginning of the test as tension is first applied to the fibre. The standard practice is to discount such tests from the final analysis, as it is presumed that their inclusion causes an under-estimation of the average fibre strength.

3.2. X-Ray Photoelectron Spectroscopy

XPS spectra were collected for untreated bare glass fibres, and for those heat-treated at the temperatures of most interest with respect to fundamental strength loss: a range of 450–600 °C was selected. Two individual series of data (ser1, ser2) were obtained using new samples each time, with approximately one month between the collections of the series. The major elemental components identified, in addition to carbon from contamination, were oxygen, silicon, calcium, aluminium, magnesium and sodium. All results, given as elemental atomic percentages (at. %), have been corrected against the carbon content of the individual samples: carbon exists only as a contaminant, and it should not be present in bare glass samples either at the surface or in the bulk. The two series of data were averaged and the results are shown in Table 1. The degree of repeatability between the two series of measurements was generally high: for major glass constituents, the individual values deviated by only a few percent from the average. The results for minor constituents such as Na or Mg were, at times, much less repeatable, and at some treatment temperatures, they deviated from the average by 25–50%. This may have been caused by the difficulty in accurately quantifying them from the XPS scan data.

Table 1. Atomic percentages of constituent elements at the surface of boron-free E-glass from X-ray photoelectron spectroscopy (XPS).

Treatment temperature (°C)	Element Atomic %					
	Si	**O**	**Ca**	**Al**	**Mg**	**Na**
20	18.97	70.27	5.36	3.94	1.13	0.31
450	18.94	67.55	5.60	3.62	2.66	1.27
500	19.72	67.7	5.56	4.56	1.34	1.12
600	19.26	67.84	6.14	4.42	1.66	0.67

It was found that the variability in Si and O, the two constituents with the highest at. %, were inter-related. The data in Figure 2 show that when the at. % of oxygen increased, for example, from 450 to 500 °C, there was a corresponding decrease in the at. % of Si. It is probable that changes in oxygen content, due to differing surface contamination levels between samples, exert an influence over other constituent elements, which all have significantly lower at. %

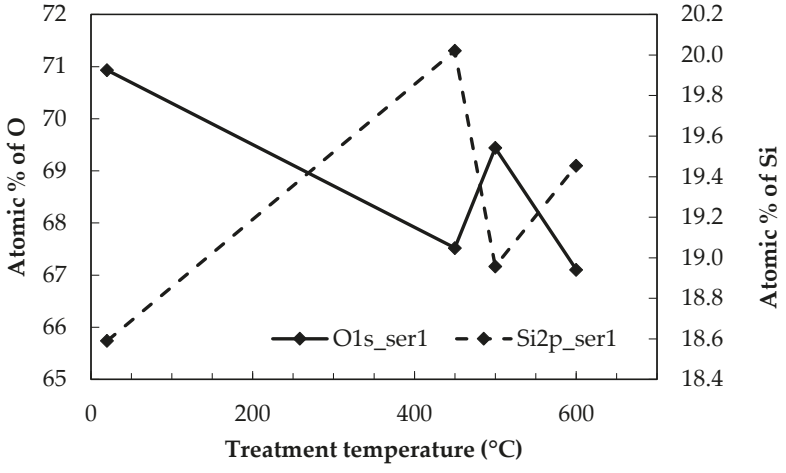

Figure 2. Atomic percentages of Si and O at the E-glass surface with respect to the thermal conditioning temperature.

In contrast to the other elements measured in the analysis, Ca demonstrated a relatively consistent trend with the conditioning temperature, as shown in Figure 3. In each of the series of measurements carried out, an increase in Ca at the fibre surface was observed after conditioning at 600 °C, while its at. % was largely stable throughout the rest of the temperature range investigated. The increase was more pronounced in the first series than the second.

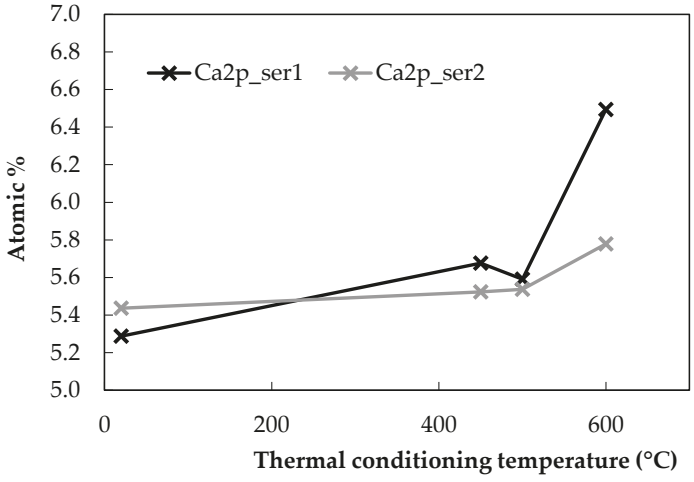

Figure 3. Atomic percentages of Ca at the E-glass surface with respect to the thermal conditioning temperature.

3.3. Atomic Force Microscopy

The average RMS roughness of bare E-glass fibres is presented in Figure 4, alongside the strength-loss behaviour of the fibres from Figure 1.

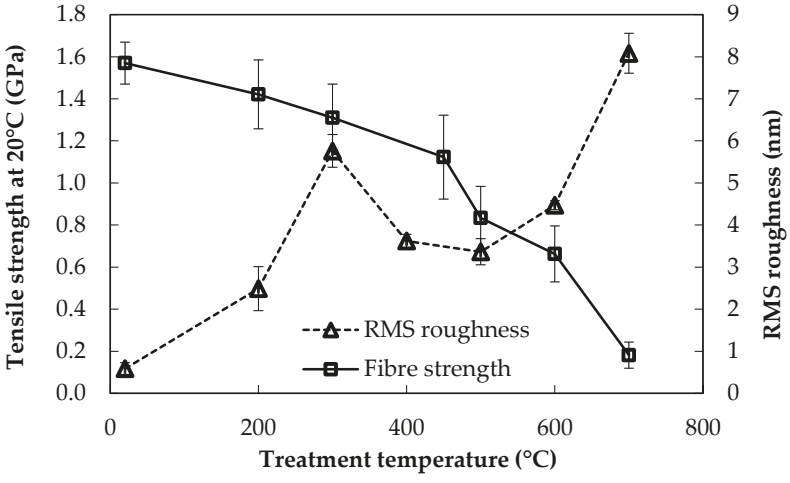

Figure 4. Average fibre tensile strength at room temperature, and fibre surface RMS roughness after thermal conditioning.

It was observed that fibre surface roughness increased with increasing conditioning temperature, while fibre strength decreased. Aside from this general trend, the correlation between these data was not close. For example, surface roughness increased significantly following treatment to only 200 °C, whereas fibre strength was not significantly different from the baseline value at these low treatment temperatures. The region of most significant strength loss occurred for conditioning temperatures in excess of 450 °C: of the total strength loss between room temperature and 600 °C, around 50% of the loss occurred between 450–600 °C. Over a similar range of thermal conditioning temperature from 400–600 °C, there was only a relatively small increase, however, in RMS roughness. A close inverse correlation between the retained tensile strength and the surface roughness was observed at the higher end of the conditioning temperatures investigated between 500–700 °C. Fibre strengths decreased precipitously, while the fibre surface roughness increased very rapidly, more than doubling from 500 to 700 °C.

If, instead of RMS roughness, the maximum depth below the z = 0 plane (labelled z-min) was plotted against the heat treatment temperature, the graph obtained was approximately the inverse. It should be noted that the values of z_{min} were obtained directly from the raw topographical data. The z = 0 plane is established automatically by the Nanoscope software after polynomial fitting, and it lies at the mean of all of the height data points. The values of z_{min} represent the deepest flaws, pits or slots at the fibre surface that could be detected. These data are plotted with the retained fibre tensile strength in Figure 5.

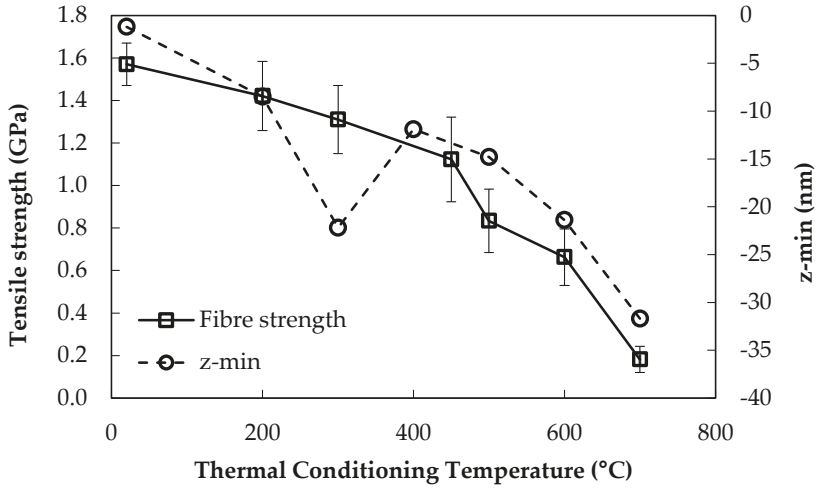

Figure 5. Average fibre tensile strength at room temperature, and average minimum topographical feature in the z-direction after thermal conditioning.

The data in Figure 5 show that the trend for the average z_{min} of topography at each treatment temperature correlated relatively well at higher treatment temperatures with fibre strength loss, but there was an obvious disparity at 300 °C. The decrease in z_{min} between 400–500 °C was only relatively small in comparison, with a significant decrease in fibre strength over the same temperature range.

The changes in surface topography observed using AFM were relatively consistent at each conditioning temperature. Examples of some typical topography plots are given in Figure 6.

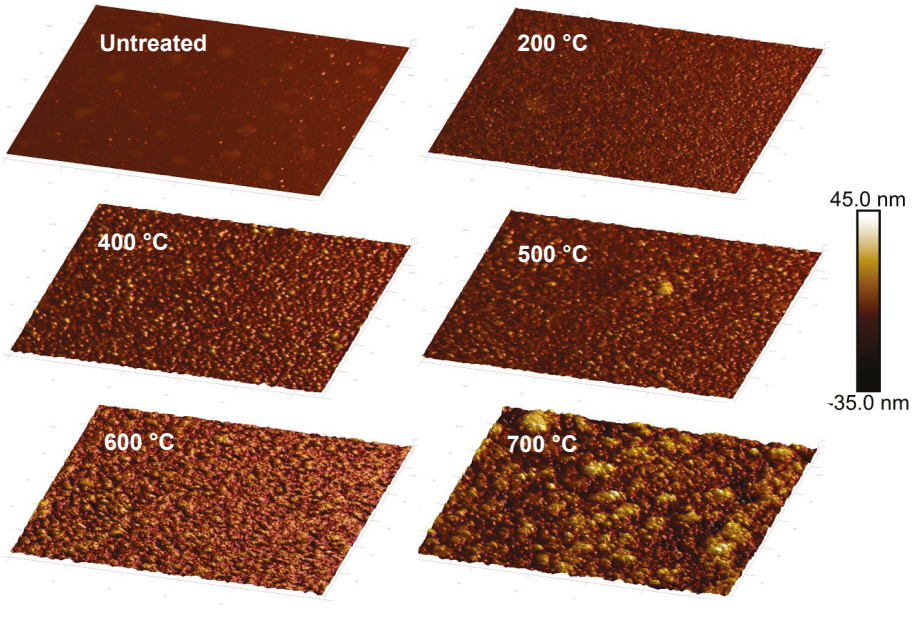

Figure 6. Three-dimensional topography plots of bare E-glass fibre: untreated and thermally conditioned at 200–700 °C.

The surface of untreated fibres was mostly flat, but two types of surface features were observed. Raised circular or ovoid areas of between 100–200 nm in diameter were found; phase plots indicated that these were part of the glass and not a contaminant on the surface. Very small contaminant particles of no more than a few tens of nm in size, identified by a clear phase contrast with the glass, covered the surfaces of all samples. The heat treatment process appeared to remove these contaminant particles. Changes to the surface topography as the roughness increased were generally homogenous across the surface of fibres: Figure 6 shows the typical topographic plots of fibres thermally conditioned between 200 to 700 °C. The additional images obtained at each conditioning temperature were similar to those presented; this was reflected in the size of the error bars in Figure 4, as the average roughness was calculated using all of the available topography data.

After thermal conditioning at only 200 °C, the fibre surface changed completely in comparison to the untreated fibre. A uniform textured appearance was observed, and the maximum height in the z-direction almost doubled in comparison to the untreated fibres. It is possible that this new rougher surface structure obscured the circular mounds that were previously found, but this was not tested. Alternatively, these features could also be a product of some surface contamination that was removed when the fibres were thermally conditioned. This explanation, however, seems less likely, as the mounds were not discernible in the AFM phase data, suggesting that they have similar mechanical properties to the glass surface.

As all of the topography plots in Figure 6 are presented using the same z-scale, the progressive increase in z-range that corresponds with increasing roughness through the range of conditioning temperatures can be clearly observed. Approaching the critical temperature range for strength loss at 400 and 500 °C, the fibre topography was mostly unchanged, reflecting the constant roughness. The surface of the fibres, particularly those conditioned at 400 °C, showed the development of numerous small but well-defined peaks measuring approximately 50–70 nm in the x–y plane. At the highest conditioning temperatures of 600–700 °C, individual peaks were no longer visible, and the entire fibre surface instead appeared to be mottled. The average z-range of the analysed areas increased by almost an order of magnitude from the initially untreated fibres to those conditioned at 700 °C.

Extracted from typical topography plots, 2D line sections from fibres heat-treated at 400, 500, 600 and 700 °C are presented in Figures 7 and 8.

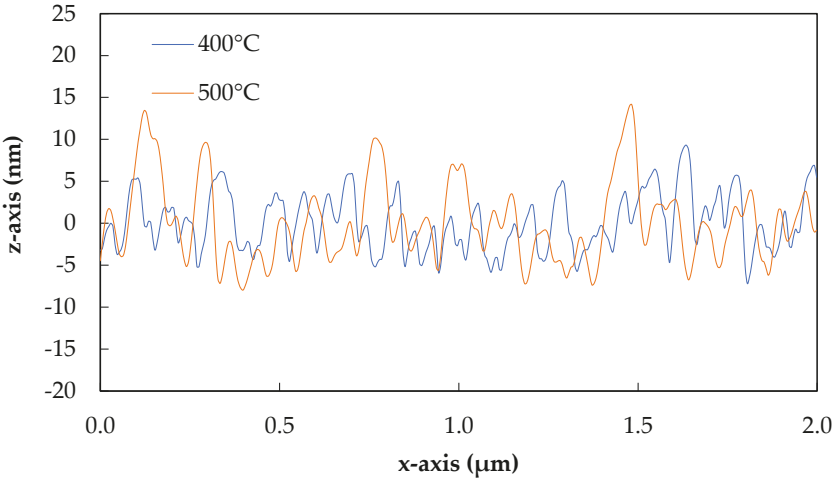

Figure 7. Typical 2D sections of the surface topography after heat treatment at 400 and 500 °C.

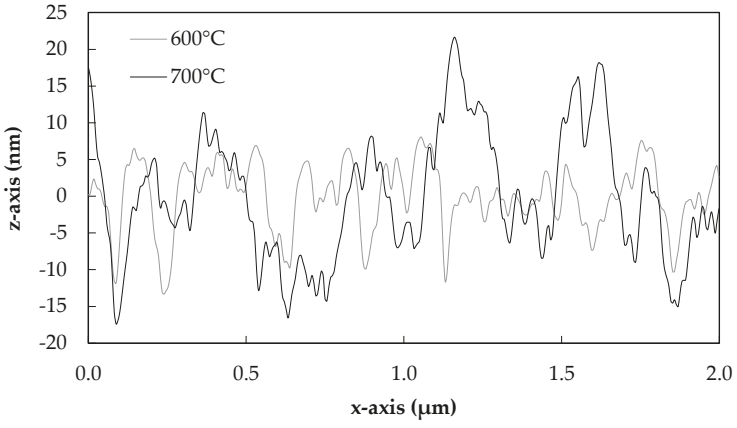

Figure 8. Typical 2D sections of the surface topography after heat treatment at 600 and 700 °C.

The slight differences in the surface morphologies of fibres treated at 400 and 500 °C can be more clearly observed in Figure 7. A greater number of smaller peaks were observed for 400 °C treated fibres than 500 °C, although the heights of these were approximately the same overall. Fibres treated at 600 °C began to lose smaller well-defined peaks, as can be seen in Figure 8, and this process was clearer yet for fibres treated at 700 °C. In this latter case, the peaks appeared to further coalesce together in groups, and the heights of the features again increased significantly.

An estimate of the total surface area covered by the developing surface topography was obtained by using the built-in capabilities of NanoScope Analysis. The half-height of each topographical image was calculated by using the raw data, after the exclusion of features due to surface contamination, using the simple equation $\frac{1}{2}(z_{max} - z_{min})$. A mask was placed at this height, and the surface coverage of the features lying above the mask was measured. A selection of heat-treated fibres with these features identified by the software is shown in Figure 9.

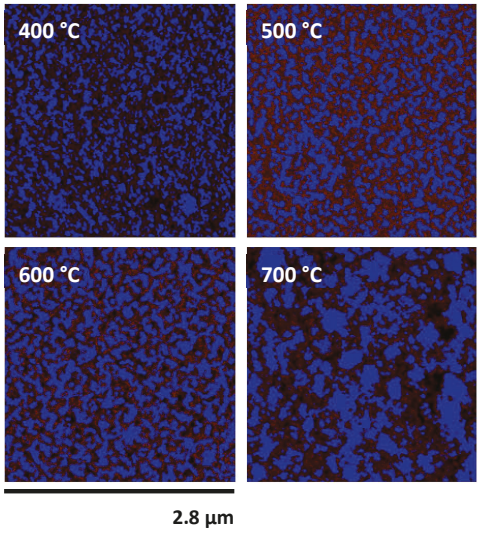

Figure 9. Fibre topography of heat-treated fibres masked to identify the coverage of the structure (sample areas approx. 2.8 × 2.8 µm).

This procedure was carried out on all fibre surface areas for which topographical data were obtained; the results were averaged and are presented in Figure 10. Error bars indicate the sample standard deviations.

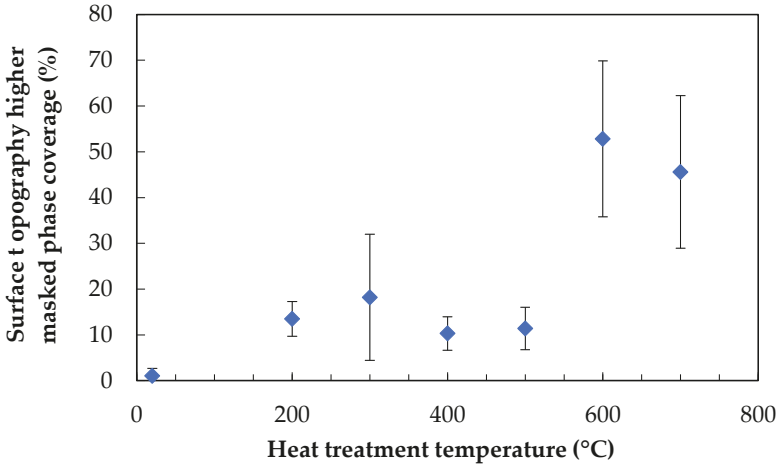

Figure 10. Coverage of the higher (masked) phase of surface topography as a percentage, over heat treatment temperature.

A step change in the coverage percentage was noted; similar values were calculated for lower treatment temperatures of 200–500 °C, followed by a significant increase to 600 and 700 °C, which themselves were similar to one another. This somewhat reflects the observations of the 3D topography plots, in which the appearance of 600 and 700 °C treated fibres were somewhat alike. It is notable, however, that the coverage percentages calculated for 200–500 °C were approximately constant, despite the relatively dissimilar fibre surface topographies. These data highlight a clear step change which occurred between the 500 and 600 °C treatment temperatures.

3.4. Scanning Electron Microscopy

3.4.1. Fibre Surfaces

Images of the fibre surfaces were obtained using SEM, in an attempt to complement the image data from AFM. The consequent loss of quantitative topographical data was compensated by the ability to image large areas of the fibre surface quickly, in contrast to the slow rate of data generation using AFM. Two images of fibres identically thermally conditioned at 700 °C are shown in Figure 11; one obtained using SEM and the other by AFM. From close visual inspection of the images, it appeared clear that the same surface topography was visible, regardless of the method of microscopy used. In image (b) obtained by AFM, a significantly greater contrast in the *z*-axis was evident, as expected.

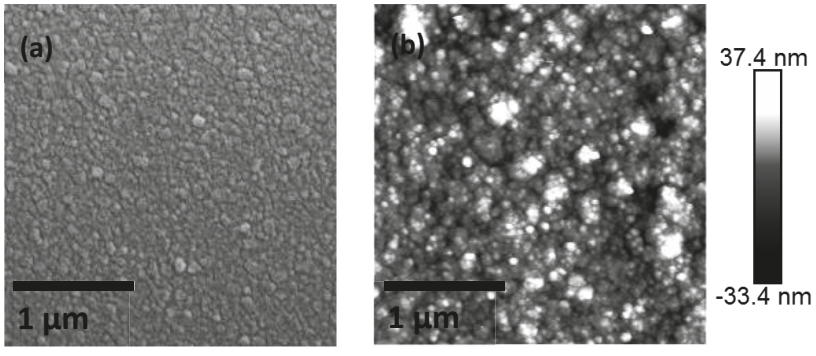

Figure 11. Images of 700 °C conditioned fibres obtained using (**a**) Scanning Electron Microscopy (SEM) and (**b**) Atomic Force Microscopy (AFM).

The surface of the thermally conditioned fibres over a range of temperatures was imaged using SEM. No consistent change of the fibre surface was visible until a temperature of at least 600 °C was used. Although the AFM results showed that roughening occurred at temperatures as low as 200 °C, the resolution of SEM was not sufficient to discern the features until they were of several tens of nm in height. It is possible that this is due in part to the need to coat fibres with a conductive material. Four images of fibre surfaces are presented in Figure 12.

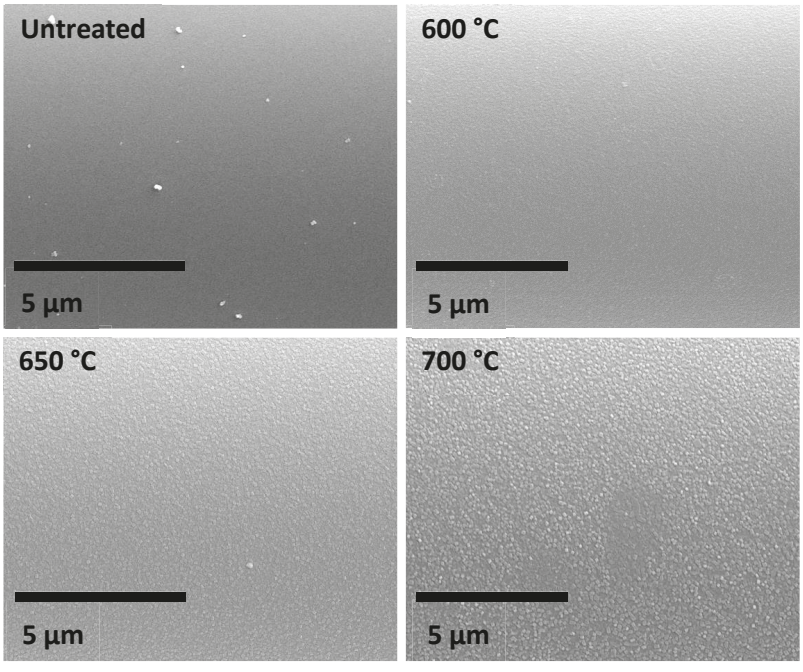

Figure 12. SEM images of E-glass fibre surfaces: untreated and following thermal conditioning at 600, 650 and 700 °C.

The SEM image of the surface of untreated bare glass fibres was found to be largely featureless, except for some small contaminant particles of sub-micron dimensions. Similar particles were observed

by AFM on untreated fibre surfaces; using phase imaging, it was clearly observed that they were distinct and not part of the glass surface (as opposed to the mound-like features of 100–200 nm, which were identical to the surrounding glass surface in the phase images). When the fibres were thermally conditioned at or above 600 °C it was possible to observe the progressive development of features on the fibre surface in the SEM micrographs. As shown by the increase in RMS roughness from AFM (Figure 4) the surface features became progressively easier to discern in SEM images as the conditioning temperature was increased. Significantly, the images provide evidence that the phenomenon occurred across the entire fibre surface; complementing the AFM data, which were captured for only a relatively small surface area on each fibre analysed.

3.4.2. Fracture Surfaces

The fracture surface of both as-received and heat-treated fibres following tensile testing were imaged using SEM. In line with established methods [16] the fractures were examined for visible indications of flaws at which failure was initiated. An example of both non-visible and visible flaws at the fracture origin is presented in Figure 13.

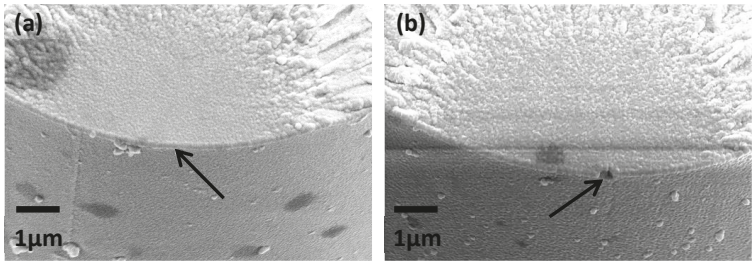

Figure 13. Fracture mirror region of 450 °C heat-treated fibres; (**a**) no visible flaw and (**b**) visible semi-circular flaw at the origin of fracture.

A total of 19 fracture surfaces were imaged with sufficient resolution to be inspected for signs of visible flaws at the origin of fracture. The data are presented in Table 2. Samples were categorised as one of three possible types; no visible flaw at the origin of mirror region; visible flaw at the origin or internal pore at which the fracture appeared to have been initiated.

Table 2. Summary of flaws observed on fracture surfaces produced by failure in pure tension, using both as-received and heat treated E-glass fibres.

Sample	Fracture Surfaces Available	Type 1	Type 2	Type 3
Surface flaw data	No.	No visible origin	Visible origin	Internal pore
Continuous E-glass	19	15	4	0

Unlike the data presented by Lund and Yue [16], no examples were found of fibres with internal pores at which failure occurred. An obvious explanation is that the fibres used in this study were all drawn from bushings, rather than produced by spin-casting. The majority of the mirror regions examined showed no evidence of any flaw at the origin. It is possible that the conductive gold coating may have obscured such features, however great care was taken to apply only a very thin coating to prevent this issue.

4. Discussion

4.1. Chemical Surface Changes

Chemical analysis of the surface of the heat-treated fibres revealed that a consistent trend was measured only for calcium: the concentration increased with increasing treatment temperature, particularly from 500 to 600 °C. This result agrees with the findings of Nichols et al. [17]: they reported that the surface region of E-glass fibres was depleted in calcium with respect to the bulk but that surface concentration of Ca increased when the fibres were heat treated. They proposed that Ca diffused from the fibre bulk to the surface and the evidence reported here is in agreement with such a mechanism. Quantified as the commonly used Ca/Si ratio, our data showed a maximum increase of around 12.5% in Ca/Si following heat treatment at the highest temperature studied, using XPS of 600 °C. This is lower than the almost 19% increase in Ca/Si reported in [17], but this difference may be explained by the shorter heat treatment used in our work. The chemical compositions of the fibres used also differed; Nichols et al. used a boron-containing E-glass, but in this study, a boron-free formulation was used. Our results, therefore, are the first to demonstrate the calcium diffusion and surface enrichment phenomenon for boron-free E-glass.

There exists little to no experimental data in the literature to suggest what effect a change in the surface concentration of Ca might have on the strength of glass fibres. It is understood that increasing the ratio of CaO in a glass blend slightly reduces strength, and the increases modulus of the product fibre [18] but this relates to the total content in the glass, and not the surface concentration. Calcium acts as a network modifier in E-glass, balancing the charge associated with the oxygen ions caused by the incorporation of non-siliceous species into the network, while itself being present in the interstices. A similar interstitial network modifier is sodium, for which some data relating concentration and glass strength exists. Investigated by Kennedy et al. [19] and summarised by Freiman [20], it was found that increasing the concentration of sodium in silica glass produced an increase in fracture toughness. It was postulated that this may be related to changes in straining or bending of Si–O bonds, thus influencing the size of a so-called process zone near the crack tip where elastic fracture mechanics may no longer apply. Even if the increase in Ca concentration after thermal conditioning, which is of relatively small magnitude, had an influence on the retained tensile strength of the fibres, it is unlikely that it would produce a weakening effect. Therefore, while the Ca surface-enrichment phenomenon due to heat treatment has been confirmed for boron-free E-glass for the first time, the phenomenon does not seem to be very likely to be related to fibre strength loss. This conclusion is further supported by the lack of correlation between Ca concentration at the surface, and fibre strength loss with heat treatment temperature.

4.2. Physical Surface Changes

4.2.1. Possibility of Phase Separation

A small number of AFM investigations of the surface of uncoated glasses, including glass fibres, have been reported in the literature [21–24], but the scope of these investigations did not include heat treatment. A systematic analysis of thermally conditioned E-glass fibres by AFM such as that reported here has not previously been conducted. Our surface topography and roughness data do not appear to correlate precisely with the fibre strength loss data presented (Figure 4). This suggests that there may not be a straightforward relationship between the development of roughness at high temperatures and the causes of fibre strength reduction. These data do not appear to support a relationship between increased surface roughness and the development of critical surface flaws. Data obtained on the parameter z_{min} as determined by AFM showed a somewhat better correlation with fibre strength loss (Figure 5) than did surface roughness. If this parameter is interpreted as an indication of flaw depth, however, the magnitudes are many times smaller than theoretical critical flaw sizes that would agree with the experimentally measured fibre strengths. This is explored in greater detail in a later section.

Aside from the issue of representation of flaws from AFM, the surface topography data provide intriguing new evidence of possible surface changes affecting heat-treated glass fibres. The phenomenon of phase separation in bulk glasses has been well studied and reported in the literature. The possibility of phase separation in glass fibres, however, has almost never been addressed, aside from a single paper on lithium alumino-silicate fibres from almost 50 years ago [25]. There is a body of literature that describes the phase separation of siliceous glasses; such studies often employ simplified binary glass systems [26,27] but more complex glasses have also been studied [27–29]. Phase separation following nucleation and growth or spinodal decomposition processes have both been reported, with an apparent dependence on the glass composition used. This is well summarised in a study by Wheaton and Clare [27] in which the sodium silicate and alkali borosilicate glasses analysed showed phase separation by spinodal decomposition, and nucleation and growth, respectively.

The 2D topography graphs presented in Figures 7 and 8 bear resemblance to those in [27]: the heights of the peaks increased with the severity of the heat treatment, and the number of peaks per μm decreased. This is shown most clearly at 700 °C (Figure 8), where the coalescence of smaller individual peaks into only a few larger ones was observed. Significant differences remain between these data, and those that might be described as an 'ideal' example of phase separation. This may be explained, however, as the glass fibres used in our investigation were not etched in hydrofluoric acid, which is commonplace in similar studies [27,28]. A clear height contrast due to differential etching rates of phases was therefore not achieved in the topography plots reported here. It is also possible that the process observed was not fully developed, as the heat treatment time of approximately 20 min was relatively short.

As samples were not acid-etched before AFM analysis, it was not possible to easily discern high and low areas of topography. The use of bearing analysis in NanoScope Analysis, however, made it possible to classify the surface into two regions in a reproducible manner. Examples of heat-treated glass fibres whose high topography regions are masked, is shown in Figure 9. Quantitative analysis of surface coverage of the higher phase is presented in Figure 10. The coverage percentage of the untreated fibres was effectively zero: these fibre surfaces were also the most challenging on which to carry out the analysis, as they suffered from the greatest amount of surface contamination by a significant margin. Fibres that were treated at 200–500 °C produced a coverage percentage of the higher phase of between 10–20%; this increased significantly to between 45–53% for fibres that were heat-treated at 600 or 700 °C. The fibre surface areas in Figure 9 for 600 and 700 °C showed the similar coverage percentages, but also the coalescence of surface features that were also presented in Figure 8. The relatively constant area over this temperature range, in addition to the decreasing interfacial area between the high and low phases, would be consistent with a spinodal decomposition mechanism [30]. The heat treatment times used in our investigation were significantly shorter than those commonly used in studies of phase separation of siliceous glasses; however, such studies have always used bulk glass rather than glass fibres. The significantly larger surface area-to-volume ratios of the glass fibres used in our study may explain the possible occurrence of spinodal decomposition over a shorter than usual time scale.

4.2.2. Effects Relating to Water

Heat treatment at a temperature of 200 °C caused a fivefold increase in roughness compared to the untreated fibre surface. This significant roughening may be a product of surface water on fibres [31,32] plus applied heat; even water alone at room temperature is sufficient to produce significant fibre roughness over longer timescales [24]. In any case, this temperature range is not of the greatest interest, as only a small decrease in fibre tensile strength was measured. The increase in roughness found at higher temperatures of 400 °C and above is unlikely to be related to surface water: it has been demonstrated that the adsorbed surface water is removed upon heating to a temperature of approximately 350 °C [33]. Rather than water adsorbed at the surface, Nishioka [33] presents some evidence of diffusion of water from within the glass bulk structure out to the surface at temperatures

in excess of 550 °C. The process may continue up to and beyond the glass transition temperature. No further exploration of this phenomenon appears to have been undertaken; it is thus unclear in what form the detected water is present in the glass structure. Diffusion of water into glasses has been studied at length, and it has been shown that water can be present in silica glass as hydroxyl, or in its molecular form [34,35]. It remains possible that at high temperatures, pairs of hydroxyls react to produce molecular water, which diffuses out of the structure. The reaction is usually presented as shown in Equation (1):

$$H_2O + SiOSi \leftrightarrow SiOH + HOSi \quad (1)$$

The reaction described is reversible, and local equilibrium depends on the conditions. As temperature increases or local vapour pressure decreases, the reaction in Equation (1) shifts to the right hand side, or in other words, the solubility of molecular water decreases [36]. This water will either react to form additional silanols, or alternatively, it may diffuse out from the structure, as found by Nishioka [33]. In either case, the physical processes involving water appear to occur in the glass fibre structure at the same relatively high temperatures which are associated with fundamental fibre strength loss. The role of water in thermally induced strength loss of glass fibres has not been directly investigated, but it must remain a possible contributing mechanism. In other studies water has been established to possess a significant influence over the strengths of glasses and glass fibres; it has a weakening effect on freshly manufactured glass fibres at room temperature [37], but inversely, it can, at elevated temperatures, be used to increase the strength of weakened glass [38,39].

4.3. Fibre Strength Loss and Fracture Behaviour

The results presented in Figure 1 describe the fundamental strength loss of bare E-glass fibres due to only thermal effects. The single-fibre heat treatment process used minimises possible surface damage to fibres by mechanical means, such as fibre–fibre or fibre–surface interactions. The latter can be avoided in any fibre testing procedure, provided that sufficient care is taken, but the former will inevitably occur if thermal conditioning is performed on fibre bundles. It has been shown that the method of heat treatment selected has a significant effect on the retained fibre strength over a wide temperature range of 200–600 °C [7]. Additional mechanical damage can occur when single fibre tensile specimens are extracted from heat-treated bundles, adding to the fundamental strength loss from thermal effects.

It is this fundamental strength loss that is of particular interest, as a satisfactory explanation for the phenomenon has yet to be presented in the literature. Glass fibres are brittle materials, and this is not changed after their exposure to elevated temperatures. Their failure, therefore, should be based on a discussion of flaws or cracks. The failure behaviour can be described adequately by relatively simple models, such as Griffith's theory [12]. This is often expressed mathematically in combination with Irwin's [40] stress intensity factor for opening mode loading in plane strain cases to yield Equation (2):

$$K_{Ic} = \sigma_f Y \sqrt{\pi a} \quad (2)$$

In Equation (2), K_{Ic} is the material fracture toughness in $N/m^{3/2}$, σ_f is the failure stress in N/m^2 and 'a' is the critical dimension of a flaw which may be straight-edged, circular, or elliptical. The dimensionless parameter Y is defined by the geometry of the flaw-initiating failure, which is usually obtained by direct observation; corresponding values may be found in ASTM C1322-05b. Within this theoretical framework, a decrease in fibre strength implies that during thermal conditioning, either new, more severe, flaws develop, or pre-existing flaws grow. Such growth might consist of an increase in the critical flaw dimension 'a', or a change in the flaw geometry that causes failure at decreased stress. An alternative possibility to explain a decrease in strength might also be a reduction in the mode I fracture toughness; however, some evidence has been presented suggesting that toughness is not changed after the thermal conditioning of E-glass fibres [41].

Fractographic analysis of single glass fibres is relatively challenging and time consuming; perhaps for this reason, there are few papers where sufficient data were collected to allow for useful quantitative analysis [16,42]. The data presented in Table 2 confirm the finding of [16], that the majority of the fracture mirror regions do not have observable signs of a flaw at which the failure originated. Our data, however, show this to be true for a commercial continuous E-glass, rather than for the cascade spun materials in [16]. All failures appeared to originate at the surface, as expected for a brittle material such as glass fibre, whose failure is governed by the surface flaw distribution.

A few visible flaws were found during fractography; an example is given in Figure 13b. In this case, the flaw dimensions give an almost perfect agreement between the theoretical fibre strength—according to Equation (2)—and the measured strength from testing, which are both 1.2 GPa. While it is occasionally possible to identify such surface flaws on fracture surfaces, they have never been identified on pre-fracture glass fibres. The AFM study of heat-treated fibres that were not tensile-tested was intended to discover if surface flaws could be imaged, in addition to providing data on any other changes in surface topography and roughness.

The minimum height measured below the z = 0 plane in topography plots, labelled z_{min}, was analysed, and the data are presented in Figure 5 and Table 3. The two datasets in Figure 5 correlate relatively well across the temperature range used. At lower treatment temperatures the fibre tensile strength was relatively stable but the average z_{min} fluctuated greatly between room temperature (untreated) and 400 °C. The most critical strength loss began after heat treating to 450–500 °C, whereas the flaw depth over the same approximate range increased only slightly. The region in which the trend was relatively similar was 500–700 °C in which both the fibre tensile strength and the average flaw depth decreased rapidly. Table 3 shows that the magnitudes of the average z_{min} measured by AFM were significantly smaller than those that would be required to produce failure at a stress consistent with the average values measured and presented in Figures 1, 4 and 5. The disparity between the theoretical strength, based on Equation (2), and using the average z_{min} depth as the critical flaw, and the measured strength was at least 2, but generally of the order ≥ 4. The disparity in theoretical flaw size is even greater at around ≥ 16, due to the square root in Equation (2).

Table 3. Comparison of measured average strengths of heat-treated fibres, with calculated strengths based on z_{min} values taken from AFM topography of heat-treated fibres.

Treatment Temperature (°C)	Measured Avg. Strength (GPa)	Avg. z_{min} (nm)	Calculated Strength (GPa)	Calculated Strength (GPa)
			Y = 1.12	Y = 1.29
200	1.42	−8.5	5.0	4.3
300	1.31	−22.2	3.1	2.7
400–450	1.12	−11.9	4.2	3.7
500	0.83	−14.8	3.8	3.3
600	0.66	−21.4	3.1	2.7
700	0.31	−31.7	2.6	2.2

The systematic topography study produced data that suggests the existence of physical changes at the fibre surface that have not previously been described, but they did not produce unambiguous evidence of a critical surface flaw. Although troughs below the mean surface (z = 0) were found in all images, their magnitudes were significantly too small to represent critical flaws. Further, although they generally tended to increase in depth as the average fibre strength decreased, the correlation between these was not precise over the temperature range investigated. This may suggest that AFM is not able to measure surface flaws on glass fibres that have not been fractured. A possible explanation is that the surface flaws on the unstressed fibres are too closed to be detected. The geometry of the tip used to characterise surface topography always places some limits on the resolution that may be detected. The tip radius and the front, back and side angles of the tip combine to produce these

geometric constraints. In the case of the analysis presented, the tip radius was approximately 8 nm and the relevant angles between 15–25°. If, for simplicity, the surface flaw is imagined as a slot with straight sides, then it must be greater than 8 nm across to be detected. Even when small flaws can be detected, if they are relatively narrow and deep, the probe will be unable to approach the bottom. For example, the average measured strength of a 200 °C treated fibre, 1.42 GPa, requires a theoretical flaw depth of at least 78 nm; for the AFM probe to touch the bottom of this flaw, it would need to have a width of at least 57 nm.

Alternatively, the low sampling rate that can realistically be achieved in AFM analysis is problematic: for example, if only two areas of 9 μm^2 are analysed on a nominal 17 μm diameter fibre of length 20 mm, this represents just one thousandth of 1% of the total surface area. The likelihood, then, of positioning the AFM probe above a site that contains the critical surface flaw of the fibre length—or any flaw even approaching it—is low. Even if it were possible to analyse along the entire length of such a fibre in a reasonable timescale, only the topmost section can be imaged due to mounting constraints, giving analysis of just over 5% of the fibre surface area.

5. Conclusions

The fundamental strength loss due to the thermal effects of bare E-glass fibres heat-treated between 200–700 °C has been presented. Chemical and physical changes at the surface of these fibres were analysed by using a variety of techniques, in an attempt to understand how they might contribute to the observed fibre strength decrease. An increase in the surface concentration of calcium was detected at 600 °C; it did not, however, correlate with fibre strength loss behaviour. Fibre surface roughness increased significantly with heat treatment temperature, while an inverse trend was found for the depth of topographical features below the z = 0 plane, z_{min}. Neither of these trends correlated closely with fibre strength loss, except between 500–700 °C, where fibre strength and z_{min} decrease and surface roughness increases rapidly. It was found that the values of z_{min} from topography data corresponded to theoretical failure strengths of greater than the actual measured value by a factor of at least four, in the majority of cases. It was concluded that AFM was unable to effectively image surface features that might represent a critical surface flaw, since the high magnification and limited sampling rate that can be achieved severely limits the probability of finding such a critical surface flaw. Alternatively it is possible that surface flaws are too close to each other in an unstressed fibre to be detected by AFM. The fractography data presented showed that, for the large majority of fracture surfaces, it is not possible to observe the flaws that induced the failures. Although AFM analysis was not successful in directly imaging the critical surface flaws of un-fractured fibres, it revealed significant surface changes that occur when glass fibres are thermally conditioned. The nature of these changes suggests that phase separation may be occurring at the glass fibre surface at high temperatures. Evidence for this was found at treatment temperatures of 600–700 °C, although the initial stages of this phase separation may already be present at 400–500 °C. This phenomenon occurs over the same approximate temperature range as that causing the most significant fibre strength loss. Further investigation of this phenomenon, including its relation to a decrease in fibre strength, might further improve our understanding of the fundamental thermally-induced strength loss mechanism.

Author Contributions: Conceptualization, James L Thomason, Liu Yang and Peter G Jenkins; Methodology, James L Thomason and Peter G Jenkins; Formal analysis, Peter G Jenkins and Xinyong Chen; Investigation, Peter G Jenkins, Xinyong Chen and Steven J Hinder; Resources, James L Thomason, Xinyong Chen and John F Watts; Writing—original draft preparation, Peter G Jenkins; writing—review and editing, Liu Yang, James L Thomason, Xinyong Chen and Steven J Hinder; Supervision, James L Thomason; Funding acquisition, James L Thomason.

Funding: This research was funded by the Engineering and Physical Sciences Research Council, grant number EP/I038616/1.

Acknowledgments: The authors would also like to thank Owens Corning for providing the glass fibres used in this study. Special thanks are given to the Advanced Materials Research Laboratory (AMRL) at the University of Strathclyde for the use of SEM equipment.

Conflicts of Interest: The authors declare no conflict of interest.

References

1. Li, H.; Watson, J.C. Continuous Glass Fibers for Reinforcement. *Encycl. Glas. Sci. Technol. Hist. Cult.* **2016**, in press.
2. Job, S.; Leeke, G.A.; Mativenga, P.T.; Oliveux, O.; Pickering, S.J.; Shuaib, N.A. Composites recycling: Where are we now? *Composites UK Ltd.* **2016**, 1–11.
3. Pickering, S.J. Recycling technologies for thermoset composite materials—current status. *Compos. Part. A Appl. Sci. Manuf.* **2006**, *37*, 1206–1215. [CrossRef]
4. Oliveux, G.; Dandy, L.O.; Leeke, G.A. Current Status of Recycling of fibre reinforced polymers: Review of technologies, reuse and resulting properties. *Prog. Mater. Sci.* **2015**, *72*, 61–99. [CrossRef]
5. Kennerley, J.R.; Fenwick, N.J.; Pickering, S.J.; Rudd, C.D. The properties of glass fibers recycled from the thermal processing of scrap thermoset composites. *J. Vinyl Addit. Technol.* **1997**, *3*, 58–63. [CrossRef]
6. Kennerley, J.R.; Kelly, R.M.; Fenwick, N.J.; Pickering, S.J.; Rudd, C.D. The characterisation and reuse of glass fibres recycled from scrap composites by the action of a fluidised bed process. *Compos. Part A Appl. Sci. Manuf.* **1998**, *29A*, 839–845. [CrossRef]
7. Jenkins, P.G.; Yang, L.; Liggat, J.J.; Thomason, J.L. Investigation of the strength loss of glass fibre after thermal conditioning. *J. Mater. Sci.* **2015**, *50*, 1050–1057. [CrossRef]
8. Thomason, J.L.; Yang, L.; Meier, R. The properties of glass fibres after conditioning at composite recycling temperatures. *Compos. Part A Appl. Sci. Manuf.* **2014**, *61*, 201–208. [CrossRef]
9. Feih, S.; Boiocchi, E.; Mathys, Z.; et al. Mechanical properties of thermally-treated and recycled glass fibres. *Compos. Part B Eng.* **2011**, *42*, 350–358. [CrossRef]
10. Thomason, J.L.; Jenkins, P.G.; Yang, L. Glass fibre strength—A review with relation to composite recycling. *Fibers* **2016**, *4*, 18. [CrossRef]
11. Sakka, S. Effect of reheating on strength of glass fibers. *Bull. Inst. Chem. Res.* **1957**, *34*, 316–320.
12. Griffith, A.A. The phenomena of rupture and flow in solids. *Philos. Trans. R. Soc. A. Math. Phys. Eng. Sci* **1921**, *221*, 163–198. [CrossRef]
13. Thomas, W.F. An investigation of the factors likely to affect the strength and properties of glass fibres. *Phys. Chem. Glas.* **1960**, *1*, 4–18.
14. Cameron, N.M. The effect of environment and temperature on the strength of E-glass fibres. Part 2. Heating and ageing. *Glas Technol.* **1968**, *9*, 121–130.
15. Yang, L.; Thomason, J.L. Effect of silane coupling agent on mechanical performance of glass fibre. *J. Mater. Sci.* **2012**, *48*, 1947–1954. [CrossRef]
16. Lund, M.D.; Yue, Y. Fractography and tensile strength of glass wool fibres. *J. Ceram. Soc. Jpn.* **2008**, *116*, 841–845. [CrossRef]
17. Nichols, D.; Hercules, D.M.; Peek, R.C.; Vaughan, D.J. Application of x-ray photoelectron spectroscopy to the study of fiberglass surfaces. *Appl. Spectrosc.* **1974**, *28*, 219–222. [CrossRef]
18. Korwin-Edson, M.L.; Hofmann, D.A.; McGinnis, P.B. Strength of high performance glass reinforcement fiber. *Int. J. Appl. Glas. Sci.* **2012**, *3*, 107–121. [CrossRef]
19. Kennedy, C.R.; Bradt, R.C.; Rindone, G.E. Fracture mechanics of binary sodium silicate glasses. In *Fracture Mechanics of Ceramics*; Bradt, R.C., Evans, A.C., Hasselman, D.P.H., Lange, F.F., Eds.; Springer: Boston, MA, USA, 1974; Volume 2, pp. 883–893.
20. Freiman, S.W. The Fracture of glass: Past, present, and future. *Int. J. Appl. Glas. Sci.* **2012**, *3*, 89–106. [CrossRef]
21. El Achari, A.; Ghenaim, A.; Wolff, V.; Caze, C.; Carlier, E. Topographic study of glass fibers by atomic force microscopy. *Text. Res. J.* **1996**, *66*, 483–490. [CrossRef]
22. Radlein, E.; Frischat, G.H. Atomic force microscopy as a tool to correlate nanostructure to properties of glasses. *J. Non Cryst. Solids* **1997**, *222*, 69–82. [CrossRef]
23. Gupta, P.K.; Inniss, D.; Kurkjian, C.R.; Zhong, Q. Nanoscale roughness of oxide glass surfaces. *J. Non Cryst. Solids* **2000**, *262*, 200–206. [CrossRef]
24. Mellott, N.P.; Pantano, C.G. A mechanism of corrosion-induced roughening of glass surfaces. *Int. J. Appl. Glas. Sci.* **2013**, *4*, 274–279. [CrossRef]

25. Aslanova, M.S.; Shaina, Z.I. Influence of phase separation on physical and chemical properties of heat-treated fibers. In *Phase-Separation Phenom. Glas. Proc. first All-Union Symp. Phase-Separation Phenom*; Porai-Koshits, E.A., Ed.; Glas: Leningrad, Russia, 1968; pp. 168–171.
26. Kreidl, N.J.; Maklad, M.S. Effect of water content on phase separation in soda-silica glasses. *J. Am. Ceram. Soc.* **1969**, *52*, 508–509. [CrossRef]
27. Wheaton, B.R.; Clare, A.G. Evaluation of phase separation in glasses with the use of atomic force microscopy. *J. Non Cryst. Solids* **2007**, *353*, 4767–4778. [CrossRef]
28. Dalmas, D.; Lelarge, A.; Vandembroucq, D. Quantitative AFM analysis of phase separated borosilicate glass surfaces. *J. Non Cryst. Solids* **2007**, *353*, 4672–4680. [CrossRef]
29. Zheng, W.; Lin, M.; Cheng, J. Effect of phase separation on the crystallization and properties of lithium aluminosilicate glass-ceramics. *Glass Phys. Chem.* **2013**, *39*, 142–149. [CrossRef]
30. Varshneya, A.K. *Fundamentals of Inorganic Glasses*; Academic Press: Cambridge, MA, USA, 2013.
31. Carman, L.A.; Pantano, C.G. Water-vapor adsorption on calcium-boroaluminosilicate glass fibers. *J. Non Cryst. Solids.* **1990**, *120*, 40–46. [CrossRef]
32. Nishioka, G.M.; Schramke, J.A. Desorption of water from glass fibers. In *Mol. Charact. Compos. Interfaces*; Ishida, H., Kumar, G., Eds.; Plenum Press: New York, NY, USA, 1985; pp. 387–400.
33. Nishioka, G.M. Adsorption/desorption of water on glass fiber surfaces. *J. Non Cryst. Solids* **1990**, *120*, 34–39. [CrossRef]
34. Oehler, A.; Tomozawa, M. Water diffusion into silica glass at a low temperature under high water vapor pressure. *J. Non Cryst. Solids* **2004**, *347*, 211–219l. [CrossRef]
35. Amma, S.I.; Kim, S.H.; Pantano, C.G. Analysis of water and hydroxyl species in soda lime glass surfaces using Attenuated Total Reflection (ATR)-Ir spectroscopy. *J. Am Ceram. Soc.* **2016**, *99*, 128–134. [CrossRef]
36. Lezzi, P.J.; Xiao, Q.R.; Tomozawa, M.; et al. Strength increase of silica glass fibers by surface stress relaxation: A new mechanical strengthening method. *J. Non Cryst. Solids* **2013**, *379*, 95–106. [CrossRef]
37. Martin, D.M.; Akinc, M.; Oh, S.M. Effect of forming and aging atmospheres on e-glass strength. *J. Am. Ceram. Soc.* **1978**, *61*, 308–311. [CrossRef]
38. Li, H.; Tomozawa, M. Mechanical strength increase of abraded silica glass by high pressure water vapor treatment. *J. Non Cryst. Solids* **1994**, *168*, 287–292. [CrossRef]
39. Wiederhorn, S.M.; Yi, F.; LaVan, D.; Richter, L.J.; Fett, T.; Hoffmann, M.J. Volume expansion caused by water penetration into silica glass. *J. Am. Ceram. Soc.* **2015**, *98*, 78–87. [CrossRef]
40. Irwin, G.R. Fracture. In *Elast. Plast.*; Flugge, S., Ed.; Springer: Heidelberg, Germany, 1958; pp. 551–590.
41. Feih, S.; Mouritz, A.P.; Case, S.W. Determining the mechanism controlling glass fibre strength loss during thermal recycling of waste composites. *Compos. Part A Appl. Sci. Manuf.* **2015**, *76*, 255–261. [CrossRef]
42. Jaras, A.C.; Norman, B.J. The measurement of glass fibre strength in composites from studies of their fracture surfaces. *J. Mater. Sci.* **1983**, *18*, 2459–2465. [CrossRef]

fibers

MDPI

Article

Chitosan as a Coupling Agent for Phosphate Glass Fibre/Polycaprolactone Composites

Chao Tan [1,2], Chris Rudd [2,3], Andrew Parsons [3], Nusrat Sharmin [2], Junxiao Zhang [2], Wanru Chen [1,2] and Ifty Ahmed [4,*]

1 International Doctoral Innovation Centre, University of Nottingham Ningbo China, Ningbo 315100, China; chao.tan@nottingham.edu.cn (C.T.); wanru.zhang@nottingham.edu.cn (W.C.)
2 Ningbo Nottingham New Materials Institute, University of Nottingham Ningbo China, Ningbo 315100, China; chris.rudd@nottingham.edu.cn (C.R.); nusrat.sharmin@nottingham.edu.cn (N.S.); zy15730@nottingham.edu.cn (J.Z.)
3 Composites Research Group, Healthcare Technologies, Faculty of Engineering, University of Nottingham, Nottingham NG7 2RD, UK; andrew.parsons@nottingham.ac.uk
4 Advanced Materials Research Group, Healthcare Technologies, Faculty of Engineering, University of Nottingham, Nottingham NG7 2RD, UK
* Correspondence: ifty.ahmed@nottingham.ac.uk; Tel.: +44-0115-7484675

Received: 5 November 2018; Accepted: 30 November 2018; Published: 10 December 2018

Abstract: This study shows that chitosan (CS) could be highly useful as a coupling agent in phosphate glass fibre/polycaprolactone (PGF/PCL) composites, as it improved the interfacial shear strength by up to 78%. PGFs of the composition $45P_2O_5$–$5B_2O_3$–$5Na_2O$–24CaO–10MgO–$11Fe_2O_3$ were dip-coated with CS (with a degree of deacetylation >80%) dissolved in acetic acid solution (2% v/v). Different CS concentrations (3–9 g L^{-1}) and coating processes were investigated. Tensile and fragmentation tests were conducted to obtain the mechanical properties of the single fibres and interfacial properties of the PGF/PCL composites, respectively. It was observed that post-cleaning, the treated fibres had their tensile strength reduced by around 20%; however, the CS-coated fibres experienced strength increases of up to 1.1–11.5%. TGA and SEM analyses were used to confirm the presence of CS on the fibre surface. FTIR, Raman, and X-ray photoelectron spectroscopy (XPS) analyses further confirmed the presence of CS and indicated the protonation of CS amine groups. Moreover, the nitrogen spectrum of XPS demonstrated a minimum threshold of CS coating required to provide an improved interface.

Keywords: chitosan; coupling agent; phosphate glass fibre; polycaprolactone (PCL) composite

1. Introduction

Much work so far has focused on phosphate glass fibre (PGF)-reinforced polymers as a substitute for metal implants in bone tissue engineering, in order to achieve sufficient mechanical properties, biodegradability, and biocompatibility [1,2]. Moreover, fibre-reinforced composites present high stiffness and strength per weight when compared with other structural materials, along with adequate toughness. The reinforcement of resins with short or long fibres has multiple applications in various biomedical fields, especially in medicine [3] and dentistry [4]. However, the application of polymer composites, such as PGF/PCL, is limited by the rapid loss of their strength profiles after exposure to an aqueous physiological environment, which has been suggested to be due to loss of their interfacial properties [5]. Recently, coupling agents have been explored to enhance the interfacial properties of fibre/polymer composites [6,7]. Chitosan (CS) has a number of properties that make it a suitable candidate as an interface agent for PGF/PCL composites.

Chitosan is the second most abundant natural polysaccharide next to cellulose and can be produced from discarded crab and shrimp shells [8]. It is the N-deacetylated derivative of chitin with

a typical degree of deacetylation of over 0.5, and it is a semicrystalline polymer in the solid state [9]. In dilute acidic solutions (below pH 6), CS is readily soluble due to the protonation of the amine groups, which makes CS a water-soluble cationic polyelectrolyte [9]. The amino functional groups of CS can participate in chemical reactions such as acetylation, chelation of metals, reactions with aldehydes, ketone alkylation, grafting, and so forth, and the hydroxyl groups also facilitate reactions such as *o*-acetylation, hydrogen bonding with polar atoms, and grafting, among others [10]. These reactive functional groups make CS outstanding in the biocomposite field, with applications such as in blends with other polymers [11], organic coupling agents [12], nanocomposites [13], and reinforced collagen structures [14].

CS has generated enormous interest in biomedical applications due to its biodegradability and biocompatibility [8,9]. For example, Copper et al. [15] investigated the fabrication and application of CS–PCL fibres for nerve tissue regeneration. They reported a good polymer compatibility between CS and PCL and achieved better cellular compatibility compared to PCL products. Zhang et al. [16] produced CS scaffolds for bone tissue engineering and used phosphate calcium invert glasses as the reinforcing filler. They found that the CS scaffolds with the calcium phosphate glass fillers had a smoother surface and smaller pores with roughly circular shape. Therefore, they inferred that not only the physical incorporation of the secondary phases occurs, but ionic complexes may also form between the fillers and the CS, due to its high surface charge. These examples revealed a good interaction between CS and both biopolymers and phosphate glasses, which suggested the potential of CS as a coupling agent to improve the interface of PGF-reinforced polymer composites, such as might be used for orthopaedic implants [17]. To the authors' best knowledge, no study has yet been published exploring the application of CS as a coupling agent.

Therefore, this study investigated the feasibility of CS as a coupling agent for PGF/PCL composites. It was hypothesised that CS would have a good connection with PGF via hydrogen, P–O–C, and/or N–P bonding [18,19]. Dilute acetic acid was used as a solvent for CS, which may also impact the mechanical properties of PGFs [20]. However, this impact could be controlled in terms of coating time and solution concentration. Mechanical properties of the coated and uncoated fibres were ascertained using a single-fibre tensile test (SFTT). The interfacial shear strength (IFSS) was analysed using a single-fibre fragmentation test. Thermogravimetric analysis (TGA) was used for the detection and quantification of the CS coating on the fibres. Morphologic examination was performed via SEM. FTIR, Raman, and X-ray photoelectron spectroscopy (XPS) analyses were conducted in order to investigate the chemical interaction between the CS and PGFs. Finally, the CS-modified PGF/PCL composites would be developed into composite bone plates for orthopaedic applications. The PGFs can completely degrade in the aqueous solution, as can the polymer matrix. Cell culture analysis and mechanical property studies have already been done and published [1,2].

2. Materials and Methods

2.1. Phosphate Glass and Fibre Preparation

Phosphate glass ($45P_2O_5$–$5B_2O_3$–$5Na_2O$–24CaO–10MgO–$11Fe_2O_3$ in mol%) was prepared as described previously [21]. An in-house facility was used to prepare ~25-µm diameter continuous fibres via a melt–draw spinning process [22].

2.2. Coating Application

A 2% *v*/*v* acetic acid solution was prepared by mixing glacial acetic acid (purity >99.7%, Fisher Scientific, Hampton, NH, USA) into Ultrapure Milli-Q water (Merck KGaA, Darmstadt, Germany) [23]. The CS coating solution was then prepared by dissolving 0.3–0.9 g of CS powder (low molecular weight (Mw), the degree of deacetylation (DD) > 80%, Sigma Aldrich, St. Louis, MO, USA) in 100 mL of the acetic acid solution, stirring in hermetically sealed glassware to prevent evaporation of acetic acid, until a transparent, viscous solution was obtained. PGFs were dip-coated in

the coating solution and subsequently dried in an oven overnight at 50 °C, before proceeding with tensile testing and single-fibre composite (SFC) preparation.

Five groups were prepared for comparison. Three of them (PCP-3, -6, and -9; PCP means PGF–chitosan–PCL) were treated using the same coating process with different CS concentrations. PCP-3R was post-cleaned after coating, i.e., the coated PGFs were immersed in 100 mL 2% v/v acetic acid solution and lightly shaken to remove excess CS on the fibre surface. Uncoated PGFs (PCP-0) were also placed in the oven and prepared as a control. Full details of the coating applications are shown in Table 1.

Table 1. Details of coating applications. The sample codes were also used for the corresponding single-fibre composites (SFCs).

Sample Codes		PCP-0	PCP-3R	PCP-3	PCP-6	PCP-9
Acetic acid solution	mL	-	100	100	100	100
CS	g	-	0.3	0.3	0.6	0.9
Dip-coating at RT	min	-	30	30	30	30
Drying at RT	hour	-	2	2	2	2
Post-cleaning	min	-	30	-	-	-
Drying at 50 °C	hour	24	24	24	24	24

* PCP means PGF–chitosan–PCL; R in "PCP-3R" means "removing excess chitosan"; CS means chitosan; RT means room temperature around 25 °C.

2.3. Single-Fibre Composite (SFC) Preparation

PCL films were prepared by compression moulding from granulated PCL (Mw 65,000, Esun, Shenzhen, China), which was dried in an oven at 50 °C for 24 h before processing. Eight grams of the dried PCL was placed between two steel plates with polytetrafluoroethylene (PTFE) as a release film. Then, the steel plates were moved into a hydraulic press (ZhengGong, Zhengzhou, China), preheated at 120 °C for 5 min, hot-pressed under 23 bar at 120 °C for 40 s, and cold-pressed under 23 bar at room temperature for 2 min. The resulting PCL films (thickness of 0.15–0.20 mm) were cut into dimensions of 75 mm × 25 mm.

SFCs were prepared via a similar compression moulding process. A single fibre was axially aligned between two prepared PCL films in the mound and fixed at both ends using heat-resistant adhesive tape. Then, the mould was preheated at 120 °C for 10 min, hot-pressed under 14 bar at 120 °C for 10 min, and cold-pressed under 14 bar at room temperature for 2 min. The resulting SFC was cut into a dog-bone specimen of total dimensions 63 mm × 10 mm × 0.25 mm using a dog-bone cutter (Keruite, Kunshan, China), with the gauge section being 25 mm × 5 mm.

2.4. Single Fibre Tensile Test (SFTT)

SFTTs were conducted in accordance with ISO 11566 [24]. Thirty individual filaments were mounted onto plastic tabs for each sample type. The filaments were bonded to the tabs using a UV-cured acrylic adhesive (Dymax, Wiesbaden, Germany). The gauge length was 25 mm.

Measurements of fibre diameter were conducted using an FDAS 770 fibre micrometre (Diastron, Andover, UK), configured with an LSM 6200 laser scan micrometre (Mitutoyo, Kanagawa, Japan). Before measurements, the micrometre was calibrated with a glass fibre of known diameter, determined by a Sigma/VP SEM with ×1000 magnification (Zeiss, Jena, Germany), and the error on each diameter measurement was taken to be ±0.3 μm. The value of diameter was obtained from the average of three measurements of the fibre. The SFTT was performed using a LEX 820 tensile tester (Diastron, Andover, UK) at room temperature with a load cell capacity of 1 N and a crosshead speed of 1 mm min^{-1} [25]. The Weibull distribution is an accepted statistical tool with which to characterise the failure of brittle fibres [25]. The normalising stress and Weibull modulus are referred to as the scale and shape parameters, respectively. The normalising stress describes the most probable stress at which

a brittle fibre of the gauge length will fail [26]. Minitab 17 (Minitab Inc., State College, PA, USA) was used to calculate Weibull parameters from the tensile strength data.

2.5. Single-Fibre Fragmentation Test (SFFT)

The interfacial shear strength (IFSS) was measured from SFCs by using the SFFT method. Dog-bone specimens were axially loaded in an E45 tensile testing machine (MTS, Eden Prairie, MN, USA) with a load cell of 1 kN and a crosshead speed of 1 mm min^{-1} until the strain increased independently of the axial stress [25].

The PCL samples prepared were not transparent enough to see the fibre fragments using a microscope after the tensile tests. Hence, the samples were sandwiched between two glass slides and heated at 70 °C for 2–5 min on a hot plate to melt the PCL so that it became transparent. Then, the number of fibre fragments within the gauge length was tallied under an NE 930 optical microscope (Nexcope, Ningbo, China).

The IFSS values were calculated using the Kelly–Tyson equation [25]:

$$\tau = \frac{\sigma_f \cdot d}{2 \cdot l_c} \tag{1}$$

where τ is the IFSS, d is the fibre diameter, and σ_f is the single-fibre tensile strength at the critical fragment length l_c, determined by:

$$\sigma_f = \sigma_0 \cdot \left(\frac{l_c}{l_0}\right)^{-1/m} \tag{2}$$

$$l_c = \frac{4}{3} \cdot l_f \tag{3}$$

$$l_f = \frac{l_0}{N} \tag{4}$$

where m and σ_0 are the Weibull shape and scale parameter, respectively, for the fibre strength at gauge length l_0. N is the number of fibre fragments and l_f is the average fragment length, obtained using optical microscopy.

2.6. Statistical Analysis

Statistical analysis was performed using version 22 of SPSS (IBM, New York, NY, USA). The significance of difference between different samples was analysed using a Student's unpaired t-test, assuming equal variance and determining two-tailed p values [21]. Comparison of the significance of change in one factor with CS concentration was performed by using one-way analysis of variance (ANOVA), calculated with the Bonferroni post-test [22]. The Kolmogorov–Smirnov (K–S) test was used to assess whether the samples follow a Gaussian distribution. The threshold value chosen for statistical significance was the 0.05 level.

2.7. SEM

Fibres were fixed on the sample stage by using conductive adhesive tape and were then coated with gold using an EM SCD 500 high-vacuum sputter coater (Leica, Welzlar, Germany). The stage with sample was placed into a Sigma/VP SEM (Zeiss, Jena, Germany). The micrographs were taken at an accelerating voltage of 3 kV using SE (secondary electron) mode.

2.8. Thermogravimetric Analysis (TGA)

TGA was performed using an SDT Q600 thermogravimetric analyser (TA Instruments, New Castle, DE, USA). The CS powder and coated/uncoated fibres were heated from room temperature to 500 °C, below the glass transition temperature (T_g) of the PGF, being around 520 °C [21]. A heating rate of 20 °C min^{-1} in flowing nitrogen gas of 50 mL min^{-1} was used for the experiment.

2.9. FTIR and Microscope FTIR

Infrared spectroscopy was performed on the CS powder and chopped fibres using a Vertex 70 FTIR spectrometer (Bruker, Ettlingen, Germany), while a Cary 660 FTIR Spectrometer coupled with a Cary 620 FTIR Microscope (Agilent Technologies, CA, USA) was used for precise analysis of the excess coating on the fibre bundle.

All the samples were scanned in the region of 4000 to 400 cm^{-1} with a scan resolution of 4 cm^{-1} for 32 scans using the Attenuated Total Reflectance (ATR) system, and analysed by using Opus software version 7.0 (Bruker, Ettlingen, Germany). Spectra were background-corrected.

2.10. Raman

Raman spectra in the range of 100–3500 cm^{-1} were taken at room temperature using an inVia-Reflex Raman spectrometer coupled with an inVia Raman Microscope (Renishaw, Gloucestershire, UK) and equipped with a 785 nm laser diode. The spectra of CS powder and chopped fibres were obtained and then analysed by using WIRE software (Version 2.0, Renishaw, Gloucestershire, UK).

2.11. XPS

An Axis Ultra (Kratos, Manchester, UK) with a monochromated AlK_α X-ray source (1486.6 eV) was operated at 8 mA emission current and 12 kV anode potential. For the XPS measurement, a fibre bundle was mounted on the sample stage using a conductive adhesive tape at both ends, while the CS powder was adhered on the stage by using conductive tape. Drift of the electron binding energy of the peaks caused by surface charging was calibrated by using the C_{1s} peak of the C–C bond at 284.5 eV.

3. Results

3.1. Mechanical Properties

As shown in Figure 1, the tensile modulus of PCP-0, -3R, -3, -6, and -9 were 72 ± 3, 73 ± 3, 72 ± 3, 69 ± 3, and 71 ± 6 GPa, respectively. No significant change was found for the modulus between the uncoated and coated fibres. Tensile strength of the fibres are shown in Figure 1 and Table 2. Table 2 also represents the fibre diameters and Weibull parameters. It was observed that the tensile strength of PCP-3R was reduced by 20.2% ($p < 0.001$) compared to the control (PCP-0), while there was no significant difference between the tensile strength of PCP-3 and PCP-0. Moreover, the tensile strength of PCP-6 and -9 were 1.1% and 11.5% higher than the control, respectively. Thus, the tensile strength of coated fibres was observed to have a positive correlation with the CS concentration. Statistical analysis further demonstrated the significance of this increase ($p < 0.05$).

Table 2. Diameters and Weibull parameters of coated/uncoated fibres (n = 30). The tensile strength values are also included for the ease of comparison.

Sample Codes	Diameter (μm)	Tensile Strength (MPa)	Normalising Strength (MPa)	Weibull Modulus
PCP-0	26 ± 4	565 ± 124	613	5.5
PCP-3R	24 ± 3	451 ± 114	495	5.5
PCP-3	25 ± 2	522 ± 104	565	5.3
PCP-6	26 ± 3	571 ± 120	619	5.3
PCP-9	25 ± 2	630 ± 111	675	6.7

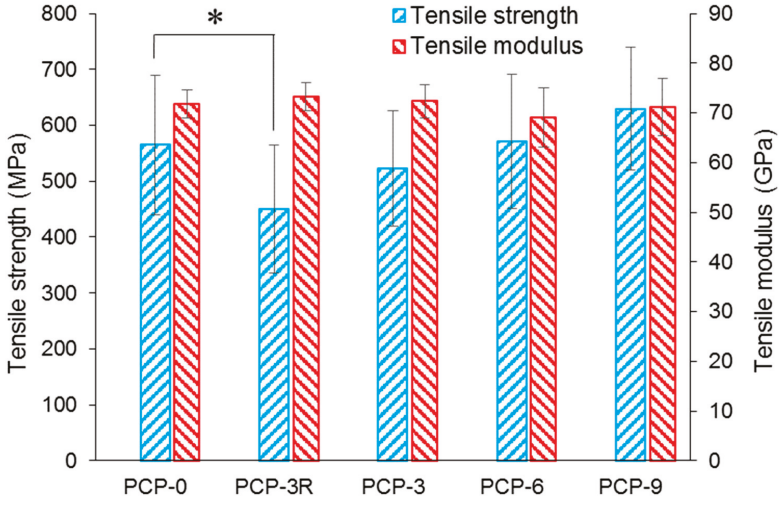

Figure 1. Mechanical properties (tensile strength and modulus) of coated/uncoated fibres (n = 30). The statistical significance of the paired t-test is indicated (*) at the $p < 0.05$ level.

It was observed from Table 2 that the trend of the mean tensile strength was consistent with that of the normalising strength. The Weibull modulus of the fibres ranged between 5.3 and 6.7. The fibre diameters were around 25 μm, and no significant change in diameter was observed between coated and pristine fibres.

3.2. IFSS Analysis

As shown in Figure 2, the interfacial shear strength (IFSS) of PCP-3R (9.97 ± 2.21 MPa) increased by 78% ($p < 0.001$) compared to the control, PCP-0 (5.59 ± 0.50 MPa). In contrast, the IFSS of PCP-3 (8.72 ± 1.88 MPa) increased by 56% ($p < 0.001$) compared to PCP-0. Moreover, no statistical significance was found for the difference in IFSS between PCP-3, -6, and -9.

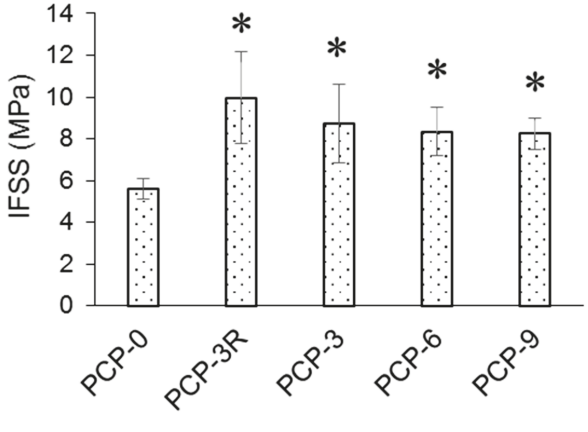

Figure 2. Interfacial shear strength (IFSS) obtained from fragmentation tests (n = 10). The statistical significance of the paired t-test at $p < 0.05$ was illustrated (*) compared to PCP-0.

3.3. SEM Analysis

SEM was used to investigate the morphology of the fibres after the application of CS and also to compare the surface of the coated and uncoated fibres. As shown in Figure 3a, the surface of the uncoated PGF (PCP-0) was smooth, whilst some CS attachment was observed on the surface of all the coated fibres (see Figure 3b–e). Moreover, the attachment of CS on PCP-3, -6, and -9 (see Figure 3c–e) appears as a "seam" (for an example, see the white arrow depicted in image Figure 3e). The difference in surface condition between PCP-3R and -3 (see Figure 3b,c) represented the effect of post-cleaning and removing of the excess CS attached to the fibres. In addition, no cracks or pits were observed in any of the samples tested.

As shown in Figure 3c, excess attachment of CS was observed as a seam on the PCP-3 fibre, and otherwise, the coating on the fibre surface seemed to be uniform. The blistering and skinning appearances indicated by white arrows in Figure 3f were generated under a prolonged exposure to the electron beam and suggested the presence of a CS coating. The white arrow in Figure 3g indicates the connection between two filaments, which was suggested to be formed by the presence of excess CS on the fibre surface.

3.4. TGA

Figure 4 represents the change in weight percentage of CS powders and glass fibres as a function of temperature. A derivative of the weight percentage curve (Wt%/°C versus °C) is also presented for a further analysis of decomposition temperature. Figure 4a shows the TGA results of the CS powders, where two apparent peaks were observed on the derived Wt curve of CS at 86 and 310 °C, respectively. The weight loss in the temperature between 230 and 400 °C was observed to be 43%, which was caused by the decomposition of CS [27]. Figure 4b exhibits TGA traces of the coated and uncoated fibres. A peak at ~300 °C was observed on the derived Wt curves of PCP-3, -6, and -9. One more peak was found at ~160 °C for PCP-6 and -9. In addition, an obvious weight loss was found for PCP-3, -6, and -9 below 100 °C. Table 3 shows the corresponding peaks of derived Wt curves for CS powders and glass fibres. The weight loss behaviour was observed to be composed of three stages. Table 3 also shows the weight loss of CS powders and glass fibres heated from 230 to 400 °C. A greater weight loss was observed with increasing CS concentration (from PCP-3 to PCP-6 and -9), and a reduced weight loss was found after the post-cleaning (from PCP-3 to PCP-3R).

Table 3. Peaks of the Deriv. Wt (the derivative of weight percentage) curves and weight loss in the temperature region of 230–400 °C (n = 3).

Sample Codes	PCP-0	PCP-3R	PCP-3	PCP-6	PCP-9	CS
Peaks on Deriv. Wt (°C)	-	-	<100	<100	<100	86 ± 0
	-	-	-	159 ± 8	159 ± 2	-
	-	-	279 ± 1	293 ± 3	291 ± 4	308 ± 3
Wt loss at 230–400 °C (%)	0 ± 0	0.02 ± 0.01	0.50 ± 0.01	1.98 ± 0.05	5.8 ± 0.2	43 ± 2

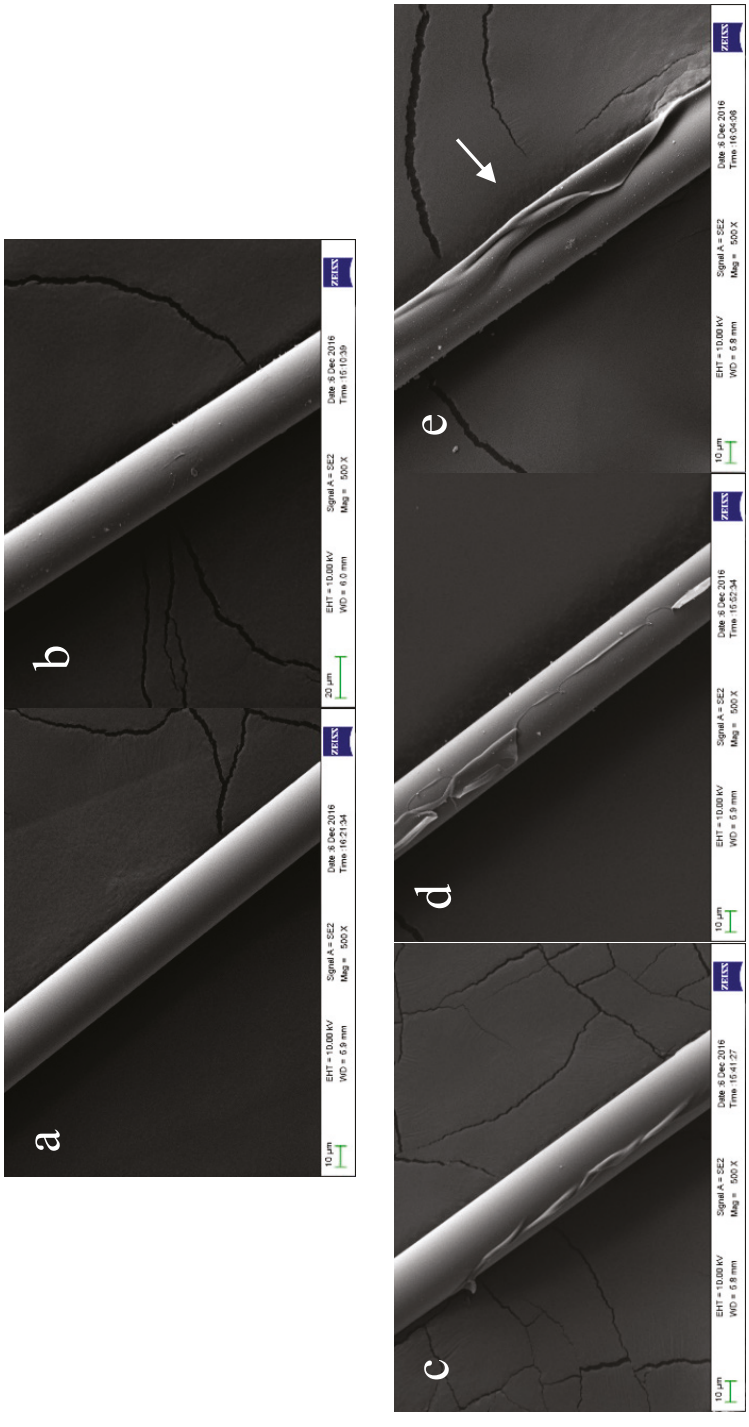

Figure 3. *Cont.*

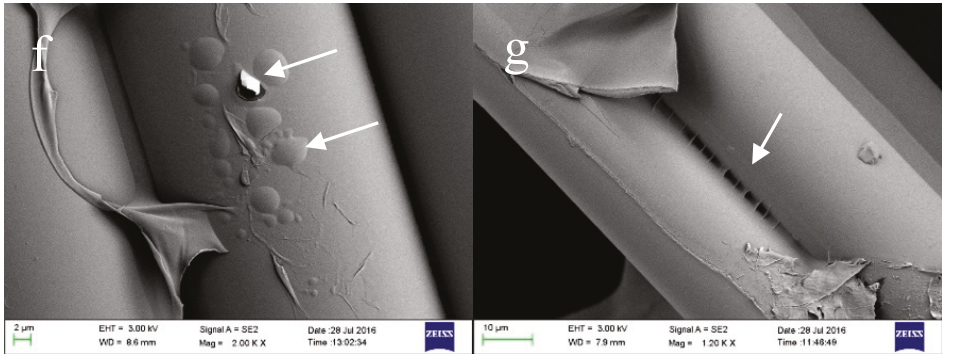

Figure 3. SEM images of coated/uncoated phosphate glass fibres (PGFs). Subfigures (**a**–**e**) show PCP-0, -3R, -3, -6, and -9, respectively; the scale-length of **a** = 10 µm, the magnification (Mag) of **a** = 500×, and (**a**–**e**) share the same factors. (**f**) shows blistering of the PCP-3 fibre surface heated by the electron beam; the scale-length of **f** = 2 µm and the Mag of **f** = 2000×. (**g**) shows two combined PCP-3 filaments; the scale-length of **g** = 10 µm and the Mag of **g** = 1200×. The cracked base shows the conductive tape.

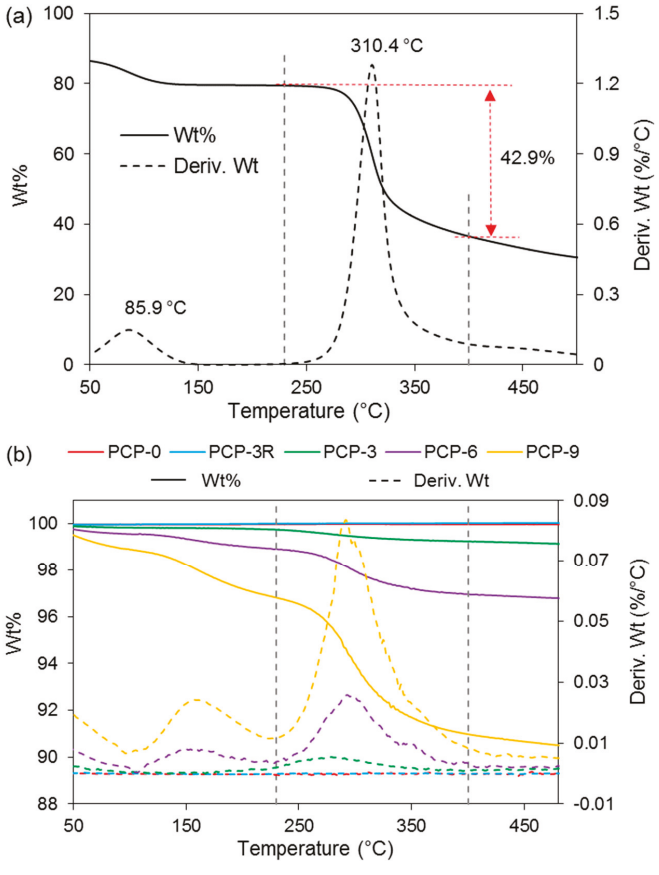

Figure 4. Weight percentage and derivative of weight percentage (Deriv. Wt) for (**a**) CS powder and (**b**) coated/uncoated PGFs. The main weight loss was observed between 230 and 400 °C. The red dashed line and arrow in (**a**) were added for eyes guide.

3.5. FTIR Analysis

3.5.1. Microscope-FTIR

IR analysis was performed on the "seam" (CS-S) of the coated fibres to characterise the excess coating on the fibre (see the seam in Figure 3e. The comparison between CS-P and CS-S in Figure 5 found a decrease in band absorption intensity around 1027 and 3358 cm^{-1} in the spectra of CS-S. The band around 561 cm^{-1} observed in CS-P disappeared in CS-S. Moreover, the bands of CS-P at 1151, 1648, 3291, and 3358 cm^{-1} were also observed in the spectrum of CS-S. The bands at 1027, 1063, 1315, 1375, 2873, and 2917 cm^{-1} were found to shift to higher wavenumbers for CS-S as compared to CS-P, while the band observed at 1419 cm^{-1} shifted to a lower wavenumber. The band at 1589 cm^{-1} disappeared for CS-S and a new band was found at 1560 cm^{-1}. Peak assignments are provided in Table 4.

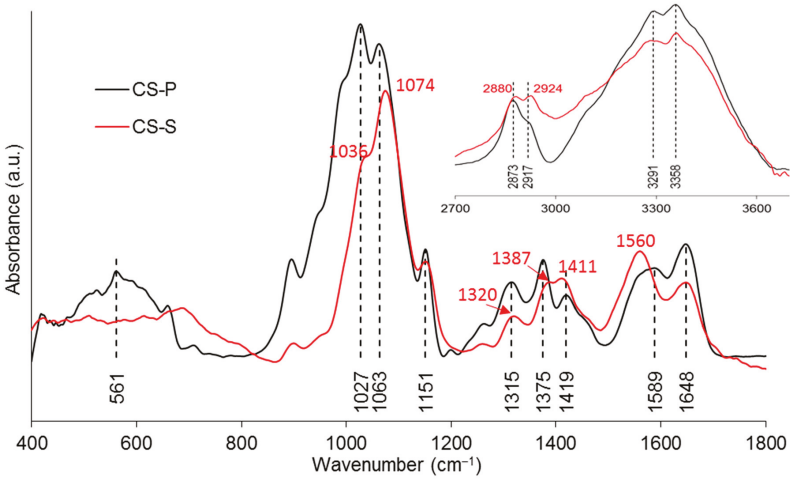

Figure 5. FTIR spectra of the CS powder used for coating (CS-P) and the "seam" on the PGFs (CS-S).

Table 4. FTIR and Raman band assignments for pure PGF and CS.

Wavenumber (cm^{-1})	Assignments	Ref.
	FTIR–PGF	
495	δ_{as}(O–P–O) in Q^1 species	[28,29]
754, 894	υ_s and υ_{as}(P–O–P) of the bridging oxygen in Q^2 species	[29,30]
~1040	υ_s and υ_{as}($P–O^-$) in Q^1 species	[29,30]
~1200	$\upsilon_{as}(PO_2)^-$ of the nonbridging oxygen in Q^2 species	[28,31]
	FTIR–CS	
1027, 1063	υ(C–O) in the pyranose ring	[11,32]
1151	υ_{as}(C–O–C) in the glycosidic linkage	[11,32]
1315	$\upsilon(CH_2)$	[33]
1375	symmetric deformation mode of CH_3	[11,34]
1419	δ(C–H)	[33,35]
1589	$\delta(NH_2)$	[32,33]
1648	υ(–C=O–) in the amide group	[11,35]
2873, 2917	υ(C–H)	[11,33]
3291, 3358	υ_s(N–H) and υ_s(O–H)	[11,33]
	Raman–PGF	
353	$\delta(PO_4)$ of phosphate polyhedra	[36,37]
450–650	δ_s and $\delta_{as}(PO_2)^{2-}$ in Q^0 species	[38,39]
736	υ_s(P–O–P) of the bridging oxygen in Q^1 species	[37,38]
946	υ_{as}($P–O^-$) of the nonbridging oxygen in Q^0 species	[37,39]
1097	$\upsilon_{as}(P_2O_7)^{4-}$ in Q^1 species	[39]
~1250	$\upsilon_{as}(PO_3)^-$ of the non-bridging oxygen in Q^2 species	[36,38]
	Raman–CS	
898	υ_s(C–O–C) in the pyranose ring	[40,41]
1106	υ(C–O–C) in the glycosidic linkage and υ(C–C)	[42,43]
1266	υ(CH)	[41]
1375	$\delta(CH_2)$	[41,44]
1459	$\delta_{as}(CH_3)$	[40,41]
1596	$\delta(NH_2)$	[41,44]
1659	υ(C=O) in the amide group	[44,45]
2734, 2889, 2933	υ(CH), $\upsilon(CH_2)$, and $\upsilon(CH_3)$	[41,44]
3305	$\upsilon(NH_2)$	[40,41]
δ_s (δ_{as}) = symmetric (asymmetric) bending vibration υ_s (υ_{as}) = symmetric (asymmetric) stretching vibration		

3.5.2. ATR-FTIR

IR analyses were also performed on the coated fibres to investigate the chemical interaction between the CS coating and the PGF surface. The bands of uncoated PGFs (PCP-0) were taken as the control and the bands of pure CS powders were used as references. The band assignments are listed in Table 4.

Figure 6a shows that the main bands of PCP-0 were observed at 495, 754, 894, and ~1040 cm^{-1}. Shifts towards lower wavenumbers were observed for the bands at 495 and 754 cm^{-1} for all the coated fibres. It was also obvious that the bands at 894 cm^{-1} shifted to a lower wavenumber in PCP-3, -6, and -9, while no evident change was found on the band at 1040 cm^{-1}.

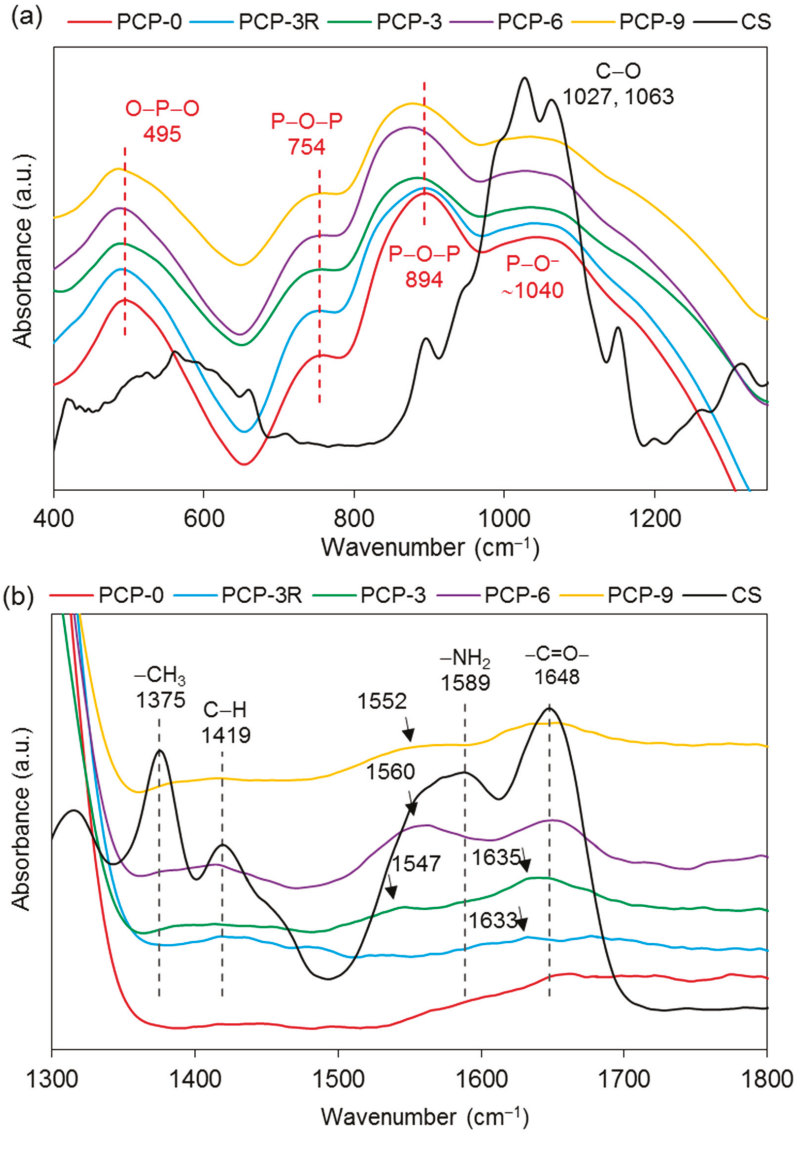

Figure 6. *Cont.*

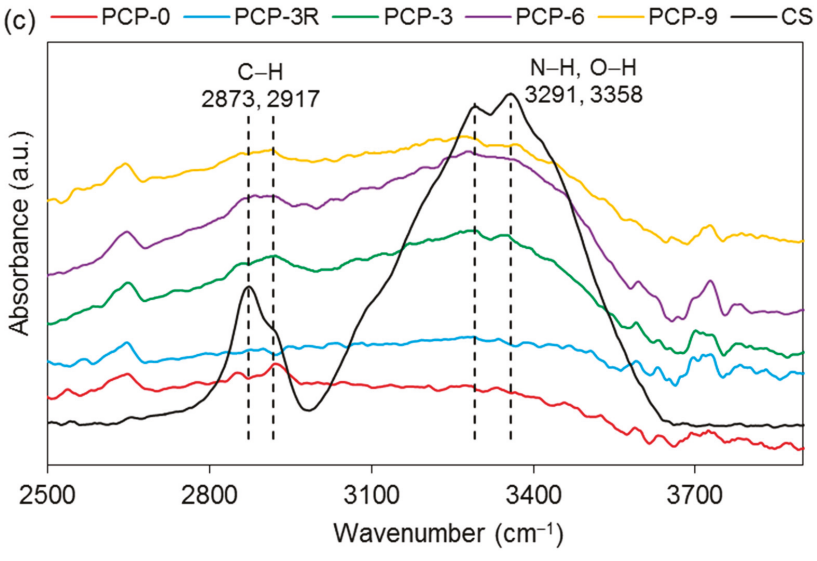

Figure 6. FTIR spectra of the coated/uncoated fibres and the pure CS powder at the band range of (**a**) 400–1300 cm^{-1}, (**b**) 1300–1800 cm^{-1} and (**c**) 2500–3800 cm^{-1}.

As shown in Figure 6b, the absorption bands of CS at ~1648 cm^{-1} were found only in PCP-3, -6, and -9, and a new band was also found at ~1633 cm^{-1}. The band at 1589 cm^{-1} disappeared in the spectra of all the coated fibres, while a new band appeared at 1547, 1560, and 1552 cm^{-1} for PCP-3, -6, and -9, respectively.

Absorption bands at 2873, 2917, 3291, and 3358 cm^{-1} were observed in PCP-3, -6, and -9, and a significant decrease in absorption intensity was observed at 3291 and 3358 cm^{-1} for the coated fibres as compared to CS (see Figure 6c).

3.6. Raman Analysis

Raman analyses was performed on the coated/uncoated fibres and the CS powder. The bands in the spectra of PGFs were observed in the range of 300–1400 cm^{-1}. As shown in Figure 7a, the bands located at 353, 736, 946, and 1097 cm^{-1} were unchanged for the coated fibres compared to PCP-0. The intensity of the bands at 946, 1097, and ~1250 cm^{-1} were observed to decrease for PCP-3R, -3, -6, and -9, especially the band at 1097 cm^{-1}. The broad band observed at 450–650 cm^{-1} was considered to be an overlapping of peaks, which were difficult to distinguish. The band assignments are listed in Table 4.

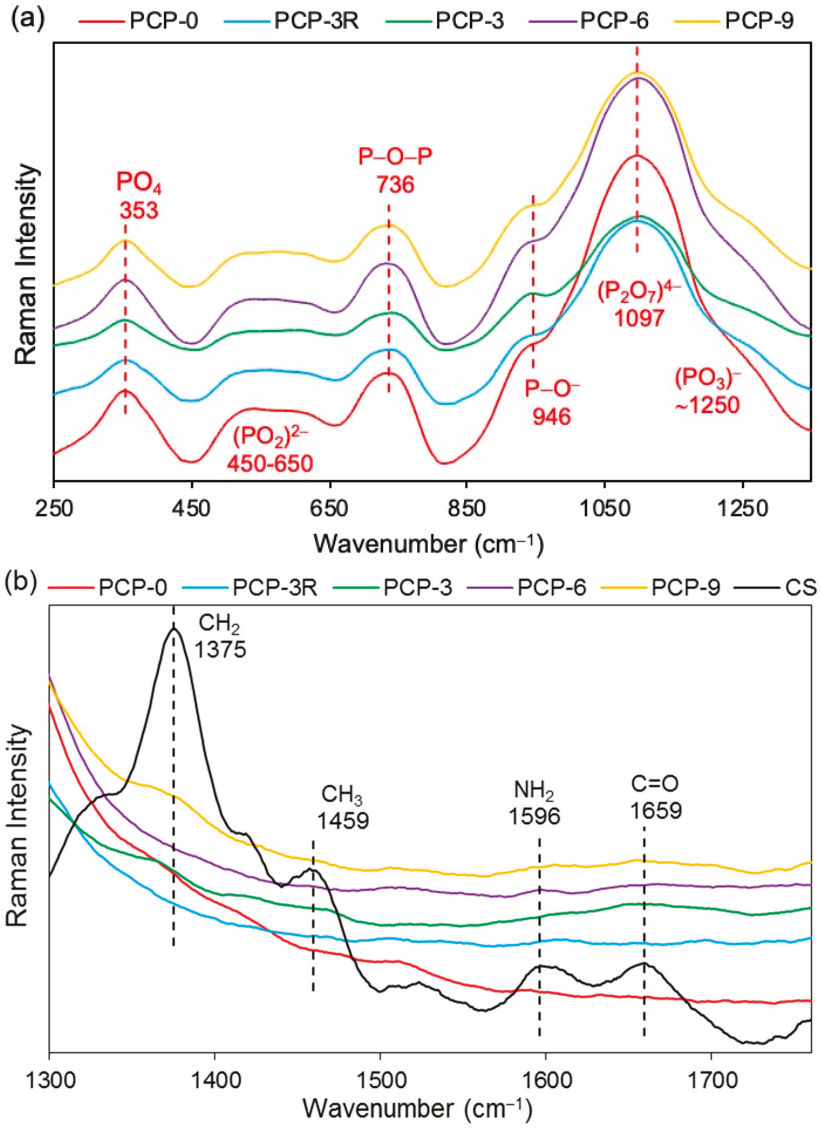

Figure 7. *Cont.*

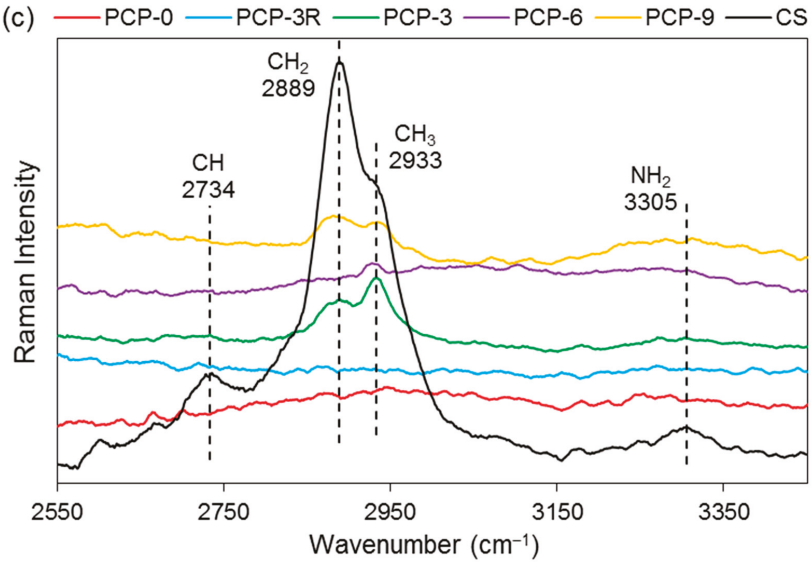

Figure 7. Raman spectra of the coated/uncoated fibres and the pure CS powder at the band range of (**a**) 250–1300 cm^{-1}, (**b**) 1300–1750 cm^{-1} and (**c**) 2550–3400 cm^{-1}.

As shown in Figure 7b, four bands were observed at 1375, 1459, 1596, and 1659 cm^{-1} in CS. The bands at 1596 and 1659 cm^{-1} were also observed for PCP-6 and -9 with much lower intensities compared to CS. However, only the band at 1659 cm^{-1} was observed for PCP-3, while neither of the two bands at 1596 and 1659 cm^{-1} were found in PCP-0 and -3R.

Figure 7c shows the bands of CS at 2734, 2889, 2933, and 3305 cm^{-1}. A decrease in the band intensity of 2889 and 2933 cm^{-1} were observed in PCP-3, -6, and -9. The bands at 2734 and 3305 cm^{-1} were observed to disappear in the spectra of all the coated fibres.

3.7. XPS Analysis

High-resolution XPS spectroscopy was performed on the coated/uncoated fibres and the CS powder. Narrow scans of C_{1s}, O_{1s}, N_{1s}, and P_{2p} are exhibited in Figure 8. In the C_{1s} scan of CS, the carbon peak was deconvoluted into three signals at 284.5, 286.0, and 287.6 eV binding energy. Similar peaks were also observed in the spectrum of PCP-3R, -3, -6, and -9.

The nitrogen peak in the spectrum of CS was deconvoluted into two signals, involving the main peak at 399.1 eV and a much smaller peak at 400.7 eV binding energy. Their atomic ratios were 95 and 5%, respectively. The peak at 399.2 ± 0.1 eV was also found in the spectrum of PCP-3R, -3, -6, and -9, whilst a new peak appeared at 401.3 ± 0.1 eV binding energy. Moreover, the atomic ratio of the peak at 401.3 ± 0.1 eV was observed to increase from 40% to 65% as the PCP-3 samples were treated by the post-cleaning process. On the contrary, the atomic ratio of the 401.3 ± 0.1 eV-peak decreased to 17% as the CS concentration increased from PCP-3 to PCP-6. However, the atomic ratio remained constant when the CS concentration increased from PCP-6 to PCP-9. The details of the binding energy and atomic ratio of nitrogen are shown in Table 5.

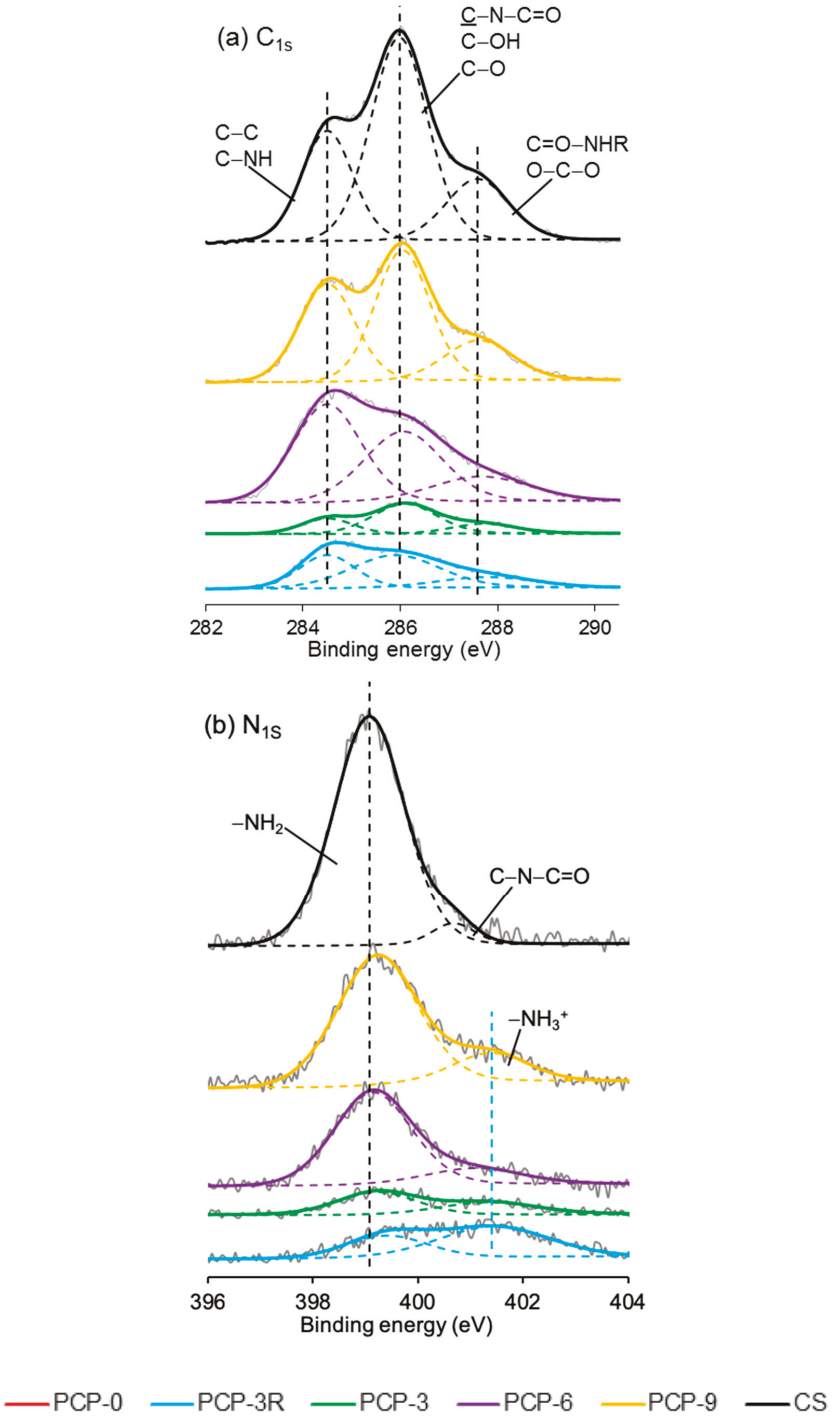

Figure 8. *Cont.*

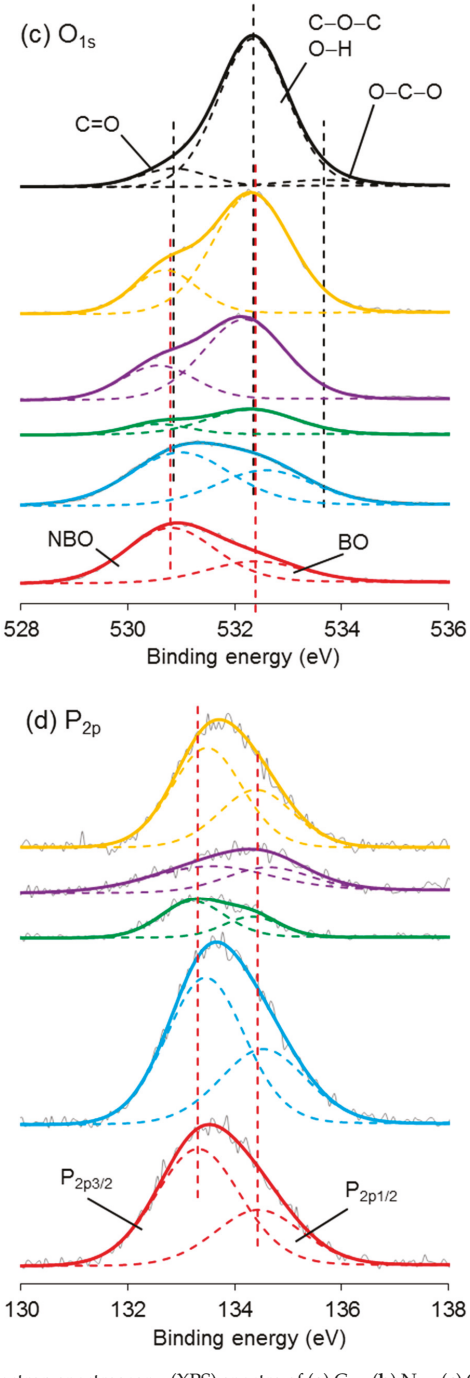

Figure 8. X-ray photoelectron spectroscopy (XPS) spectra of (**a**) C_{1s}, (**b**) N_{1s}, (**c**) O_{1s}, and (**d**) P_{2p} narrow scans of coated/uncoated fibres and pure CS powders.

Table 5. Binding energy and atomic ratio of N_{1s} peaks in XPS spectra.

Sample codes	Binding Energy (eV)	Atomic Ratio
PCP-0	-	-
PCP-3R	399.4; 401.5	35.2:64.8
PCP-3	399.2; 401.3	59.8:40.2
PCP-6	399.1; 401.1	83.2:16.8
PCP-9	399.2; 401.4	82.9:17.1
CS	399.1; 400.7	94.8:5.2

In the O_{1s} spectroscopy, the spectrum of CS required three peaks for the curve fit, including the main peak at 532.3 eV taking 86% of the oxygen atomic ratio and two much smaller peaks at 530.9 and 533.7 eV. The O_{1s} peak of PCP-0 showed two deconvoluted peaks at 530.8 and 532.4 eV binding energy. Due to the absorption peaks over similar ranges of binding energy, it was difficult to differentiate the peaks between PCP-0 and CS in the spectrum of coated fibres. However, as shown in Figure 8c, it was obvious that the signal of CS gradually dominated the peak from PCP-3R to PCP-9.

The P_{2p} peak of PCP-0 was deconvoluted into two peaks at 133.3 and 134.4 eV binding energy. Their atomic ratio was 67:33. Similar peaks were also observed in the spectrum of the coated fibres.

4. Discussion

4.1. Mechanical Properties

The impact on fibre strength caused by the acetic acid solution used for dip-coating and post-cleaning was investigated by a comparison of PCP-0 with PCP-3 and -3R (see Figure 1). There was no significant difference between the tensile strength of PCP-3 and PCP-0, while a significant decrease of 20.2% ($p < 0.001$) in tensile strength was observed for PCP-3R as compared to PCP-0. The degradation of PGF in solution is highly pH-dependent and greatly accelerated at low pH [46]. Potentially, the additional exposure to acid in the post-cleaning process caused additional glass degradation and could have created additional surface flaws, affecting the fibre strength [46].

The mechanical properties of PCP-3, -6, and -9 fibres were compared to investigate the influence of varying CS concentration. As shown in Figure 1, a linear increase in tensile strength was shown to be statistically significant ($p < 0.05$) with respect to the CS concentration. The CS did not contribute significantly to the fibre modulus, due to there being only a thin coating and having a much lower modulus than the glass. However, Gao et al. [47] stated that the CS coating could make contributions to the mechanical properties by reducing the flaw formation and crack growth at the glass fibre surface. Firstly, the CS coating layer could protect the fibre surface from abrasion during sample preparation for tensile testing, as well as moisture/alkali contact and reaction at a crack tip (stress corrosion). Secondly, the protonation of amine groups in CS molecules could decrease the Na^+/H^+ exchange at the fibre surface, and then the positively charged amine groups could absorb the free hydroxyl ions around the fibre surface. Thirdly, the coated CS could have filled any surface flaws present, and in turn, blunt the crack tips. Finally, shrinkage of the CS during drying could have created compressive stresses on the fibre surface, which may have prevented crack initiation/propagation [47].

4.2. Interfacial Properties

As shown in Figure 2, IFSS between the PCL matrix and the PGF significantly increased ($p < 0.001$) for PCP-3, which was suggested to be due to the formation of hydrogen bonds between the hydroxyl groups present at the PGF surface and the amino and hydrogen groups in CS [18]. The phosphate glass immersed in aqueous solution will generate O^- groups at the glass surface due to the rapid release of sodium ions, whilst the CS in low-pH aqueous solution could have generated NH_3^+ groups (see Figure 9) [46]. Strong hydrogen bonds of 20–40 kcal/mol could be formed between the charged donor and acceptor groups that are nearly as strong as covalent bonds [48]. Kohl et al. [49] reported

that glass fibres with native surface hydroxyl groups could have strong hydrogen-bonding interactions (high surface energy) with polar functional groups of the polymers in glass fibre-reinforced composites.

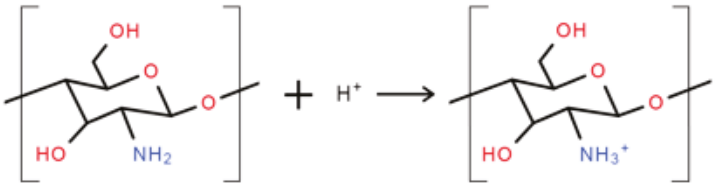

Figure 9. Schematic illustration of the protonation of amine groups in low-pH aqueous solution.

The protonation could have also enabled CS to possess pH-dependent electrostatic interactions with the phosphate groups on the PGFs in a manner similar to amino silane [50]. Huang et al. [51] added glycerol–phosphate to the CS–acetic acid solution and found that the interaction between the NH_3^+ and P–OH groups was caused by electrostatic attraction. Chenite et al. [52] summarised that the combination of CS and polyol–phosphate salts could have formed hydrogen bonding, electrostatic interactions, and hydrophobic interactions in acetic acid solution. Amaral et al. [53] investigated the phosphorylation of CS using XPS and assigned the signal at 401.4 eV in the N_{1s} peak to the amino groups in ammonium form. They proposed that the phosphate groups and the protonated amine groups were likely to form salt linkages with inter- or intrachain ionic bonds.

Zhang et al. [16] reinforced a CS scaffold with P_2O_5–CaO invert glass and suggested that the chemical attraction between CS and the glass may take place due to the high surface charge density of CS. They inferred that not only that the physical incorporation of the glass powders into the CS matrix occurred, but that the chemical complexation between CS and the glass may also occur due to the high surface charge density of CS and its ability to form ionic complexes.

A further increase in IFSS was observed after the post-cleaning treatment, which was employed to remove any excess CS coating on the fibre surface and consequently improved the load transmission between the matrix and fibres (see Figure 2) [54]. However, no evidence of an increase in fibre roughness was observed at the resolution of SEM microscopy after post-cleaning.

The IFSS value reduced from 8.72 to 8.34 MPa when the CS concentration was increased from PCP-3 to PCP-6, whilst it reduced to 8.24 MPa when the CS concentration was increased to PCP-9. This linear reduction may also relate to poorer load transmission from the matrix to the reinforcing fibres caused by the thicker coating. As shown in Figure 2, the effect of CS concentration on the IFSS was relatively small, but cumulative.

Bhattarai et al. [55] investigated CS–PCL polyblend nanofibres in comparison to PCL products. They reported an enhancement in mechanical properties and cellular behaviour without the creation of chemical crosslinking between the CS and the PCL. Copper et al. [15] also achieved better mechanical properties and cellular compatibility from CS-PCL fibres compared to the PCL products alone.

Furthermore, the different profiles of Figures 1 and 2 reveal that the fibre strength increased, but the IFSS decreased with increasing CS concentration. Therefore, an optimal solution can be expected between PCP-3R and -3 to balance the mechanical and interfacial properties during the application of the CS coupling agent.

4.3. SEM Analysis

As shown in Figure 3, the surface of the uncoated fibre (PCP-0) was smooth, while excess attachment was observed on the surface of all the coated fibres (PCP-3R, -3, -6, and -9), which evidenced the presence of a CS coating on the fibres. The difference between Figure 3b,c indicated removal of excess coating by post-cleaning. In addition, no visible cracks or pits were observed on the surface of all the fibres after dipping or post-cleaning treatments.

The blistering and skinning indicated by white arrows in Figure 3f were observed at the fibre surface after a prolonged exposure to the electron beam. This phenomenon was suggested to be associated with the heating on the fibre surface caused by electronic scanning, indicating a heat-sensitive coating layer on the fibre. This was interpreted as further evidence of a polymeric CS layer on the fibres. Furthermore, the connection between two filaments presented in in Figure 3g showed the potential of CS to act as a binder or film former as well as a coupling agent.

4.4. TGA

Zawadzki et al. [27] conducted TGA of CS from room temperature to 600 °C under a nitrogen atmosphere, and suggested that the TGA behaviour of solid CS can be divided into three stages: (1) the removal of water below 100 °C, in which the water was physically adsorbed and/or weakly hydrogen-bonded to CS molecules; (2) the release of strongly hydrogen-bonded water starting above 100 °C and reaching the maximum rate at ~168 °C; and (3) the predominant weight loss by 43% at 230–400 °C caused by the depolymerisation of CS chains, the decomposition of pyranose rings via dehydration and deamination, and finally, a ring-opening reaction. The quantities of weight loss provided in Table 3 indicated the presence of a coating layer on the fibres. The thermal behaviours traced in Figure 4 showed a good agreement with reference [27], further proving the coating layer to be CS.

An increase in weight loss of CS was also shown in Table 3, indicating a thicker CS coating layer with higher CS concentration, which was suggested to be due to the aggregation behaviour of CS polymer chains. The rapid release of alkali (Na^+) in the coating solution introduced negative charge at the fibre surface, which attracted NH_3^+ groups of CS, further leading to an uneven charge distribution of the CS chains caused by asymmetric electron dispersion. Then, the CS coating on the fibre surface was increased by charge attraction and stabilised via intermolecular hydrogen-bonding [27]. Several articles [10,56] have reported that CS can form an entangled network in an acidic aqueous medium by crosslinking with itself and that the crosslinking involves two structural units that may be from the same or from different CS polymer chains.

In addition, the post-cleaning process may have disrupted the intermolecular hydrogen bonds and consequently removed any excess CS, leaving only the firmly bonded CS on the fibre surface [25].

4.5. FTIR and Raman Analyses

As shown in Figure 5, the absorption bands at 3291 and 3358 cm^{-1} were assigned to the stretching vibrations of O–H and N–H, respectively. The intensity of these two bands on CS–S was observed to reduce as compared to CS–P, which was suggested to be due to the formation of intermolecular hydrogen bonds in the excess CS coating [11]. The band of NH_2 at 1589 cm^{-1} was replaced by a new band of NH_3^+ at 1560 cm^{-1} on CS–S, suggesting the formation of hydrogen bonds to balance the change of charges in the excess CS [27]. The bands at 561 and 1063 cm^{-1} could be identified as crystallisation-sensitive bands of CS, and the changes of these bands in wavenumber and intensity that occurred on CS–S implied that an intermolecular interaction between different polymer chains disturbed the crystallisation of CS [34]. The absence of a characteristic band at ~1730 cm^{-1} on CS–S implied that there was no residual COOH group on the fibres after coating application [57].

The band at 495 cm^{-1} shown in Figure 6a was assigned to the asymmetric bending vibration of O–P–O in Q^1 units, and a slight shift to a lower wavenumber occurred for the coated fibres, which might be attributed to the interaction between the pyrophosphate units and the coating [28]. The bands at 754 and 894 cm^{-1} were assigned to the symmetric and asymmetric stretching of P–O–P bridging bonds in Q^2 units, respectively [30]. The latter band was observed to decrease in intensity and shift to a lower wavenumber for the coated fibres, which was suggested to be due to the reduction in Q^2 units, indicating a depolymerisation of metaphosphate units in acid solution. The Raman spectra in Figure 7a also showed a reduction in intensity of the band at 1097 cm^{-1} (the asymmetric stretching vibration of $(P_2O_7)^{4-}$ in Q^1 units [38]) and the shoulder at ~1250 cm^{-1} (the asymmetric stretching

vibration of $(PO_3)^-$ in Q^2 units [39]) for the coated fibres, indicating a decrease in concentration of pyro- and metaphosphate units.

As shown in Figure 6b, the replacement of the band of NH_2 at 1589 cm^{-1} by the new bands appearing at 1547, 1560, and 1552 cm^{-1} on PCP-3, -6, and -9, respectively, was attributed to the protonation of the amine groups in CS [33]. Lawrie et al. [58] reported that partial protonation of NH_2 groups in CS could cause the appearance of a new band at ~1530 cm^{-1} due to one of the NH_3^+ vibrational modes. The difference of the band locations between the literature and this study might be due to the interaction between the charged amine groups and the phosphate units. The Raman spectra in Figure 7b,c show that the bands of the bending (1596 cm^{-1}) and stretching (3305 cm^{-1}) vibrations of NH_2 disappeared for the coated fibres, and this was attributed to the protonation of amine groups, which correlated well with the IR results [41].

Bhumkar et al. [59] investigated the crosslinking of CS with sodium tripolyphosphate in acidic aqueous solution via FTIR. They reported that in the IR spectra of crosslinked CS, the band at 1655 cm^{-1} disappeared and two new bands appeared at 1554 and 1645 cm^{-1}, due to the linkage between the phosphoric and ammonium ions. Therefore, the appearance of the bands at ~1547 and ~1635 cm^{-1} and the intensity reduction of the band at 1648 cm^{-1} for the coated fibres suggested interaction of the NH_3^+ groups with the fibre surface (see Figure 6b). Moreover, it was also suggested that the formation of hydrogen bonding contributed to the interaction between the charged CS and PGFs. Sayyar et al. [60] characterised graphene-filled CS composites using FTIR. They found that the bands corresponding to the N–H bending of the amino group (1573 cm^{-1}), C=O stretching of the amide group (1658 cm^{-1}), and N–H stretching of the amino group (3464 cm^{-1}) in CS shifted to a lower wavenumber in composite films, indicating likely hydrogen-bonding interactions between CS and lactic acid and reduced graphene oxide.

4.6. XPS Analysis

The C_{1s} peaks of CS shown in Figure 8a have a good agreement with the literature [61]. The peak at 284.5 eV was assigned to C–C or C–NH_2; 286.0 eV was assigned to C–O, C–OH, or C–NHC=O; and 287.6 eV was assigned to O–C–O or C=O–NHR chemical bonds. The detection of these signals for the coated fibres indicated the presence of CS on the fibre surface. The minor difference between the spectra of the CS powder and the coated fibres was suggested to be due to contamination carbon on the fibres.

The N_{1s} peak of CS could be resolved into two peaks at 399.1 and 400.7 eV, assigned to the nitrogen of the amino and amide groups, respectively [62]. The atom % of the amino peak was 95%, agreeing well with the degree of deacetylation (DD > 80%) quoted by the supplier. As shown in Figure 8b, the peak of NH_2 was also found for the coated fibres, whilst a new peak of NH_3^+ appeared at 401.3 $\pm$ 0.1 eV binding energy, indicating the partial protonation of the amino groups [62]. Lawrie et al. [58] performed XPS on CS powders from Sigma with a reported 85% degree of deacetylation. They identified the N_{1s} peak as one main signal at 399.4 eV with another weaker signal at 400.5 eV, corresponding to the amino and amide, respectively. They subsequently characterised the acid-treated CS film and detected one more signal at 401.4 eV, attributing to the protonated amine.

As shown in Table 5, the atomic percentage of the NH_3^+ in PCP-3 increased from 40% to 65% after the post-cleaning, supporting the assertion that the post-cleaning process removed excess unreacted CS adsorbed to fibre surface by weak hydrogen bonds. In contrast, the atom % decreased to 17% in PCP-6 with increasing CS concentration, indicating an increasing layer of excess CS. The atomic % was observed to remain constant in PCP-9 as compared to PCP-6, indicating that there was a threshold of concentration of CS interacting with the PGF surface. The changes in the atomic % of NH_3^+ were also observed to be consistent with the IFSS profile shown in Figure 2, which revealed the efficiency of the CS coating.

The O_{1s} spectrum of CS was resolved into one main peak at 532.3 eV and two weak peaks at 530.9 and 533.7 eV. The peak at 532.3 eV was assigned to C–O–C, O–H, or bound water and the two weak

peaks were assigned to C=O in the amide group and O–C–O in the pyranose ring, respectively [61]. The O_{1s} spectrum of PGF was deconvoluted into two peaks at 530.6 and 531.8 eV binding energy, corresponding to the nonbridging and bridging phosphate oxygens, respectively [25]. Although it was difficult to differentiate the subpeaks from the overlapped binding energy range, the signal of CS was seen to dominate the overlapping peak gradually from PCP-3R to PCP-9, which indicated the increase in CS on the fibres, fitting well with the TGA results.

The P_{2p} peak of PGF was composed of the $P_{2p3/2}/P_{2p1/2}$ doublet, and was fitted with an energy difference of 1.1 eV and an approximate atomic ratio of 2:1. The peak of $P_{2p3/2}$ at 133.3 eV was attributed to the pentavalent tetracoordinated phosphorus (pyrophosphate and orthophosphate) surrounded by a different chemical environment (phosphate-like structure), and the peak of $P_{2p1/2}$ at 134.4 eV was attributed to the metaphosphate [63]. The peaks at similar binding energy were also observed for the coated fibres.

In summary: (1) The presence of CS coating on the fibre surface was confirmed via TGA, FTIR, Raman, and XPS analyses. (2) SEM and TGA indicated the formation of a thicker CS coating layer when using the solution of higher CS concentration. (3) The results of tensile tests indicated that the CS coating protected the fibres from losing strength in the acid solution. (4) The results from single-fibre fragmentation tests indicated that CS coupling agents improved the IFSS of the composites, due to the interaction between the protonated amine groups of CS and the hydrogen groups in the fibre surface, as correlated via the analyses of FTIR, Raman, and XPS.

5. Conclusions

CS showed its potential to improve the interface of PGF/PCL composites, in which the protonation of amine groups plays a central role in the interaction between CS and PGF. The nitrogen spectrum of XPS revealed a threshold of efficient CS coating for interfacial improvement. The post-cleaning process could remove the excess CS on the fibre surface and consequently increase the efficiency of the coupling agent.

The coated CS layer showed a significant effect on the fibre surface protection, resulting in a maintenance of mechanical strength after dipping in the acetic acid solution. In addition, TGA and SEM indicated an increase in coating thickness with higher CS concentration in the coating solution. However, a thicker CS layer could also have led to poorer load transmission between the fibre and matrix. Therefore, a balance of the mechanical and interfacial properties would be considered during the application of CS as a coupling agent. This balance is suggested to be achieved by adjusting the CS concentration and the post-cleaning duration.

Author Contributions: C.T. and I.A. conceived the original idea. C.T. carried out the experiment. J.Z. fabricated the PCL film and single fibre composite samples. W.C. supported on the XPS experiment and discussion. C.T. wrote the manuscript with support from I.A., A.P. and N.S. A.P. helped supervise the project. C.R. and I.A. supervised the project.

Funding: The authors kindly acknowledge the financial support from the Ningbo Education Bureau, Ningbo Science and Technology Bureau, China's MOST, and The University of Nottingham. Additionally, the authors also would like to acknowledge financial support from the Ningbo S&T bureau Ningbo International Collaboration Project (project code 2017D10012) and the Ningbo 3315 Innovation team Scheme "Composites Development and Manufacturing for Sustainable Environment".

Acknowledgments: The authors would like to acknowledge all the technical staff of the ITRC and Wolfson Building in UK campus and the SEB in Ningbo campus of Nottingham University, for their guidance and technical assistance.

Conflicts of Interest: The authors declare no conflicts of interest.

References

1. Ahmed, I.; Jones, I.A.; Parsons, A.J.; Bernard, J.; Farmer, J.; Scotchford, C.A.; Walker, G.S.; Rudd, C.D. Composites for bone repair: Phosphate glass fibre reinforced PLA with varying fibre architecture. *J. Mater. Sci. Mater. Med.* **2011**, *22*, 1825–1834. [CrossRef]

2. Parsons, A.J.; Ahmed, I.; Haque, P.; Fitzpatrick, B.; Niazi, M.I.K.; Walker, G.S.; Rudd, C.D. Phosphate glass fibre composites for bone repair. *J. Bionic Eng.* **2009**, *6*, 318–323. [CrossRef]
3. Bas, O.; De-Juan-Pardo, E.M.; Meinert, C.; D'Angella, D.; Baldwin, J.G.; Bray, L.J.; Wellard, R.M.; Kollmannsberger, S.; Rank, E.; Werner, C. Biofabricated soft network composites for cartilage tissue engineering. *Biofabrication* **2017**, *9*, 25014. [CrossRef] [PubMed]
4. Scribante, A.; Vallittu, P.K.; Özcan, M. Fiber-Reinforced Composites for Dental Applications. *Biomed. Res. Int.* **2018**, *2018*. [CrossRef] [PubMed]
5. Hasan, M.S.; Ahmed, I.; Parsons, A.J.; Walker, G.S.; Scotchford, C.A. The influence of coupling agents on mechanical property retention and long-term cytocompatibility of phosphate glass fibre reinforced PLA composites. *J. Mech. Behav. Biomed. Mater.* **2013**, *28*, 1–14. [CrossRef] [PubMed]
6. Mohammadi, M.S.; Ahmed, I.; Muja, N.; Rudd, C.D.; Bureau, M.N.; Nazhat, S.N. Effect of phosphate-based glass fibre surface properties on thermally produced poly(lactic acid) matrix composites. *J. Mater. Sci. Mater. Med.* **2011**, *22*, 2659–2672. [CrossRef] [PubMed]
7. Haque, P.; Barker, I.A.; Parsons, A.; Thurecht, K.J.; Ahmed, I.; Walker, G.S.; Rudd, C.D.; Irvine, D.J. Influence of compatibilizing agent molecular structure on the mechanical properties of phosphate glass fiber-reinforced PLA composites. *J. Polym. Sci. Polym. Chem.* **2010**, *48*, 3082–3094. [CrossRef]
8. Lee, D.W.; Lim, H.; Chong, H.N.; Shim, W.S. Advances in chitosan material and its hybrid derivatives: A review. *Open Biomater. J.* **2009**, *1*, 10–29. [CrossRef]
9. Rinaudo, M. Chitin and chitosan: Properties and applications. *Prog. Polym. Sci.* **2006**, *31*, 603–632. [CrossRef]
10. Pillai, C.K.S.; Paul, W.; Sharma, C.P. Chitin and chitosan polymers: Chemistry, solubility and fiber formation. *Prog. Polym. Sci.* **2009**, *34*, 641–678. [CrossRef]
11. Ramya, R.; Sudha, P.N.; Mahalakshmi, J. Preparation and characterization of chitosan binary blend. *Int. J. Sci. Res. Publ.* **2012**, *2*, 1–9.
12. Xu, K.; Li, K.; Zhong, T.; Guan, L.; Xie, C.; Li, S. Effects of chitosan as biopolymer coupling agent on the thermal and rheological properties of polyvinyl chloride/wood flour composites. *Compos. Part B Eng.* **2014**, *58*, 392–399. [CrossRef]
13. Cai, X.; Tong, H.; Shen, X.; Chen, W.; Yan, J.; Hu, J. Preparation and characterization of homogeneous chitosan-polylactic acid/hydroxyapatite nanocomposite for bone tissue engineering and evaluation of its mechanical properties. *Acta Biomater.* **2009**, *5*, 2693–2703. [CrossRef] [PubMed]
14. Min, D.H.; Kim, M.J.; Yun, J.H.; Kim, C.S.; Lee, Y.K.; Choi, S.H.; Kim, K.N.; Kim, C.K. Effect of calcium phosphate glass scaffold with chitosan membrane on the healing of alveolar bone in 1 wall intrabony defect in the beagle dogs. *Key Eng. Mater.* **2005**, *284–286*, 851–854. [CrossRef]
15. Cooper, A.; Bhattarai, N.; Zhang, M. Fabrication and cellular compatibility of aligned chitosan—PCL fibers for nerve tissue regeneration. *Carbohydr. Polym.* **2011**, *85*, 149–156. [CrossRef]
16. Zhang, Y.; Zhang, M. Microstructural and mechanical characterization of chitosan scaffolds reinforced by calcium phosphates. *J. Non-Cryst. Solids* **2001**, *282*, 159–164. [CrossRef]
17. Felfel, R.M.; Ahmed, I.; Parsons, A.J.; Harper, L.T.; Rudd, C.D. Initial mechanical properties of phosphate-glass fibre-reinforced rods for use as resorbable intramedullary nails. *J. Mater. Sci.* **2012**, *47*, 4884–4894. [CrossRef]
18. Pacaphol, K.; Aht-Ong, D. The influences of silanes on interfacial adhesion and surface properties of nanocellulose film coating on glass and aluminum substrates. *Surf. Coat. Technol.* **2017**, *320*, 70–81. [CrossRef]
19. Gunanathan, C.; Ben-David, Y.; Milstein, D. Direct synthesis of amides from alcohols and amines with liberation of H_2. *Science* **2007**, *317*, 790–792. [CrossRef]
20. El-Hefian, E.A.; Nasef, M.M.; Yahaya, A.H. The preparation and characterization of chitosan/poly (vinyl alcohol) blended films. *J. Chem.* **2010**, *7*, 1212–1219. [CrossRef]
21. Tan, C.; Ahmed, I.; Parsons, A.J.; Sharmin, N.; Zhu, C.; Liu, J.; Rudd, C.D.; Liu, X. Structural, thermal and dissolution properties of MgO- and CaO-containing borophosphate glasses: Effect of Fe_2O_3 addition. *J. Mater. Sci.* **2017**, *52*, 7489–7502. [CrossRef]
22. Tan, C.; Ahmed, I.; Parsons, A.J.; Zhu, C.; Betanzos, F.B.; Rudd, C.D.; Liu, X. Effects of Fe_2O_3 addition and annealing on the mechanical and dissolution properties of MgO- and CaO-containing phosphate glass fibres for bio-applications. *Biomed. Glasses* **2018**, *4*, 57–71. [CrossRef]

23. Jin, R.M.; Sultana, N.; Baba, S.; Hamdan, S.; Ismail, A.F. Porous PCL/chitosan and nHA/PCL/chitosan scaffolds for tissue engineering applications: Fabrication and evaluation. *J. Nanomater.* **2015**, *2015*, 1–8. [CrossRef]
24. Ahmed, I.; Parsons, A.J.; Palmer, G.; Knowles, J.C.; Walker, G.S.; Rudd, C.D. Weight loss, ion release and initial mechanical properties of a binary calcium phosphate glass fibre/PCL composite. *Acta Biomater.* **2008**, *4*, 1307–1314. [CrossRef] [PubMed]
25. Haque, P.; Parsons, A.J.; Barker, I.A.; Ahmed, I.; Irvine, D.J.; Walker, G.S.; Rudd, C.D. Interfacial properties of phosphate glass fibres/PLA composites: Effect of the end functionalities of oligomeric PLA coupling agents. *Compos. Sci. Technol.* **2010**, *70*, 1854–1860. [CrossRef]
26. Sharmin, N.; Rudd, C.D.; Parsons, A.J.; Ahmed, I. Structure, viscosity and fibre drawing properties of phosphate-based glasses: Effect of boron and iron oxide addition. *J. Mater. Sci.* **2016**, *51*, 7523–7535. [CrossRef]
27. Zawadzki, J.; Kaczmarek, H. Thermal treatment of chitosan in various conditions. *Carbohydr. Polym.* **2010**, *80*, 394–400. [CrossRef]
28. Lu, M.; Wang, F.; Liao, Q.; Chen, K.; Qin, J.; Pan, S. FTIR spectra and thermal properties of TiO_2-doped iron phosphate glasses. *J. Mol. Struct.* **2015**, *1081*, 187–192. [CrossRef]
29. Qian, B.; Yang, S.; Liang, X.; Lai, Y.; Gao, L.; Yin, G. Structural and thermal properties of La_2O_3-Fe_2O_3-P_2O_5 glasses. *J. Mol. Struct.* **2012**, *1011*, 153–157. [CrossRef]
30. Ciceo-Lucacel, R.; Radu, T.; Ponta, O.; Simon, V. Novel selenium containing boro-phosphate glasses: Preparation and structural study. *Mater. Sci. Eng. C Mater. Biol. Appl.* **2014**, *39*, 61–66. [CrossRef]
31. Sharmin, N.; Hasan, M.S.; Rudd, C.D.; Boyd, D.; Werner-Zwanziger, U.; Ahmed, I.; Parsons, A.J. Effect of boron oxide addition on the viscosity-temperature behaviour and structure of phosphate-based glasses. *J. Biomed. Mater. Res. B* **2016**, *105*, 754–777. [CrossRef] [PubMed]
32. Kweon, H.; Um, I.C.; Park, Y.H. Structural and thermal characteristics of Antheraea pernyi silk fibroin/chitosan blend film. *Polymer* **2001**, *42*, 6651–6656. [CrossRef]
33. Pawlak, A.; Mucha, M. Thermogravimetric and FTIR studies of chitosan blends. *Thermochim. Acta* **2003**, *396*, 153–166. [CrossRef]
34. Zheng, H.; Du, Y.; Yu, J.; Huang, R.; Zhang, L. Preparation and Characterization of Chitosan/Poly(vinyl alcohol) Blend Fibers. *J. Appl. Polym. Sci.* **2001**, *80*, 2558–2565. [CrossRef]
35. Mohammadi, Z.; Mesgar, A.S.; Rasouli-Disfani, F. Reinforcement of freeze-dried chitosan scaffolds with multiphasic calcium phosphate short fibers. *J. Mech. Behav. Biomed. Mater.* **2016**, *61*, 590–599. [CrossRef] [PubMed]
36. Lai, Y.M.; Liang, X.F.; Yang, S.Y.; Wang, J.X.; Cao, L.H.; Dai, B. Raman and FTIR spectra of iron phosphate glasses containing cerium. *J. Mol. Struct.* **2011**, *992*, 84–88. [CrossRef]
37. Saranti, A.; Koutselas, I.; Karakassides, M.A. Bioactive glasses in the system CaO-B_2O_3-P_2O_5: Preparation, structural study and in vitro evaluation. *J. Non-Cryst. Solids* **2006**, *352*, 390–398. [CrossRef]
38. Ma, L.; Brow, R.K.; Choudhury, A. Structural study of Na_2O-FeO-Fe_2O_3-P_2O_5 glasses by Raman and Mössbauer spectroscopy. *J. Non-Cryst. Solids* **2014**, *402*, 64–73. [CrossRef]
39. Joseph, K.; Premila, M.; Amarendra, G.; Kutty, K.V.G.; Sundar, C.S.; Rao, P.R.V. Structure of cesium loaded iron phosphate glasses: An infrared and Raman spectroscopy study. *J. Nucl. Mater.* **2012**, *420*, 49–53. [CrossRef]
40. Mikhailov, G.P.; Tuchkov, S.V.; Lazarev, V.V.; Kulish, E.I. Complexation of chitosan with acetic acid according to Fourier transform Raman spectroscopy data. *Russ. J. Phys. Chem. A* **2014**, *88*, 936–941. [CrossRef]
41. Ren, X.D.; Liu, Q.S.; Feng, H.; Yin, X.Y. The Characterization of Chitosan Nanoparticles by Raman Spectroscopy. *Appl. Mech. Mater.* **2014**, *665*, 367–370. [CrossRef]
42. Reinas, A.E.; Hoscheid, J.; Outuki, P.M.; Cardoso, M.L.C. Preparation and characterization of microcapsules of Pterodon pubescens Benth. by using natural polymers. *Braz. J. Pharm. Sci.* **2014**, *50*, 919–930. [CrossRef]
43. Retamal, M.J.; Cisternas, M.A.; Gutierrez-Maldonado, S.E.; Perez-Acle, T.; Seifert, B.; Busch, M.; Huber, P.; Volkmann, U.G. Towards bio-silicon interfaces: Formation of an ultra-thin self-hydrated artificial membrane composed of dipalmitoylphosphatidylcholine (DPPC) and chitosan deposited in high vacuum from the gas-phase. *J. Chem. Phys.* **2014**, *141*, 104201. [CrossRef] [PubMed]
44. Zajac, A.; Hanuza, J.; Wandas, M.; Dyminska, L. Determination of N-acetylation degree in chitosan using Raman spectroscopy. *Spectrochim. Acta A Mol. Biomol. Spectrosc.* **2015**, *134*, 114–120. [CrossRef] [PubMed]

45. Orrego, C.E.; Salgado, N.; Valencia, J.S.; Giraldo, G.I.; Giraldo, O.H.; Cardona, C.A. Novel chitosan membranes as support for lipases immobilization: Characterization aspects. *Carbohydr. Polym.* **2010**, *79*, 9–16. [CrossRef]
46. Bunker, B.C.; Casey, W.H. *The Aqueous Chemistry of Oxides*; Oxford University Press: Oxford, UK, 2016.
47. Gao, S.-L.; Zhang, J.; Liu, J.-W.; Zhuang, R.-C.; Plonka, R.; Mäder, E. Healing Microcracks and Early Warning Composite Fractures. In Proceedings of the 6th Colloquium on Textile Reinforced Structures (CTRS6), Berlin, Germany, 19–20 September 2011.
48. Perrin, C.L. The Logic behind a Physical-Organic Chemist's Research Topics. *J. Org. Chem.* **2017**, *82*, 819–838. [CrossRef]
49. Kohl, J.G.; Malicky, D.M.; Jones, A.M. Adhesion of epoxy (pseudobarnacles) to glass that has been treated with hydrophobic carbosilane-based coatings. *Prog. Org. Coat.* **2017**, *107*, 1–4. [CrossRef]
50. Shah, B.L.; Matuana, L.M.; Heiden, P.A. Novel coupling agents for PVC/wood-flour composites. *J. Vinyl Addit. Technol* **2005**, *11*, 160–165. [CrossRef]
51. Huang, C.L.; Chen, Y.B.; Lo, Y.L.; Lin, Y.H. Development of chitosan/beta-glycerophosphate/glycerol hydrogel as a thermosensitive coupling agent. *Carbohydr. Polym.* **2016**, *147*, 409–414. [CrossRef]
52. Chenite, A.; Chaput, C.; Wang, D.; Combes, C.; Buschmann, M.D.; Hoemann, C.D.; Leroux, J.C.; Atkinson, B.L.; Binette, F.; Selmani, A. Novel injectable neutral solutions of chitosan form biodegradable gels in situ. *Biomaterials* **2000**, *21*, 2155–2161. [CrossRef]
53. Amaral, I.F.; Granja, P.L.; Barbosa, M.A. Chemical modification of chitosan by phosphorylation: An XPS, FT-IR and SEM study. *J. Biomater. Sci. Polym. Ed.* **2005**, *16*, 1575–1593. [CrossRef] [PubMed]
54. Hasan, M.S.; Ahmed, I.; Parsons, A.J.; Rudd, C.D.; Walker, G.S.; Scotchford, C.A. Investigating the use of coupling agents to improve the interfacial properties between a resorbable phosphate glass and polylactic acid matrix. *J. Biomater. Appl.* **2013**, *28*, 354–366. [CrossRef] [PubMed]
55. Bhattarai, N.; Li, Z.; Gunn, J.; Leung, M.; Cooper, A.; Edmondson, D.; Veiseh, O.; Chen, M.; Zhang, Y.; Ellenbogen, R.G.; et al. Natural-synthetic polyblend nanofibers for biomedical applications. *Adv. Mater.* **2009**, *21*, 2792–2797. [CrossRef]
56. Berger, J.; Reist, M.; Mayer, J.M.; Felt, O.; Peppas, N.A.; Gurny, R. Structure and interactions in covalently and ionically crosslinked chitosan hydrogels for biomedical applications. *Eur. J. Pharm. Biopharm.* **2004**, *57*, 19–34. [CrossRef]
57. Tanigawa, J.; Miyoshi, N.; Sakurai, K. Characterization of chitosan/citrate and chitosan/acetate films and applications for wound healing. *J. Appl. Polym. Sci.* **2008**, *110*, 608–615. [CrossRef]
58. Lawrie, G.; Keen, I.; Drew, B.; Chandler-Temple, A.; Rintoul, L.; Fredericks, P.; Grøndahl, L. Interactions between Alginate and Chitosan Biopolymers Characterized Using FTIR and XPS. *Biomacromolecules* **2007**, *8*, 2533–2541. [CrossRef] [PubMed]
59. Bhumkar, D.R.; Pokharkar, V.B. Studies on Effect of pH on Cross-linking of Chitosan with Sodium Tripolyphosphate: A Technical Note. *AAPS PharmSciTech* **2006**, *7*, E138–E143. [CrossRef]
60. Sayyar, S.; Murray, E.; Thompson, B.C.; Chung, J.; Officer, D.L.; Gambhir, S.; Spinks, G.M.; Wallace, G.G. Processable conducting graphene/chitosan hydrogels for tissue engineering. *J. Mater. Chem. B* **2015**, *3*, 481–490. [CrossRef]
61. Yap, W.F.; Yunus, W.M.M.; Talib, Z.A.; Yusof, N.A. X-ray photoelectron spectroscopy and atomic force microscopy studies on crosslinked chitosan thin film. *Int. J. Phys. Sci.* **2011**, *6*, 2744–2749.
62. Nikolenko, Y.M.; Kuryavyi, V.G.; Sheveleva, I.V.; Zemskova, L.A.; Sergienko, V.I. Atomic force microscopy and X-ray photoelectron spectroscopy study of chitosan-carbon fiber materials. *Inorg. Mater.* **2010**, *46*, 221–225. [CrossRef]
63. Majjane, A.; Chahine, A.; Et-tabirou, M.; Echchahed, B.; Do, T.-O.; Breen, P.M. X-ray photoelectron spectroscopy (XPS) and FTIR studies of vanadium barium phosphate glasses. *Mater. Chem. Phys.* **2014**, *143*, 779–787. [CrossRef]

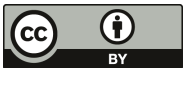

fibers

MDPI

Article

Further Progress in Functional Interlayers with Controlled Mechanical Properties Designed for Glass Fiber/Polyester Composites

Antonin Knob [1], Jaroslav Lukes [2], Lawrence Thadeus Drzal [3] and Vladimir Cech [4,*]

[1] Remarkplast s.r.o., Luka 152, CZ-783 24 Luka, Czech Republic; knob@remarkplast.cz
[2] Department of Mechanics, Biomechanics and Mechatronics, Czech Technical University in Prague, Technicka 4, CZ-166 07 Prague 6, Czech Republic; jaroslav.lukes@bruker.com
[3] Composite Materials and Structures Center, Michigan State University, 2100 Engineering Building, East Lansing 48824, MI, USA; drzal@egr.msu.edu
[4] Institute of Materials Chemistry, Faculty of Chemistry, Brno University of Technology, Purkynova 118, CZ-612 00 Brno, Czech Republic
* Correspondence: cech@fch.vut.cz; Tel.: +420-541149304

Received: 19 July 2018; Accepted: 14 August 2018; Published: 16 August 2018

Abstract: Compatible interlayers must be coated on reinforcing fibers to ensure effective stress transfer from the polymer matrix to the fiber in high-performance polymer composites. The mechanical properties of the interlayer, and its interfacial adhesion on both interfaces with the fiber and polymer matrix are among the key parameters that control the performance of polymer composite through the interphase region. Plasma-synthesized interlayers, in the form of variable materials from polymer-like to glass-like films with a Young's modulus of 10–52 GPa, were deposited on unsized glass fibers used as reinforcements in glass fiber/polyester composites. Modulus Mapping (dynamic nanoindentation testing) was successfully used to examine the mechanical properties across the interphase region on cross-sections of the model composite in order to distinguish the fiber, the interlayer, and the modified and bulk polymer matrix. The interfacial shear strength for plasma-coated fibers in glass fiber/polyester composites, determined from the microindentation test, was up to 36% higher than those of commercially sized fibers. The effects of fiber pretreatment, single and double interlayers, and post-treatment of the interlayer on interfacial shear strength were also discussed. Functional interlayers with high shear yield strength and controlled physicochemical properties are promising for high-performance polymer composites with a controlled interphase.

Keywords: glass fiber; polymer-matrix composites; interface/interphase; nanoindentation; mechanical properties; microindentation test

1. Introduction

Fiber-reinforced polymer composites are significant materials for transportation, building/construction, electrical/electronic applications, and consumer goods mainly because of their low density and high specific strength. The performance of the polymer composite is controlled by the properties of the fiber reinforcement, the polymer matrix, and the interphase [1], which is the region of material between the fiber and the polymer matrix responsible for the effective stress transfer from the matrix to the fiber. The composite interphase comprises a functional interlayer, and eventually, a modified matrix region. The functional interlayer is a material in the form of thin film that is deposited on the fiber surface to improve compatibility and create a strong but tenacious link between both components. The modified matrix is the part of the polymer matrix affected by the presence of the coated fiber. It is the interphase that is very important for the resultant performance of

the composite material. Even reinforcing fibers with high modulus or high strength and polymers with high thermal or chemical resistance result in inefficient composites in the case of a poor interphase. The interphase is built in polymer composites using functional interlayers through fiber sizing, coating, or grafting in a wet chemical process or through chemical vapor deposition [2].

Investigating interphase properties is very important for understanding its functionality and the possibility of its optimization for a specific composite system, i.e., the fiber and the polymer matrix. The reinforcement and the polymer matrix are mostly very different materials in terms of their mechanical, electrical, and chemical properties. The interphase can, therefore, be identified between the two composite phases based on differences in material structure, Young's modulus, hardness, coefficient of friction, dielectric permittivity, elemental composition, or chemical structure. The cross-section of the polymer composite was investigated using microscopic infrared spectroscopy [3]; however, the interphase region is tiny since the interphase thickness is generally less than several microns, and nanoscale imaging techniques are necessary to ensure sufficient lateral resolution. Transmission electron microscopy (TEM) has sufficient lateral resolution to distinguish the interphase region based on differences in the atomic mass of the elements, and even the element composition profile across the composite phases can be determined using electron energy loss spectroscopy (EELS) [4,5]. The results show some limitations depending on the technique used to fabricate a sample for TEM imaging, such as focus ion beam (FIB), ion beam etching, and ultramicrotomy [6].

Another principal technique suitable for interphase characterization is atomic force microscopy (AFM), which is used in different modes. Standard AFM tips with a radius of less than 10 nm provide sufficient lateral resolution. Electrostatic force microscopy (EFM) is one of the modes used to measure electrostatic interactions between the AFM tip and the composite phases made from dielectric materials. The interaction is sensitive to charge distribution or local differences in dielectric permittivity of composite phases [7]. During scanning in phase-imaging AFM mode, the oscillating tip is influenced by contact with composite components of different viscoelastic properties, resulting in a phase shift of the tip against the applied oscillating force. The interphase area can be identified due to changes in phase distribution over the sample surface [8,9]. Similarly, lateral force microscopy using AFM contact mode can be used to characterize the distribution of lateral forces on the sample surface to distinguish the interphase area due to a different coefficient of friction [9]. In this mode, the constant force-feedback on the sample adjusts the height of the AFM cantilever to compensate for the topographic features of the surface, and the torsion of the cantilever bearing the tip characterizes lateral forces as a result of surface friction. In the intermodulation AFM, the cantilever is simultaneously excited by two frequencies near the resonance, and the cantilever response at a new frequency contains information on the surface mechanical properties of the composite sample [10]. Atomic force acoustic microscopy (AFAM) is a combination of ultrasonics with AFM, where the composite sample is excited with ultrasonic frequency by means of a piezoelectric transducer that causes vibrations of the sample surface, and the vibration behavior of the AFM cantilever in contact with the surface of the sample is sensitive to its local elastic properties [9,11]. All of the aforementioned AFM modes have some limitations in order to sufficiently differentiate the interphase region.

The difference between the mechanical properties of composite constituents is sufficient to potentially distinguish the interphase region. Nanoindentation techniques [12,13] are, therefore, ideal for characterizing the distribution of mechanical properties across the fiber/matrix interface in terms of Young's modulus and hardness. Quantitative nanomechanical measurements are possible, starting with forces $\leq$1 μN, but the lateral resolution is not as high as in AFM measurements due to a higher radius of commercially available diamond indenters with a radius of 50 nm (Berkovich) or 40 nm (cube corner). However, nanoindentation together with nanoscratch measurements is influenced by fiber constraint [8], because the indenter induces stress near the fiber surface, and the critical distance is approximately twenty times the indentation depth [14,15]. Dynamic nanoindentation may be operated as a Modulus Mapping mode that appears to be more suitable for observing the cross-section of the

composite sample using detailed maps of the complex modulus, the storage, and the loss modulus, just a few nanometers below the sample surface, thereby avoiding the fiber constraint [9,16]. This technique is carried out by superimposing a small sinusoidal force on a greater but constant force during the indentation test.

Recently, force mapping spectroscopy (nanomechanical mapping) [17–21] was applied in order to characterize the interphase region in polymer composites and nanocomposites. In this AFM mode, a force–distance curve is recorded in each pixel of the map, and a linear portion of this curve corresponding to an elastic regime is used to determine the Young's modulus using the Derjaguin–Muller–Toporov (DMT) model. However, the determined values of Young's modulus are not realistic for the range of moduli from the polymer matrix to the reinforcement, and they are strongly affected by the surface topography of the composite sample. It was found that surface formations (grains), with a radius similar or larger than that of the AFM tip or diamond indenter, have a critical influence on probe (AFM or nanoindentation) measurements used to characterize mechanical properties based on the geometry of contact between the tip and the sample [22].

Plasma-enhanced chemical vapor deposition (PECVD) is a technique for depositing thin films with controlled mechanical properties [23], which are intended to be used as functional interlayers for glass fiber/polyester composites in order to improve their interfacial shear strength (IFSS). This study is focused on examining the mechanical properties of such interlayers in model composites using Modulus Mapping based on our previous experience [9]. Selected interlayers with controlled mechanical and chemical properties were tested to determine how they affect the IFSS in glass fiber/polyester composites determined by the microindentation test [24]. Also, the effects of pretreatment, plasma coating (thin-film deposition), and post-treatment of glass fibers (GF) on determined IFSS were firstly discussed.

2. Materials and Methods

2.1. Thin-Film Deposition

A plasma reactor [25] equipped with a radio-frequency (RF; 13.56 MHz) capacitive coupling system using asymmetric plan-parallel plate electrodes was employed to deposit thin films on silicon wafers (polished on both sides (1 0 0) with an overlayer of native SiO_2 (3 nm), infrared (IR), transparent, $0.8 \times 10 \times 10$ mm^3; ON Semiconductor, Roznov pod Radhostem, Czech Republic) and single GFs (unsized (bare) E-glass, 1200 tex, mean diameter 19 µm; Saint-Gobain Adfors, Litomysl Czech Republic). Fifteen GFs separated from the GF bundle were placed parallel to each other on silicon wafers and fixed with adhesive carbon tape suitable for vacuum applications. Hydrogenated amorphous carbon-silicon (a-CSi:H) films were deposited from pure tetravinylsilane (TVS; Si–$(CH{=}CH_2)_4$ purity 97%, Sigma Aldrich, Prague, Czech Republic) precursor, and hydrogenated amorphous carbon-silicon oxide (a-CSiO:H) films were deposited from TVS in a mixture with oxygen gas (TVS/O_2 mixture) using PECVD. Firstly, the silicon wafer (alone or with single GFs) was loaded into the RF bottom electrode, and the plasma reactor was evacuated to a basic pressure of 1×10^{-5} Pa. Then, the silicon wafer was pretreated with argon (Ar) plasma (10.0 sccm, 5.7 Pa, continuous wave 5.0 W) for 10 min to remove adsorbed gases and to ensure the reproducible adhesion of deposited films. The a-CSi:H or a-CSiO:H films were deposited using pulsed plasma at a mass flow rate of 3.8 sccm, a pressure of 2.7 Pa, and an effective power of 2.0–10 W. The effective power, W_{eff}, was set by changing the ratio of the time the plasma is switched on, t_{on}, to the period, T, defined as $T = t_{on} + t_{off}$, and thus, $W_{eff} = t_{on}/T \times W_{total}$, where t_{off} is the time the plasma is switched off and W_{total} is the total RF power. An oxygen fraction of 0.92 was used for the TVS/O_2 mixture as the mass flow rates for TVS and O_2 gas were 0.30 sccm and 3.5 sccm, respectively. A movable shutter was used to deposit the films in steady-state plasma conditions monitored by mass spectrometry (Process Gas Analyser HPR-30, Hiden Analytical, Warrington, UK). When the deposition process was completed, the plasma reactor was flushed with Ar gas (10.0 sccm, 5.7 Pa) to remove residual gases for 60 min, and the reactor was

then evacuated to a basic pressure of 1×10^{-5} Pa. The deposited sample was moved to the load-lock chamber after 12 h, and the chamber was then flooded with air to atmospheric pressure [25].

Another plasma reactor [26], an RF helical coupling system operated in a pulsed regime, was used to deposit (PECVD) thin films on special glass slides without flaws ($1.0 \times 26 \times 76$ mm^3; Knittel Glaser, Braunschweig, Germany), silicon wafers, and GF bundles specified above. This cylindrical discharge is axially symmetrical, and therefore, more suitable for film deposition on the GF bundle mounted in the discharge axis. This plasma reactor was first evacuated to a basic pressure of 5×10^{-4} Pa. The planar substrate or GF bundle was pretreated with O_2 plasma (5.0 sccm, 4.0 Pa, 25 W) for 60 min to desorb gases and remove hydrocarbons from the substrate surface (planar or fibrous). The oxygen fraction $X = O_2/(TVS + O_2)$ in the gas mixture was varied from 0–0.46 (0, 0.10, 0.21, 0.33, and 0.46) at a total flow rate ($TVS + O_2$) of 0.80 sccm, and the corresponding pressure was 1.4 Pa. To deposit all films, an effective power of 5.0 W (time-on pulse, period, and total power were 1 ms, 10 ms, and 50 W, respectively) was used. Finally, after film deposition, the apparatus was flushed with Ar gas (10.0 sccm, 10 Pa). After 60 min, the reactor was evacuated to a basic pressure, and, after 12 h, was flooded with air at atmospheric pressure.

2.2. Thin-Film Analysis

The thickness of the films deposited on the silicon wafers was determined using a phase-modulated spectroscopic ellipsometer, UVISEL (HORIBA Scientific, Longjumeau, France), at a wavelength of 250–830 nm in a 2-nm step; the angle of incidence was 70° and the spot size was 100×300 μm^2. The average deposition rate was given by the ratio of film thickness to deposition time. The thickness of the film deposited on planar or fibrous substrate was controlled by the deposition time at a constant deposition rate.

Infrared measurements in the 500–4000 cm^{-1} wavenumber range were made using a VERTEX 80 vacuum Fourier-transform infrared (FTIR) spectrometer (Bruker Optics, Billerica, MA, USA). Transmission spectra were obtained on films deposited on infrared-transparent silicon wafers. To remove the spectral properties of the silicon wafer, an absorption-subtraction technique was used, and background correction was carried out before each measurement. The spectral resolution was 4 cm^{-1}, and 256 scans were recorded in order to achieve a reasonable signal-to-noise ratio. The bulk chemical composition of the thin films was investigated using conventional and resonant Rutherford backscattering spectrometry (RBS) and elastic recoil detection analysis (ERDA) methods on a Tandetron 4130MC accelerator (High Voltage Engineering Europa B.V., Amersfoort, The Netherlands (HVEE)) using 2.73-MeV alpha particles.

The Young's modulus of the films deposited on the silicon wafers was determined with the Oliver–Pharr method [27] from nanoindentation measurements using a two-dimensional (2D) TriboScope (Hysitron, Eden Prairie, MN, USA) attached to an NTegra Prima Scanning Probe Microscope (NT-MDT), Zelenograd, Russia. A Berkovich tip with a radius of curvature of 50 nm was used. The experiment was performed in cyclic mode to obtain the depth profile of Young's modulus to 15–20% of the film thickness, applying 19 loading and partial unloading cycles in a single indentation, while the unloading fraction was kept constant at 0.8, and the loading was increased using a displacement exponent of 2 (exponential function) [28]. The experimental depth profile was extrapolated to the zero-contact depth (film surface) to estimate the correct Young's modulus of the film not influenced by the substrate properties [29].

2.3. Sample Preparation and Modulus Mapping

After thin-film deposition, 15 GFs fixed with adhesive carbon tape were transferred from the silicon wafer into a silicon rubber mold, which was filled with unsaturated polyester resin (isophthalic) Viapal HP 349 F (Sirca S. p. A., Sandono di Massanzago, Italy), and cured at 140 °C to form a polymer block, $5 \times 13 \times 25$ mm^3 with unidirectional fibers. This block was inserted into the metallographic

sample holder with GFs placed normally to the sample surface, and the surface was polished using conventional metallographic techniques.

The mechanical properties of the interphase region around a single GF in the polyester matrix were characterized using a Hysitron TI 950 TriboIndenter nanomechanical test instrument (Hysitron, Eden Prairie, MN, USA) with a nanoDMA III (Dynamic Mechanical Analysis) package. The Modulus Mapping mode combines the in situ scanning probe microscopy (SPM) imaging capability of Hysitron's nanomechanical testing instruments with the ability to perform nanoDMA III tests. During the test, the indenter is scanned over the surface to image the topography of the sample. During scanning, the probe is oscillated with the specified frequency and amplitude of the load. The resulting signal from the transducer is then analyzed to determine the displacement amplitude and phase delay of the oscillation at each pixel in the image [9]. The software plots these measurements in separate image files, and after scanning is complete, the images can be analyzed to determine the storage, E', and loss, E'', modulus at each point using the following equations:

$$E' = \frac{k_s\sqrt{\pi}}{2\sqrt{A}}, \quad E'' = \frac{\omega C_s\sqrt{\pi}}{2\sqrt{A}} \tag{1}$$

where k_s and C_s are the stiffness and damping of the specimen determined from the displacement amplitude and phase difference between the force and the displacement, A is the projected contact area, and ω is the frequency used [27,30]. A cube diamond indenter (NorthStar, Hysitron, Eden Prairie, MN, USA) with a radius of curvature of 40 nm was used for Modulus Mapping. The amplitude of a dynamic force of 5 μN at an oscillation frequency of 220 Hz was superimposed to a normal contact force of 15 μN in order to maintain the dynamic displacement amplitude at 4 nm when scanning the sample surface in an in situ SPM mode. The radius of the tip was carefully calibrated using Modulus Mapping in standard silica at the above conditions, and with the same displacement as in the test specimen. The map resolution in the 3 × 3 μm^2 scan area was 256 × 256 pixels.

2.4. Composite Fabrication and Microindentation Test

After the GF bundle was surface-modified in an RF helical coupling system, the bundle was impregnated with unsaturated polyester resin and then axially placed in a silicon rubber mold that was filled with resin, before being cured at 140 °C to form a polymer disc of 14 mm in diameter and 5 mm in height [31]. Similar to the resin block with unidirectional fibers, the disc was embedded in a metallographic specimen and polished using conventional metallographic techniques.

The polished cross-section of the composite, with the fibers normal to the surface of the sample 3 mm high, was used to characterize the interfacial adhesion of GF in the polyester matrix using the microindentation test [24]. Using an Interfacial Testing System (ITS) (Dow Chemical Company, Midland, MI, USA) [32], a diamond tip with a diameter of 12 μm was applied to push the single fiber from its surrounding polyester resin. The tested fiber was indented at increased normal loading until failure of adhesion. The de-bonding of the fiber is visible as a dark shadow around the fiber. When the shadow appears around the fiber at an angle of between 90° and 120°, the fiber is considered to be de-bonded [32]. The IFSS was determined from the de-bond load, P, using a generalized empirical equation,

$$IFSS = A\frac{P}{D^2}\left[B\left(\frac{G_m}{E_f}\right)^{\frac{1}{2}} - C\log\left(\frac{d}{D}\right) - E\right] \tag{2}$$

where D is the fiber diameter, G_m and E_f are the matrix shear modulus and fiber axial modulus, respectively, d is the matrix thickness between the tested fiber and its nearest neighbor, and A = 1.249 × 10^4, B = 0.8757, C = 0.01863, and E = 0.02,650. A matrix shear modulus of 1.5 GPa and a fiber axial modulus of 73 GPa correspond to the polyester resin used and the GF, respectively [32].

3. Results

3.1. Mapping of Storage Modulus across the Interphase Region

Two polymer blocks, 5 × 13 × 25 mm^3, each with 15 unidirectional fibers (mean diameter 19 µm) embedded in polyester resin, were fabricated using unsized and commercially sized GFs to examine the interphase region with Modulus Mapping. The commercial sizing based on silane coupling agents was designated by the GF manufacturer for GF/polyester composites. After polishing, the metallographic specimen with GFs placed normally to the surface was scanned in a 3 × 3 µm^2 area using a cube corner indenter with a radius of 40 nm. The storage modulus across the fiber/polymer interface for the unsized GF is shown in Figure 1a. A three-dimensional (3D) image with a storage modulus in a color scale, which is used for better orientation, shows the black area corresponding to the polymer matrix and a part of the fiber with a sharply raised modulus at the fiber/polymer interface. The 2D projection of the storage modulus is visible at the top of Figure 1a. A similar image of the storage modulus was obtained for the commercially sized GF (Figure 1b). The detailed profile of the storage modulus close to the fiber/polymer interface (Figure 1c) enabled the finding of characteristic differences. The red line for the unsized GF rises in the immediate vicinity of the fiber surface, and the 0.07-µm-thick area on which the modulus was changed corresponds to the fiber constraint area rather than the interphase region. However, the blue line corresponding to the commercially sized GF indicates the wider area of the modulus change that can be assigned to the interphase region with a thickness of 0.5 µm. The interphase region around the commercially sized GF was non-regular, and the thickness varied from 0.1 (GF without sizing) to 0.5 µm. The storage modulus for the polyester resin outside the interphase region was approximately 6 GPa, as shown in Figure 1c, which appears to be a little overvalued because a Young's modulus of 4 GPa was evaluated from the quasi-static tensile test of the polyester resin. An increased storage modulus was found in the subsurface layer up to a depth of 40 nm of metallographic specimen, probably due to resin polishing.

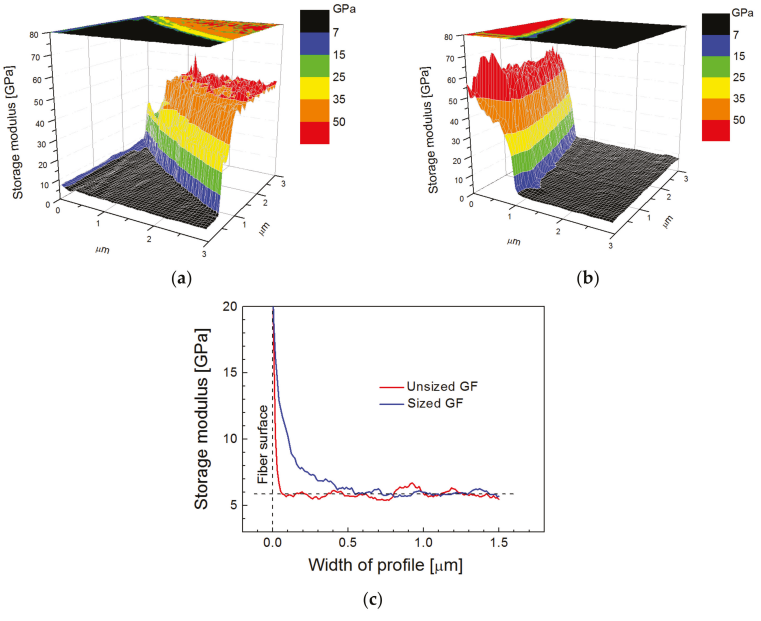

Figure 1. Storage modulus mapping of the interphase region in model glass fiber (GF)/polyester composites for (**a**) unsized GF, (**b**) sized GF, and (**c**) a detailed profile close to the fiber/polymer interface.

The polymer-like a-CSi:H film was deposited (68.7 nm/min) on single GFs and silicon wafers at an effective power of 2.0 W (time-on pulse, period, and total power were 1 ms, 5 ms, and 10 W, respectively) from a pure TVS precursor using the plasma reactor with plan-parallel electrodes. The film thickness was 895 nm, which was determined from the ellipsometric spectrum of the film on the silicon wafer, and we expect that approximately the same thickness of the film was deposited on the GFs. A Young's modulus of 10.0 ± 0.5 GPa was evaluated for the film on the silicon wafer using cyclic nanoindentation measurements. RBS/ERDA spectra of a-CSi:H film allowed determining the chemical composition and calculating the element ratios to the silicon concentration, resulting in a stoichiometric formula a-$C_{5.6}$Si:$H_{5.0}$. The high concentration of hydrogen (43 atom%) that is bonded to silicon and carbon atoms is responsible for the relatively low cross-linking of the mainly carbon network in the a-CSi:H film, resulting in the low Young's modulus that corresponds to a polymer-like material. GFs coated with this interlayer (a-$C_{5.6}$Si:$H_{5.0}$ film) were inserted in polyester resin to fabricate a model composite, whose cross-section was analyzed with Modulus Mapping to distinguish the interlayer between the fiber and the polymer matrix, and to characterize its mechanical properties. The storage modulus in a color scale across the interphase region in a model GF/polyester composite is shown in Figure 2a. The lateral resolution of this map is 11.7 nm. The scan area of 3 × 3 μm^2 shows the white area with a modulus above 62 GPa corresponding to GF surrounded by a ring with a modulus similar to the polymer matrix (black area on the left) with a blue contour. Profiles of the storage modulus (red line) and surface topography (blue line), corresponding to the GF with the polymer-like interlayer, are plotted in Figure 2b. Interpretation of mechanical properties is not easy due to the surface topography of the composite sample marked with a blue dashed line. Generally, the indentation measurement analysis is based on the assumption that the process is initiated by penetrating the indenter into a flat surface. The influence of surface roughness on nanoindentation measurements was interpreted using model simulations [22]. The polymer composite is a hybrid material, and its polished surface exhibits roughness in the interphase region due to the different mechanical properties of the composite phases. Based on the thickness of the interlayer, its position is expected at the GF surface, indicated by the yellow area in Figure 2b. At the interface between the interlayer and the polymer matrix, there is an elevated modulus, but it is an artefact due to the side contact of the indenter with the rough surface of the composite sample. In this case, the measured contact stiffness is higher than that corresponding to the flat surface, and the projected contact area is underestimated, resulting in an overestimated storage modulus. The slope of the surface across the interlayer provides a slightly underestimated modulus, corresponding to model simulations [22], but part of the interlayer close to the interlayer/fiber interface corresponds to the correct value of the storage modulus of 10 GPa. The surface roughness of the interphase region complicates the differentiation between the polymer-like interlayer and the polymer matrix with similar mechanical properties.

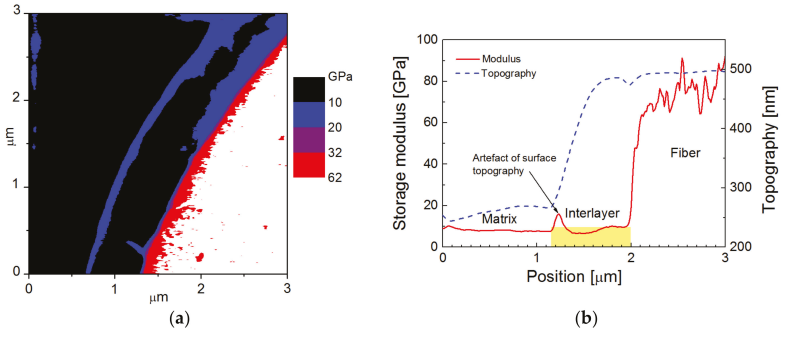

Figure 2. Modulus Mapping (scan area 3 × 3 μm^2) across the interphase region with a polymer-like (hydrogenated amorphous carbon-silicon (a-$C_{5.6}$Si:$H_{5.0}$)) interlayer in a model GF/polyester composite: (**a**) map of the storage modulus, (**b**) storage modulus and topography profiles.

An interlayer with a higher Young's modulus of 16.3 ± 0.8 GPa was deposited (9.7 nm/min) on single GFs at an effective power of 2.0 W (1 ms, 5 ms, and 10 W) from TVS in a mixture with oxygen gas with a 0.92 oxygen fraction. Oxygen atoms (34 atom%) were incorporated into the thin film, but carbon (29 atom%) and hydrogen (24 atom%) concentrations were reduced in the a-$C_{2.2}SiO_{2.6}$:$H_{1.8}$ film with a thickness of 966 nm, unlike the polymer-like a-$C_{5.6}$Si:$H_{5.0}$ film. Cross-linking of the carbon-silicon oxide network is still relatively low due to Si–H, Si–OH, C–H, C–OH, and C=O bonding species. The results of Modulus Mapping across the interphase region in a model GF/polyester composite with a-$C_{2.2}SiO_{2.6}$:$H_{1.8}$ interlayer are plotted in Figure 3. The map of the storage modulus in Figure 3a provides easy orientation in specific composite phases; the red/white area corresponds to a fiber, surrounded by a blue belt, indicating an interlayer with a higher modulus than the polymer matrix that is marked with a black area. The surface topography across the interlayer, marked by the yellow area, was flat, and was, therefore, favorable for determining the correct value of the storage modulus (Figure 3b). The storage modulus of the interlayer slightly increased from the interface between the interlayer and the polymer matrix to the interlayer/fiber interface, but the mean value was 16 GPa. A small portion of the interphase region with a thickness of 0.1–0.2 μm between the interlayer and the polymer matrix had a slightly elevated modulus, and could, therefore, correspond to the modified matrix.

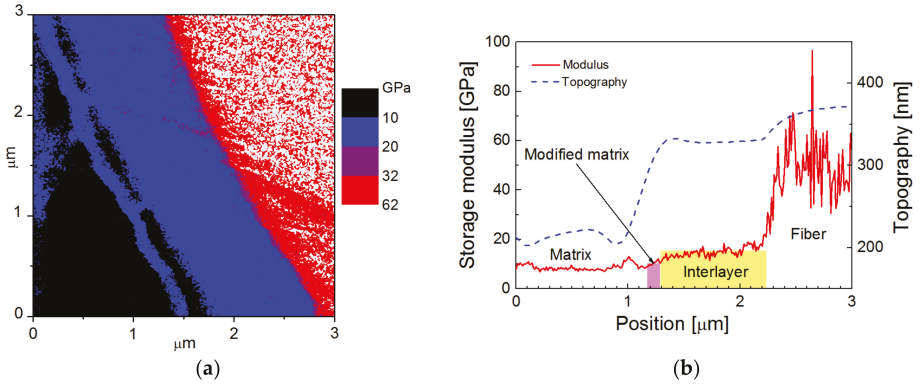

Figure 3. Modulus Mapping (scan area 3 × 3 μm^2) across the interphase region with the a-$C_{2.2}SiO_{2.6}$:$H_{1.8}$ interlayer in a model GF/polyester composite: (**a**) map of the storage modulus, (**b**) storage modulus and topography profiles.

Another interlayer in the form of a silicon oxide film with a carbon concentration of 16 atom% was deposited (7.5 nm/min) at 4.5 W (1 ms, 11 ms, and 50 W) from TVS in a mixture with oxygen gas with a 0.92 oxygen fraction. The a-$C_{0.7}SiO_{2.1}$:$H_{0.8}$ interlayer with a thickness of 1109 nm was more cross-linked, with a Young's modulus of 29.6 ± 1.5 GPa. Modulus Mapping in Figure 4a distinguished the fiber (white area) from the interlayer (purple area) and the polymer matrix (black area). A part of the blue belt with a thickness of 0.3 to 0.4 μm between the interlayer and the polymer matrix may represent a modified matrix region characterized by a gradually increasing modulus. The beginning of the step in the surface topography between the modified and the bulk matrix was responsible for the elevated modulus, which is an artefact caused by a specific surface topography, and can be seen as a purple contour in the blue belt (Figure 4b). In this case, the mechanical properties of the interlayer were sufficiently high to avoid any surface roughness between the fiber and the interlayer. This means that the surface topography was flat for the interlayer, delineated with the yellow area, and the storage modulus of the interlayer increased from 21 to 31 GPa at the interlayer/fiber interface at a mean value of 26 GPa.

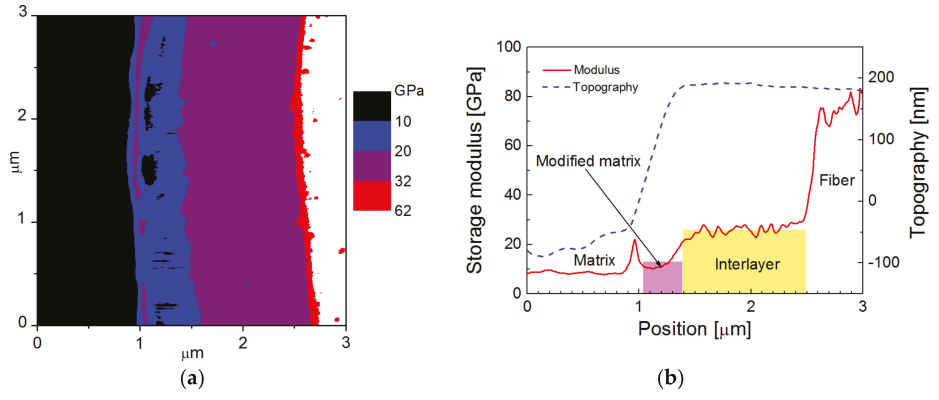

Figure 4. Modulus Mapping (scan area 3 × 3 µm^2) across the interphase region with a hydrogenated amorphous carbon-silicon oxide (a-$C_{0.7}SiO_{2.1}$:$H_{0.8}$) interlayer in a model GF/polyester composite: (**a**) map of storage modulus, (**b**) storage modulus and topography profiles.

An SiO_2-like interlayer with a small concentration of carbon (3 atom%) and hydrogen (11 atom%) was deposited (5.5 nm/min) at 10 W (1 ms, 5 ms, and 50 W) from TVS in a mixture with oxygen gas with a 0.92 oxygen fraction. The a-$C_{0.1}SiO_{1.9}$:$H_{0.4}$ interlayer with a thickness of 950 nm was highly cross-linked resulting in a Young's modulus of 51.7 ± 3.3 GPa. Figure 5a shows a map of the storage modulus corresponding to the fiber (white area), interlayer (red area), modified matrix (blue area), and the bulk matrix (black area). The same deposition time resulted in consistent film thickness for films deposited on planar and fibrous substrates. The thickness of the modified matrix was increased for the SiO_2-like interlayer, and varied from 0.5 to 0.7 µm. The mean value of the storage modulus for the flat surface of the interlayer was 52 GPa (Figure 5b), as expected from cyclic nanoindentation. The storage modulus across the interlayer varied like across the GF surface. This means that the interlayer material was as brittle as the glass, and the composite surface was specifically modified (slightly scratched) with 50-nm alumina nanoparticles, which were used to polish composite samples. The root-mean-square (RMS) roughness of the composite surface was 30 nm for a scan area of 100 × 100 µm^2 measured by AFM. The varying modulus was caused by surface topography. Nanoindentation measurements of the material with a higher modulus are more sensitive to surface roughness [22]. The wide region of the modified matrix with the elevated modulus between the interlayer and the bulk matrix is evident for the SiO_2-like interlayer in Figure 5b. We can assume that the modified matrix region was created as a result of a chemical bonding at the interface between the interlayer and the polymer matrix, unlike the unsized GF (Figure 1c). The polymer network was firmly anchored onto the surface of the interlayer, which increased the rigidity of the polymer network. The interlayer/polymer matrix interface was sharp, and no interpenetrating network between the interlayer and the polymer matrix can be expected, unlike commercially sized GFs that are surface-modified by silane coupling agents [33]. Analysis of the depth profile for the interlayers and GFs revealed that the subsurface layer, up to a depth of 5–10 nm, showed an increase in the storage modulus due to the mechanical modification of the material during the polishing procedure. Therefore, the storage modulus in the maps may be overestimated by up to 10% for the SiO_2-like interlayer and GFs, as the average displacement of the indenter was approximately 5 nm, but it cannot affect the polymer-like interlayer with an average displacement of 15 nm. The differences in storage modulus among the composite phases were significantly higher compared to the differences in loss modulus, and were, therefore, more appropriate for the distinction of the specific phase.

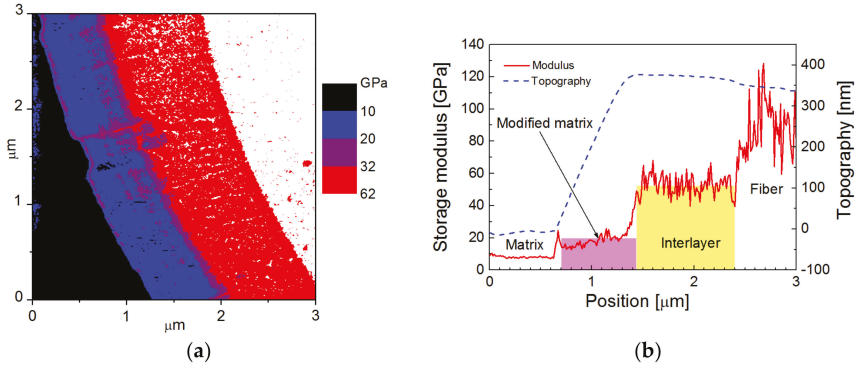

Figure 5. Modulus Mapping (scan area 3 × 3 µm^2) across the interphase region with the SiO_2-like (a-$C_{0.1}SiO_{1.9}$:$H_{0.4}$) interlayer in a model GF/polyester composite: (**a**) map of storage modulus, (**b**) storage modulus and topography profiles.

3.2. Selected Interlayers for GF/Polyester Composite

As shown in Section 3.1, a wide range of materials from polymer-like to SiO_2-like films with a Young's modulus of 10 to 52 GPa can be used as interlayers for GF/polyester composites. The chemical and physical compatibility of the interlayer and the polymer matrix was increased for the polymer-like interlayers with the lower (≤16 GPa) Young's modulus as the thickness of the modified matrix region was decreased. Model simulations (finite element analysis) enabled calculating the interfacial stress fields in a GF/polyester composite during the microindentation test. The simulation showed that inserting a suitable interlayer between the fiber and the polymer matrix resulted in a significant reduction in shear stress across the interphase region when the polymer composite was under mechanical or thermal loading. If the indenter pushed the individual fiber into the polyester resin during the microindentation test, the interfacial shear stress at the interlayer/fiber interface increased with the raised Young's modulus of the interlayer [34]. The interfacial shear stress as a function of the indenter displacement for the interlayer Young's modulus in the range of 1 to 40 GPa is shown in Figure 6a. As can be seen from Figure 6a, the use of the interlayer with the higher modulus means that the interlayer/fiber interface must be stronger in order to avoid interphase shear failure. Also, the shear yield strength of the interlayer must be higher than the applied shear stress. Thermosetting or thermoplastic coatings are poor in shear [35], and are, therefore, unsuitable for use as functional interlayers in high-performance fiber-reinforced polymer composites. However, the plasma coatings deposited (PECVD) from organosilicon precursors have a sufficiently high shear yield strength at a relatively low Young's modulus [25], as opposed to thermosetting or thermoplastic coatings (see the schematic comparison in Figure 6b). Therefore, the plasma coatings may be more suitable as functional interlayers.

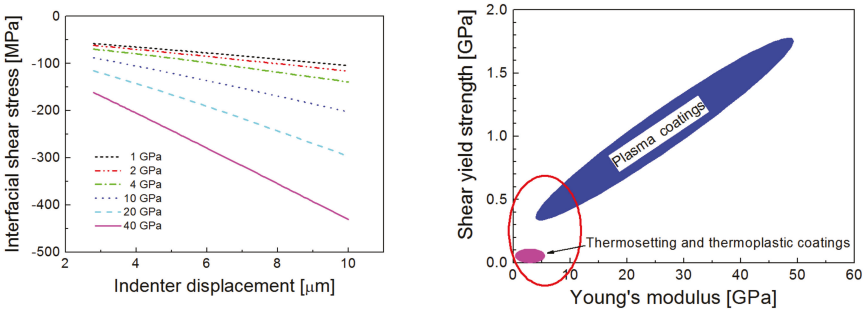

Figure 6. Model simulations: (**a**) shear stress at interlayer/fiber interface as a function of indenter displacement for interlayers with different Young's moduli during the microindentation test, (**b**) schematic correlation between shear yield strength and Young's modulus for plasma coatings [25] and thermosetting or thermoplastic coatings.

In our previous work, an oxygen-free TVS was successfully used for plasma coating of GFs in the RF helical coupling system to enhance the interfacial adhesion in GF/polyester composites [36]. In that case, the Young's modulus of the interlayer was increased from 9.4 to 23 GPa, reducing the vinyl concentration with an enhanced power of 0.1–5.0 W, but the adhesion of the interlayer to the GF did not significantly improve. In another study, therefore, a mixture of TVS precursor in gaseous oxygen was used to deposit plasma coatings onto GFs. Incorporating oxygen atoms into plasma coatings can increase interfacial adhesion, not only on the GF surface, but also at the interface with the polyester matrix due to better wettability and higher density of interfacial bonds. Indeed, the IFSS for oxidized plasma coatings was up to 21% higher than that for the non-oxidized interlayer, indicating the direct chemical effect of oxygen atoms on the interphase properties [34]. A nanoscratch test was used to measure the interlayer adhesion on a flat glass substrate, as well as on a single GF. For a given film, consistent interlayer adhesion was identified for both fibrous and planar glass substrates [37]. The work of adhesion was used as the right parameter for the characterization of the interlayer adhesion measured by a nanoscratch test. A strong correlation was found between the IFSS in GF/polyester composites and the interlayer adhesion for the same plasma coating [38]. Model and experimental data showed that the shear strength at the interlayer/fiber interface is the key factor affecting the mechanical response of the plasma-coated fibers in a GF/polyester composite at microindentation testing.

Further enhancement of the adhesion of oxidized plasma coatings deposited at higher power was our motivation to test an improvement of IFSS for GF/polyester composites. A set of interlayers was deposited onto silicon wafers and GF bundles at a constant effective power of 5.0 W, but the various oxygen fractions in the TVS/O_2 mixture varied from 0 to 0.46 (0, 0.10, 0.21, 0.33, and 0.46) in the RF helical coupling system. Using the same power, the power density in the RF helical coupling system was significantly lower, due to a higher volume of plasma discharge, compared to the plasma reactor equipped with parallel electrodes. This means that plasma coatings synthetized in the RF helical coupling system contain a higher concentration of hydrogen atoms and are less cross-linked. The Young's modulus of plasma coatings deposited on silicon wafers was determined from nanoindentation measurements for various oxygen fractions in the TVS/O_2 mixture (Figure 7a). The Young's modulus decreased from 22 to 18 GPa as a result of an increase in oxygen concentration from 0 to 11 atom% in a-CSiO:H films (Figure 7b). Chemical analysis (RBS/ERDA) showed that the C/Si and H/Si ratios in all films were approximately 7.1 and 10, respectively, but the O/Si ratio increased from 0 to 2.4 with the enhanced oxygen fraction (Figure 7b). FTIR spectra indicate that oxygen atoms were incorporated into hydroxyl, carbonyl, and Si–O–C/Si–O–Si species, and the intensity

and area of the absorption bands increased with enhanced oxygen fraction (Figure 7c). This trend is consistent with the previous analysis [39]. This means that the number of Si–C species in the a-CSi:H film deposited from pure TVS were reduced at the expense of the newly formed Si–O–C species in a-CSiO:H films synthetized from TVS in a mixture with oxygen gas. An increase in the number of Si–O–C/Si–O–Si species was important for increased adhesion at the interlayer/glass interface due to chemical reactions of plasma species with hydroxyl groups on the surface of the glass. By increasing the oxygen fraction, only a slight reduction of the vinyl groups in the film can be expected (Figure 7c). The vinyl groups on the interlayer surface are responsible for chemical bonding with the polyester resin during the curing process. The formation of hydroxyl and carbonyl groups eliminates one and two bonds, respectively, from each carbon atom that could potentially be used for cross-linking the network. Therefore, decreased cross-linking of the carbon-silicon oxide network with an increased oxygen fraction resulted in a film density reduction of 1.47 to 1.31 g/cm^3 (Figure 7d), as determined from the RBS spectra, and also resulted in a reduced Young's modulus (Figure 7a).

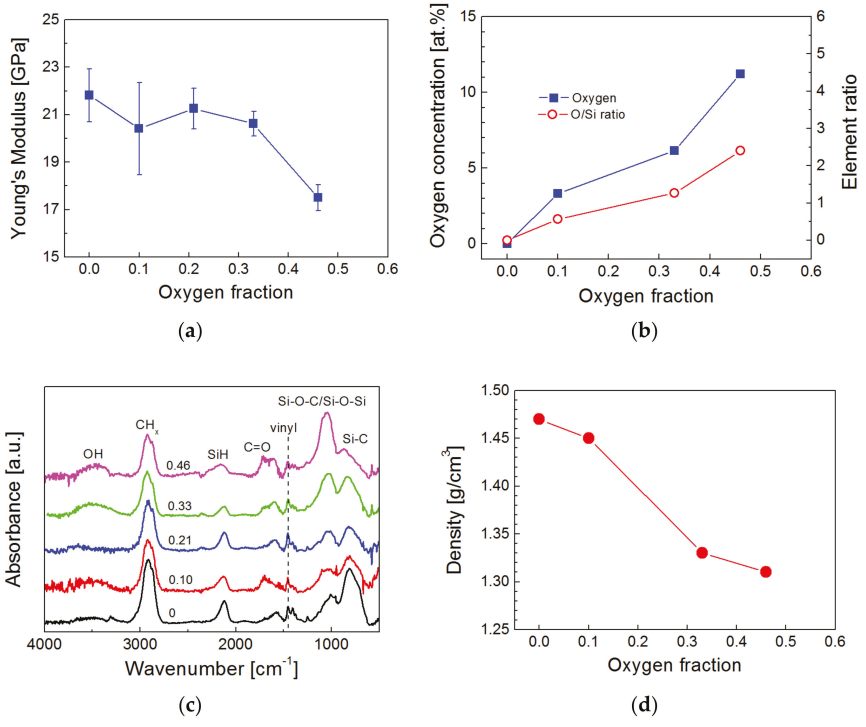

Figure 7. Analysis of thin films deposited on silicon wafers at 5.0 W from the tetravinylsilane (TVS)/O_2 mixture at different oxygen fractions 0–0.46: (**a**) Young's modulus determined from nanoindentation measurements, (**b**) oxygen concentration together with the O/Si ratio evaluated from Rutherford backscattering spectrometry (RBS)/elastic recoil detection analysis (ERDA) spectra, (**c**) infrared spectra for oxygen fractions 0–0.46, and (**d**) density of the film estimated from RBS spectra.

Interlayers with the properties shown in Figure 7 were also deposited on an unsized GF bundle of 1600 single filaments. The GF bundle was positioned along the axis of the axially symmetric plasma, resulting in the deposition of a uniform and homogeneous coating around the fibers [36]. TVS molecules were fragmented during the plasma process to form free radicals, and these highly reactive radicals recombined on the surface of the GFs to form an interlayer. Because of the low pressure (1.4 Pa) during the

plasma process, free radicals diffuse into the central part of the GF bundle and form an interlayer even on the surface of the central fibers. The thickness of the interlayer is controlled by deposition time at a known deposition rate, which is constant during deposition. However, the interlayer on the central fibers is thinner than that on the fibers at the edge of the bundle, because the deposition rate decreases radially into the GF bundle due to the shadow effect of the surrounding fibers. We found that the thickness of the film deposited on the silicon wafer under a single GF was reduced by a factor of 0.9, due to the shadow effect, after the deposition process with plan-parallel electrodes. Multiple shielding can be expressed in a geometric series as $t_n = t_s\, q^{n-1}$, where t_s is the film thickness on the fiber at the edge of the bundle, t_n is the film thickness on the n-th fiber in the direction toward the center of the bundle shielded by $n-1$ fibers, and q is the shielding factor. For the GF bundle with a circular cross-section of 1600 single filaments, 22 is the order of the fiber in the center of bundle, and for t_s = 1.0 µm, q = 0.9, the film thickness is t_{22} = 109 nm on the central GF. The thickness of the interlayer on the central GF is, therefore, ten times smaller than the thickness of the interlayer on the fiber at the edge of the bundle. The expected thickness of the interlayer varied between 1.0 and 0.1 µm across the GF bundle for all tested GFs. The plasma-coated GF bundle was embedded in the polyester resin, and was cured to form a unidirectional GF/polyester composite. The polished cross-section of the composite sample was subjected to microindentation testing for the IFSS evaluation. The mean value and its standard deviation were calculated from measurements of ten fibers selected from different parts of the bundle cross-section. No evident differences between IFSS values for central and edge fibers were observed, which corresponds to the previous results [34]. The dependence of IFSS on the oxygen fraction in the TVS/O_2 mixture for plasma-coated GFs with an interlayer thickness of 1.0 µm (edge fibers) at an effective power of 5.0 W is given in Figure 8a. The IFSS (blue square) ranged from 130 to 139 MPa at a fiber volume fraction of approximately 0.53 in the GF/polyester composite. The maximum IFSS at a 0.33 oxygen fraction corresponds to the highest adhesion of the interlayer on glass substrate characterized by the work of adhesion (red circle) [38]. A 3.4-fold increase in the adhesion of the a-CSiO:H film (0.33 oxygen fraction), due to a raised concentration of Si–O–C/Si–O–Si bonding species at the interlayer/glass interface, compared to the a-CSi:H film (zero oxygen fraction) was promising for using the adhesive film as a functional interlayer in the GF/polyester composite. The IFSS trend corresponds to the adhesion trend (Figure 8a), but the statistical significance of the maximum IFSS is not entirely convincing. Although there are differences between the microindentation test and the nanoscratch test in the specimen loading and failure mechanics, and both the IFSS and the work of adhesion are calculated based on simplified assumptions, the interlayer adhesion on the glass surface was shown to control the shear strength in the GF/polyester composite [38].

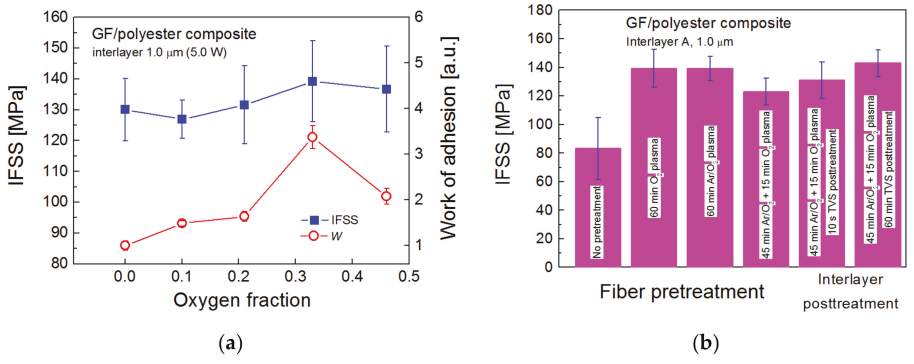

Figure 8. Interfacial shear strength (IFSS) for plasma-coated glass GFs in the GF/polyester composite: (**a**) IFSS as a function of oxygen fraction in the TVS/O_2 mixture used to deposit the interlayer at 5.0 W, (**b**) effect of GF pretreatment and post-treatment of plasma-coated GFs on IFSS for the same Interlayer A.

The effect of GF pretreatment and post-treatment of plasma-coated GFs on IFSS is demonstrated for the same Interlayer A (type A: 0.33 oxygen fraction, 5.0 W) in Figure 8b. The strong adhesion at the interlayer/fiber interface was primarily achieved by pretreatment of GFs with O_2 plasma, which cleans and activates the fiber surface due to physical and chemical etching before the interlayer is deposited. The deposition of Interlayer A on GFs without pretreatment resulted in a significant reduction of IFSS to 83 MPa compared to 139 MPa for GFs pretreated with O_2 plasma at 25 W for 60 min (Figure 8b). Ar gas (4.0 sccm) was mixed with O_2 gas (0.5 sccm) to increase the degree of ionization during the pretreatment of GFs, but the IFSS of 139 GPa was the same as in the pretreatment with O_2 plasma using the same Interlayer A. The IFSS value was reduced to 123 GPa when Ar/O_2 plasma was applied for 45 min followed by O_2 plasma for 15 min during the pretreatment procedure. This means that the cleaning and activation of the GF surface was not so effective, probably because of the interruption of the pretreatment process to change the gas mixture. This pretreatment method, however, was used for the other two samples, where, after the deposition of Interlayer A, the plasma-coated GFs were left in the reactor filled with TVS vapor for 10 s or 60 min without RF discharge. During this post-treatment procedure, the TVS molecules are not only physisorbed, but also chemisorbed on the chemically active surface of the interlayer that contains free radicals. An ultrathin overlayer, rich in vinyl groups, is formed on the interlayer surface during the application of TVS vapor. This layer may be important for improved adhesion at the polymer matrix/interlayer interface due to chemical bonding of vinyl groups with polyester resin during the curing process. Progress in the IFSS of 8 and 20 MPa (up to 143 MPa) was found for the interlayer, post-treated for 10 s and 60 min, respectively.

Interlayer B, deposited from pure TVS at an effective power of 0.1 W, contains no polar groups, but contains a higher concentration of vinyl groups compared to Interlayer A, as evident from the FTIR spectra (Figure 9a). Interlayer B could, therefore, be used to improve chemical bonding between the polymer matrix and the interlayer, similar to the ultrathin overlayer deposited from TVS vapor during the post-treatment procedure. In addition, Interlayer B has a lower Young's modulus of 9.4 GPa [36], which is beneficial for decreasing shear stress across the interphase region (Figure 6a). Interlayer B was combined with Interlayer A to form a bilayer that was tested to improve the IFSS in GF/polyester composites. Interlayer A, containing 6.1 atom% of oxygen, was deposited on the GF bundle followed by the oxygen-free Interlayer B in three thickness variations: 0.9 μm (Interlayer A) + 0.1 μm (Interlayer B), 0.1 μm (Interlayer A) + 0.9 μm (Interlayer B), and 0.05 μm (Interlayer A) + 0.05 μm (Interlayer B). The resulting IFSS values were compared with the single Interlayer A in Figure 9b. All the results in Figure 9b correspond to GFs pretreated with Ar/O_2 plasma for 45 min, followed by O_2 plasma for 15 min. The IFSS for bilayers was slightly higher by 1 to 4 MPa, which was statistically insignificant. The bilayer thickness was only 0.1 μm on edge fibers for the third bilayer, meaning that the bilayer thickness was only 0.01 μm on the central fibers. The final bilayer was prepared from the C and D interlayers by diluting the deposition plasma by adding 1.0 sccm of Ar gas to increase the ionization degree, and the total flow rate was, therefore, 1.8 sccm. Interlayer C was deposited from a $TVS/O_2/Ar$ mixture with a 0.15 oxygen fraction and a 0.55 argon fraction at an effective power of 5.0 W, but Interlayer D was synthesized from a TVS/Ar mixture with a 0.55 argon fraction at 0.1 W. The deposition rates for this bilayer were not known, but a significantly reduced IFSS value of 47 MPa indicates that the bilayer thickness was not sufficient for a uniform fiber coating, probably <0.1 μm (edge fibers). This means that part of the GF surface was not covered by the interlayer.

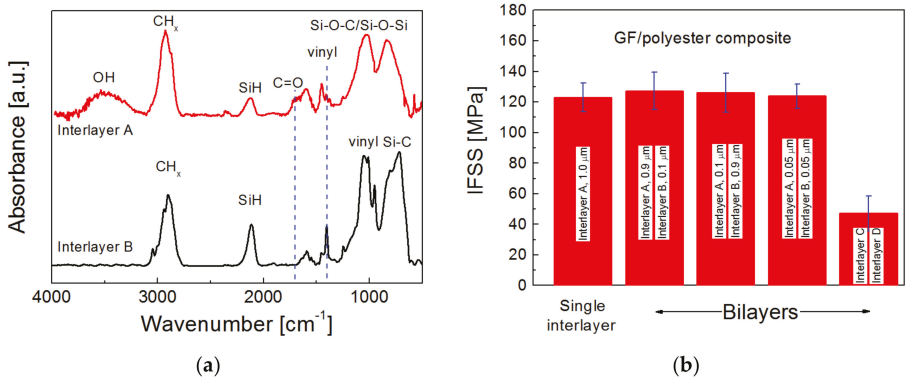

Figure 9. (**a**) Infrared spectra of Interlayers A and B, (**b**) effect of the bilayer on IFSS for the same pretreatment of GFs.

The final comparison of IFSS values for the GF/polyester composite in Figure 10 includes unsized, O_2-plasma pretreated but uncoated, commercially sized, and optimized plasma-coated GFs. No chemical bonding at the polymer matrix/fiber interface for unsized GFs with an IFSS of 29 MPa is expected. O_2-plasma pretreatment of GFs without deposition of an interlayer resulted in improved interfacial adhesion at the polymer matrix/fiber interface, but the IFSS at 49–50 MPa was limited by the shear failure of the matrix, as demonstrated by model simulations [34]. The IFSS of 105 MPa for commercially sized GFs was twice as high compared to GFs pretreated with O_2 plasma. However, the optimized Interlayer A deposited on O_2- or Ar/O_2-plasma pretreated GFs resulted in an IFSS of 139 MPa. A further increase in IFSS to 143 MPa was achieved by the subsequent post-treatment of Interlayer A in TVS vapor for 60 min.

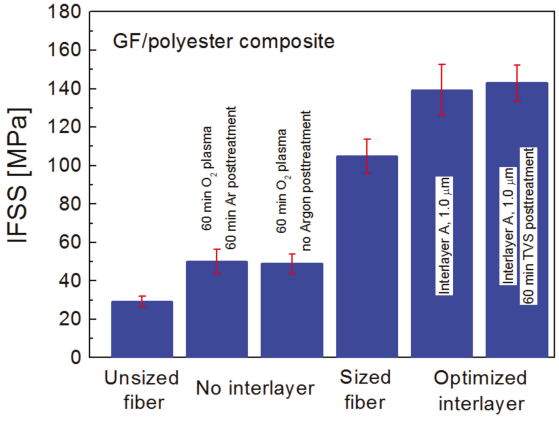

Figure 10. Interfacial shear strength (IFSS) for the GF/polyester composite reinforced with unsized, O_2-plasma pretreated but uncoated, commercially sized, and optimized plasma-coated GFs.

Plasma coatings of tailored physicochemical properties have potential applications in high-performance polymer composites with a controlled interphase. Plasma nanotechnology is a promising technique for the construction of gradient interlayers needed for the new concept of composites without interfaces [40].

4. Conclusions

A wide range of polymer-to-glass materials was plasma synthesized (PECVD) to control their mechanical properties with Young's moduli from 10 to 52 GPa. The oxygen-free (a-CSi:H) and oxygen-bound (a-CSiO:H) films of 1.0-μm thickness were deposited from pure TVS and TVS mixed with oxygen gas on planar and fibrous substrates. Cyclic nanoindentation was used to determine the Young's modulus for films deposited on planar substrates. Single GFs coated by the interlayer were embedded into the polyester resin to form a model composite. The polished cross-section of the model composite was used to distinguish the composite phases, due to their different mechanical properties, with Modulus Mapping. The maps of storage modulus allowed defining the interlayer between the fiber surface and the polymer matrix. The results showed that the mechanical properties, along with the deposition rates, are consistent for films on planar and fibrous substrates. Modulus Mapping revealed that the thickness of the modified matrix increased up to 0.7 μm with the raised Young's modulus at 52 GPa for the SiO_2-like interlayer. We assumed that the modified matrix region was created due to chemical bonding at the polymer matrix/interlayer interface, unlike the unsized fiber, where no interphase region was observed. Thus, a strong interfacial adhesion between the polymer matrix and stiffer material (interlayer) may result in the formation of a modified matrix region with gradually increased Young's modulus. The thickness of the modified matrix increased with the increasing difference between the interlayer and the polymer matrix moduli. Plasma organosilicon coatings with a relatively low Young's modulus (polymer-like material) have a shear yield strength that is significantly higher than that for thermosetting and thermoplastic coatings. This means that the plasma coatings with controlled interfacial adhesion and Young's modulus are promising as interlayers in polymer composites. Selected compatible interlayers with increased interlayer adhesion were deposited onto a 1600-filament GF bundle. The interlayer thickness on the fibers at the edge of the bundle was found to be reduced by one order for fibers in the center of the bundle as a result of the shadow effect. Optimized interlayer adhesion (0.33 oxygen fraction, 5.0 W) resulted in an IFSS of 139 MPa, supported by O_2 and Ar/O_2 pretreatment of GFs. The IFSS was reduced to 83 MPa if the pretreatment procedure was omitted. The GF pretreatment was, therefore, very important for cleaning and activating the surface of the fibers. Following the plasma coating, the optimized interlayer was then post-treated in TVS vapor to increase the concentration of vinyl groups on the interlayer surface. The post-treatment procedure increased the IFSS to 143 MPa, which is 3.9 times higher than unsized GFs, 1.9 times higher than O_2-plasma pretreated GFs, and 36% higher than commercially sized GFs.

Author Contributions: A.K. deposited the interlayers, produced the composite samples, performed the microindentation tests, and analyzed the data; J.L. designed and performed the Modulus Mapping, and analyzed the data; L.T.D. provided the model simulations, as well as advice and discussions about the microindentation test and interface/interphase phenomena; V.C. provided the idea for this study, proposed the deposition conditions and experiments, analyzed and discussed the data, and wrote the paper.

Funding: This research was funded by the Grantová Agentura České Republiky, grant no. 16-09161S.

Acknowledgments: The authors would like to thank Petr Kucharcik for technical assistance, Erik Palesch for cyclic nanoindentation measurements, Vratislav Perina for RBS/ERDA analysis, and Miroslav Sirovy and Saint-Gobain Adfors CZ s.r.o. for providing glass fibers.

Conflicts of Interest: The authors declare no conflict of interest.

References

1. Drzal, L.T.; Rich, M.J.; Lloyd, P.F. Adhesion of graphite fibers to epoxy matrices: I. the role of fiber surface treatment. *J. Adhes.* **1983**, *16*, 1–30. [CrossRef]
2. Karger-Kocsis, J.; Mahmood, H.; Pegoretti, A. Recent advances in fiber/matrix interphase engineering for polymer composites. *Prog. Mater. Sci.* **2015**, *73*, 1–43. [CrossRef]
3. Ikuta, N.; Yanagawa, A.; Suzuki, Y.; Ochiai, S. Investigation on resin interphase produced near silane-treated glass fiber in vinyl ester resin. *Compos. Interfaces* **2000**, *7*, 511–515. [CrossRef]

4. Wu, Q.; Li, M.; Gu, Y.; Li, Y.; Zhang, Z. Nano-analysis on the structure and chemical composition of the interphase region in carbon fiber composite. *Compos. Part A* **2014**, *56*, 143–149. [CrossRef]
5. Uribe, B.E.B.; Tarpani, J.R. Interphase analysis of hierarchical composites via transmission electron microscopy. *Compos. Interfaces* **2017**, *24*, 849–859. [CrossRef]
6. Wu, Q.; Li, M.; Gu, Y.; Li, Y.; Zhang, Z. Imaging the interphase of carbon fiber composites using transmission electron microscopy: Preparations by focused ion beam, ion beam etching, and ultramicrotomy. *Chin. J. Aeronaut.* **2015**, *28*, 1529–1538. [CrossRef]
7. Deschler, J.; Seiler, J.; Kindersberger, J. Detection of charges at the interphase of polymeric nanocomposites. *IEEE Trans. Electr. Insul.* **2017**, *24*, 1027–1037. [CrossRef]
8. Gao, S.L.; Mäder, E. Characterisation of interphase nanoscale property variations in glass fibre reinforced polypropylene and epoxy resin composites. *Compos. Part A* **2002**, *33*, 559–576. [CrossRef]
9. Cech, V.; Palesch, E.; Lukes, J. The glass fiber-polymer matrix interface/interphase characterized by nanoscale imaging techniques. *Compos. Sci. Technol.* **2013**, *83*, 22–26. [CrossRef]
10. Huang, H.; Dobryden, I.; Thoren, P.A.; Ejenstam, L.; Pan, J.; Fielden, M.L.; Haviland, D.B.; Claesson, P.M. Local surface mechanical properties of PDMS-silica nanocomposite probed with Intermodulation AFM. *Compos. Sci. Technol.* **2017**, *150*, 111–119. [CrossRef]
11. Sharahi, H.J.; Shekhawat, G.; Dravid, V.; Park, S.; Egberts, P.; Kim, S. Contrast mechanisms on nanoscale subsurface imaging in ultrasonic AFM: Scattering of ultrasonic waves and contact stiffness of the tip–sample. *Nanoscale* **2017**, *9*, 2330–2339. [CrossRef] [PubMed]
12. Gibson, R.F. A review of recent research on nanoindentation of polymer composites and their constituents. *Compos. Sci. Technol.* **2014**, *105*, 51–65. [CrossRef]
13. Hardiman, M.; Vaughan, T.J.; McCarthy, C.T. A review of key developments and pertinent issues in nanoindentation testing of fibre reinforced plastic microstructures. *Compos. Struct.* **2017**, *180*, 782–798. [CrossRef]
14. Hardiman, M.; Vaughan, T.J.; McCarthy, C.T. The effect of fibre constraint in the nanoindentation of fibrous composite microstructures: A finite element investigation. *Comput. Mater. Sci.* **2012**, *64*, 162–167. [CrossRef]
15. Hardiman, M.; Vaughan, T.J.; McCarthy, C.T. Fibrous composite matrix characterisation using nanoindentation: The effect of fibre constraint and the evolution from bulk to in-situ matrix properties. *Compos. Part A* **2015**, *68*, 296–303. [CrossRef]
16. Gu, Y.; Li, M.; Wang, J.; Zhang, Z. Characterization of the interphase in carbon fiber/polymer composites using a nanoscale dynamic mechanical imaging technique. *Carbon* **2010**, *48*, 3229–3235. [CrossRef]
17. Martínez-Tong, D.E.; Najar, A.S.; Soccio, M.; Nogales, A.; Bitinis, N.; López-Manchado, M.A.; Ezquerra, T.A. Quantitative mapping of mechanical properties in polylactic acid/natural rubber/organoclay bio nanocomposites as revealed by nanoindentation with atomic force microscopy. *Compos. Sci. Technol.* **2014**, *104*, 34–39. [CrossRef]
18. Joliff, Y.; Rekik, W.; Belec, L.; Chailan, J.F. Study of the moisture/stress effects on glass fibre/epoxy composite and the impact of the interphase area. *Compos. Struct.* **2014**, *108*, 876–885. [CrossRef]
19. Niu, Y.F.; Yang, Y.; Gao, S.; Yao, J.W. Mechanical mapping of the interphase in carbon fiber reinforced poly(ether-ether-ketone) composites using peak force atomic force microscopy: Interphase shrinkage under coupled ultraviolet and hydro-thermal exposure. *Polym. Test.* **2016**, *55*, 257–260. [CrossRef]
20. Huang, H.; Dobryden, I.; Ihrner, N.; Johansson, M.; Ma, H.; Pan, J.; Claesson, P.M. Temperature-dependent surface nanomechanical properties of a thermoplastic nanocomposite. *J. Colloid Interface Sci.* **2017**, *494*, 204–214. [CrossRef] [PubMed]
21. Riaño, L.; Belec, L.; Chailan, J.F.; Joliff, Y. Effect of interphase region on the elastic behavior of unidirectional glass fiber/epoxy composites. *Compos. Struct.* **2018**, *198*, 109–116. [CrossRef]
22. Cech, V.; Lasota, T.; Palesch, E.; Lukes, J. The critical influence of surface topography on nanoindentation measurements of a-SiC:H films. *Surf. Coat. Technol.* **2015**, *261*, 114–121. [CrossRef]
23. Cech, V.; Lukes, J.; Palesch, E.; Lasota, T. Elastic modulus and hardness of plasma-polymerized organosilicones evaluated by nanoindentation techniques. *Plasma Process. Polym.* **2015**, *12*, 864–881. [CrossRef]
24. Drzal, L.T.; Herrera-Franco, P.J.; Ho, H. Fiber-matrix interface tests. In *Comprehensive Composite Materials*, 1st ed.; Kelly, A., Zweben, C., Eds.; Elsevier: Amsterdam, The Netherlands, 2000.

25. Cech, V.; Hosein, H.A.; Lasota, T.; Drzal, L.T. Mechanical properties of plasma-polymerized tetravinylsilane films. *Plasma Process. Polym.* **2011**, *8*, 138–146. [CrossRef]
26. Cech, V. Plasma polymer film as a model interlayer for polymer composites. *IEEE Trans. Plasma Sci.* **2006**, *34*, 1148–1155. [CrossRef]
27. Oliver, W.C.; Pharr, G.M. An improved technique for determining hardness and elastic modulus using load and displacement sensing indentation experiments. *J. Mater. Res.* **1992**, *7*, 1564–1583. [CrossRef]
28. Trivedi, R.; Hoferek, L.; Cech, V. Depth profile of mechanical properties of plasma-polymerized tetravinylsilane films evaluated by cyclic nanoindentation. *Surf. Coat. Technol.* **2011**, *205*, S470–S474. [CrossRef]
29. Fischer-Cripps, A.C. *The IBIS Handbook of Nanoindentation*; Fischer-Cripps Laboratories: Forestville, Australia, 2005; p. 42.
30. Syed Asif, S.A.; Wahl, K.J.; Colton, R.J.; Warren, O.L. Quantitative imaging of nanoscale mechanical properties using hybrid nanoindentation and force modulation. *J. Appl. Phys.* **2001**, *90*, 1192–1200. [CrossRef]
31. Cech, V.; Janecek, P.; Lasota, T.; Bursa, J. A fiber-bundle pull-out test for surface-modified glass fibers in GF/polyester composite. *Compos. Interfaces* **2011**, *18*, 309–322. [CrossRef]
32. *The Interfacial Testing System (ITS)*; The Dow Chemical Company: Freeport, TX, USA, 2002.
33. Cech, V.; Knob, A.; Lasota, T.; Lukes, J.; Drzal, L.T. Surface modification of glass fibers by oxidized plasma coatings to improve interfacial shear strength in GF/polyester composites. *Polym. Compos.* **2017**. [CrossRef]
34. Jones, F.R. A review of interphase formation and design in fibre-reinforced composites. *J. Adhes. Sci. Technol.* **2010**, *24*, 171–202. [CrossRef]
35. Liu, K.; Piggott, M.R. Shear strength of polymers and fibre composites: 1. Thermoplastic and thermoset polymers. *Composites* **1995**, *26*, 829–840. [CrossRef]
36. Cech, V.; Knob, A.; Hosein, H.A.; Babik, A.; Lepcio, P.; Ondreas, F.; Drzal, L.T. Enhanced interfacial adhesion of glass fibers by tetravinylsilane plasma modification. *Compos. Part A* **2014**, *58*, 84–89. [CrossRef]
37. Palesch, E.; Cech, V. Characterization of interlayer adhesion on single glass fibers and planar glass using the nanoscratch test technique. *Thin Solid Films* **2017**, *636*, 353–358. [CrossRef]
38. Palesch, E.; Knob, A.; Plichta, T.; Cech, V. Functional interlayers with controlled adhesion developed for polymer composites. *Thin Solid Films* **2018**, *656*, 37–43. [CrossRef]
39. Bussey, D.; Perina, V.; Jones, F.R.; Cech, V. Effect of chemical modification on the mechanical properties of plasma-polymerized organosilicones. *Prog. Org. Coat.* **2018**, *119*, 85–90. [CrossRef]
40. Cech, V. Plasma polymer films: From nanoscale synthesis to macroscale functionality. In *Nanostructured Thin Films and Coatings*; Zhang, S., Ed.; CRC Press: New York, NY, USA, 2010; Volume 1, pp. 481–527. ISBN 9781420094039.

fibers

MDPI

Article

Investigation of Transcrystalline Interphases in Polypropylene/Glass Fiber Composites Using Micromechanical Tests

Hanna Brodowsky * and Edith Mäder

Leibniz-Institut für Polymerforschung Dresden, e.V. (IPF) Hohe Str. 6, D-01069 Dresden, Germany; emaeder@ipfdd.de

* Correspondence: brodowsky@ipfdd.de; Tel.: +49-351-4658-641

Received: 20 December 2017; Accepted: 30 January 2018; Published: 12 March 2018

Abstract: In composites, a strong interphase between the components is essential for mechanical properties. By using a suitable sizing (i.e., surface modification) of the fiber, the interphase may be varied, e.g., by suppressing or promoting heterogeneous nucleation of a thermoplastic matrix. In the latter case, three-dimensional transcrystallized interphases with properties differing from those of the bulk matrix are formed. Polypropylene-glass fiber composites are prepared as single-fiber model composites with (a) sizings either inducing or suppressing a transcrystalline interphase, (b) different amounts of modifier maleic acid anhydride grafted polypropylene, and (c) different molecular weights of the matrix polymer. These are studied in quasi-static or cyclic load tests. Static tests permit insights in the interfacial characteristics such as critical interface energy release rate, adhesion strength and frictional stress. Cyclic tests on these model composites can be used to study the nature of dissipative processes and the damage behavior. Atomic Force Microscopy (AFM) investigations of the fiber fracture surfaces provide supplementary information. The transcrystalline layer can indeed improve the mechanical parameters (a 70–100% increase of strength and a 25 or 125% increase in toughness, depending on the molecular weight (MW) of the matrix polymer at low modifier concentration). However, the effect is partially neutralized by an opposing effect: high nucleation in the bulk in samples with commonly used concentrations of modifier.

Keywords: polypropylene; glass fiber; polymer-matrix composites; interface; mechanical behavior; transcrystallinity; micromechanical tests

1. Introduction

Semicrystalline thermoplastics crystallize in spherulites. In absence of external nuclei, the homogeneous crystallization can only occur at temperatures below the crystallization temperature T_{cr}. The nucleation rate is material-dependent, it generally increases with the temperature difference T_{cr}-T [1]. Once nucleated, the growth of spherulites in the bulk occurs in all directions until it reaches the neighboring spherulites, which impede further growth. On surfaces, the nucleation may occur by heterogeneous nucleation at the surface and can be significantly higher than in the bulk. In this case, the impedation by neighboring crystallites occurs almost immediately in the lateral directions, leaving only the outward direction for crystal growth. Thus, a so-called transcrystalline (TC) layer at the surface is formed. Transcrystallization is a nucleation controlled crystallization process which can occur in a semicrystalline polymer in contact with a second material [2,3]. The growth mechanism itself, as well as the growth rate, is identical in the bulk and within the TC layer [4–7]. The thickness of the TC layer is therefore determined by the different rates of the two nucleation processes in the bulk and at the surface, in relation to the growth rate [5,8,9]. These three quantities depend on a number

of thermodynamic and physicochemical conditions, such as the surface free energy, the nucleation density and the sample temperature.

In the case of a semicrystalline thermoplastic/glass fiber (GF) composite, the fiber surface may be sized with the aim to induce a high nucleation density. The closely packed nuclei enforce a primarily outward growth of the crystallites. This leads to a TC interphase layer between the fiber surface and the semicrystalline bulk. Since early reports of transcrystallization [10,11], much effort has been put into the topic and there is still a controversial discussion, as the existence and structure of a TC layer have significant influence on the mechanical properties of the composite [1,4–6,12–17].

The surface free energy is determined by the type of fiber and the sizing or finish components, especially the coupling agent. The nucleation density can be increased by appropriate sizing components at the surface or by matrix additives for the bulk [18–20]. The roughness of the fibers can play a role [5,14,18], especially if epitaxial ordering at the surface is possible [21,22]. The sample temperature influences the nucleation rate at the interface and in the bulk, and the crystallization kinetics [23,24]. Due to the memory effect of incompletely melted polymer crystals, the "temperature history" since the last complete melting plays a role.

Occasionally, the term „transcrystallization" is used in the literature in connection with another phenomenon [25,26]. By applying a shear stress along the fiber axis, a columnar superstructure is formed even at $T > T_{cr,trans}$ which resembles a TC layer. It was even supposed that TC layers only occur as a result of shearing. However, Wu et al. [27] observed that shear leads to a cylindric crystallization. Varga and Karger-Kocsis [28] determined that this structure does not lead to increased adhesion strength, as the cylindric crystallites are nucleated homogeneously, unlike the heterogeneous nucleation of the TC layer, so no physical coupling occurs.

1.1. Structure of the TC Interphase

According to Pompe und Mäder [20], three different sections of the TC layer can be specified (Figure 1), which are influenced by the above mentioned parameters.

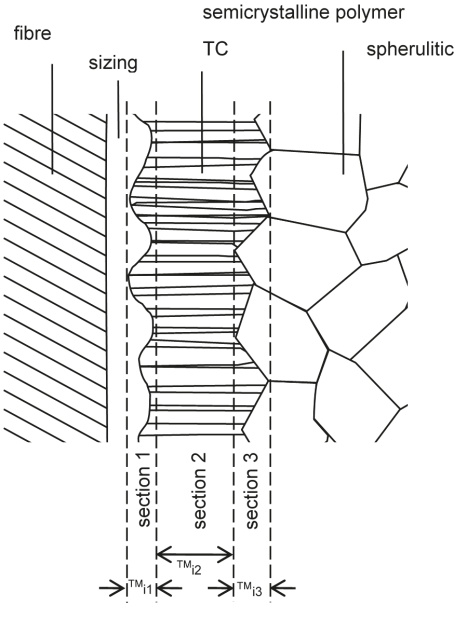

Figure 1. Scheme of the interphase between the fiber and a semicrystalline matrix forming a TC-layer.

Section 1, the nucleation region, includes the interface between fiber and the TC part of the matrix. It is here the nucleation takes place. A TC layer is only formed if the nucleation rate at the surface is higher than in the bulk, e.g., if the crystallization temperature of the interface induced nucleation is higher than that of the bulk crystallization, $T_{cr,bulk} < T_{cr,TC}$. The thickness of Section 1 is determined by the roughness of the interface. The crystal morphology within a layer of the thickness of around the distance of two nuclei is less well ordered compared to the TC layer beyond, where the crystal growth direction is primarily perpendicular to the surface. Within the surface layer, the nuclei grow in a hemisphere, until they are impeded by the neighboring nuclei. For some fiber/matrix combinations, the nuclei themselves have a preferred crystal orientation.

The adjacent Section 2 is the homogeneous part of the TC layer. Its extension is delimited by the impeding bulk spherulites. When its thickness $\delta_{i,2}$ is bigger, therefore, the more the TC layer can grow in the time interval between the nucleation at the interface and (a mean point in time of) bulk nucleation. These parameters can be adjusted via a sizing/finish with high nucleating ability, or by nucleating agents/nucleation suppressants within the polymer matrix. The crystal growth rate is determined by the temperature resp. the cooling rate. In the case of slow cooling or isothermal annealing at temperatures T with $T_{cr,bulk} < T < T_{cr,trans}$, an extended TC layer is formed [4–6,8,29]. In samples with high fiber density, the bulk spherulite region can even be fully suppressed [20].

Section 3 (cf. Figure 1) encloses the interface between the TC region and the surrounding bulk, i.e., between the TC and the spherulitic morphology. The thickness $\delta_{i,3}$ of this section as well as the specific surface area of the interface are determined by the size of the bordering spherulites [12].

1.2. The TC Interphase and Its Impact on the Micromechanics and Composite Properties

The influence of a TC interphase on the mechanical properties of the composite is actively and controversially discussed in the literature [26,28–32]. Clark et al. [16] report on polyamide (PA)/GF or PA/carbon fiber (CF) composites with higher strength but lower toughness in the case of transcrystallinity. In another experiment [29,33], PA/GF-composites were cooled at different rates, resulting in TC layers of different thicknesses. The slowly cooled samples with thicker TC layers had a Young's modulus increased by 30% and a bending modulus increased by 70%. However, slowing the cooling rate not only increased the TC layer thickness, but also the degree of crystallization of the matrix and the fraction of α-crystallized PA, making a comparison more difficult.

An intermediate step to study the interplay between the local crystal morphology and the composite properties is the micromechanical study of the influence of transcrystallization on the adhesion strength. The results so far are controversial. Bessel et al. [11] determined a reduced adhesion strength for TC samples. In a fragmentation test, Folkes and Wong [34] determined an increase in the critical fiber length, i.e., also a decrease of the adhesion strength due to TC layers in PP/GF composites. Similar results have been reported by Rolel et al. [35] for polyethylene (PE) matrix composites. In contrast, Carvalho and Bretas [36], Huson and McGill [31] as well as Feldman et al. [14] observed an increase in the adhesion strength due to transcrystallinity, for a number of different fibers in different thermoplastic matrices such as polypropylene (PP), polyethylene (PE) und polyamide (PA). Similarly, Clark et al. [15,16] found high interfacial shear strength and cohesive failure in TC samples, in contrast to adhesive failure of the interface in absence of a TC layer. Hsiao and Chen [30] observed that transcrystallinity had no significant effect on the adhesion strength for a number of composites. The situation is obviously complex, due to interaction and superposition of a number of parameters, influencing the interphase and the adhesion strength. The following paragraphs will discuss these parameters according to the scheme in Figure 1.

Section 1: this section is determined by the fiber interface, i.e., generally by the sizing or finish of the fiber. Sizings (on GF) or finishes (on CF) are used to increase the interfacial strength. Considering transcrystallinity, it is of importance if the surface can induce nuclei for heterogeneous crystallization. The resulting TC layers should act as a "physical coupling" between fiber and matrix [15], increasing the shear strength of this first section. This has been experimentally confirmed [37]. However, usually

the TC is reached via a sizing, which also influences the adhesion. In the present work, GF composites are compared whose sizings are identical except for the film former, with the aim to modify the nucleating properties at comparable adhesion strengths.

Section 2: The homogeneous region of the TC layer influences the composite properties via the properties of the TC morphology as compared to that of the bulk. The degree of crystallization is often higher than in the spherulitically crystallized regions [38]. Karger-Kocsis proposes that in an extended Section 2 the crystallization shrinkage might lead to a weak interface [39]. In the TC layer, the crystallites are smaller and radially aligned in reference to the fiber direction.

There are few experimental results focusing on this region in fiber-reinforced systems. By using specific scanning probe microscopic techniques (phase imaging, nanoindentation), the extension and the Young's modulus of the interphase between GF and PP matrix could be determined [40]. Within a TC layer, the local modulus is higher than in the bulk. Folkes and Hardwick [41] found an increase of storage modulus E' by a factor of 2 and higher shear and tensile strengths for a TC layer compared to a finely spherulitic layer. Marom et al. [38] confirmed these results by dynamic mechanical studies of microtomed sections containing predominantly TC polymer. The TC layer forming samples were more brittle and the fracture energy was smaller than comparable bulk samples. Microbeam synchrotron measurements of TC PP showed that under small load, no change in the microstructure is visible [42]. The authors attribute this to an "anchoring" of the TC layer lamella, confining the strain mainly to the amorphous phase.

Section 3: At the contact of the two crystallization fronts, a second interface is formed in Section 3. This interface is mechanically weak, due to the enrichment of low molecular weight species [43,44] as well as due to low entanglement density [45].

Transcrystallinity occurs in many technically relevant thermoplastics. It has a great influence on composite properties. The existence of a TC layer depends on a number of parameters, on the combination of the materials used as well as on processing conditions. More often than not, the resulting effect of TC morphology is an improvement, but this is by no means unequivocal. The aim of the present work is to study the effect of adhesion strength in PP/GF microcomposites where the fiber sizings are as similar as possible while either inducing a TC crystallization or suppressing it.

2. Experimental

2.1. Methods

In the last decade, several pieces of micromechanical equipment have been developed and set up at the IPF to investigate the interphase characteristics between fiber and matrix in composites. The micromechanical experiments include quasi-static pull-out tests, a hysteresis/micro-fatigue test as well as a dynamic test with sinusoidal loads up to 350 Hz. Figure 2 presents a scheme of the experiments. A vessel with matrix and an end-embedded fiber is clamped on an actuator that generates the displacement. The fiber end protruding out of the matrix is glued onto a mandrel that is fixed to a force sensor.

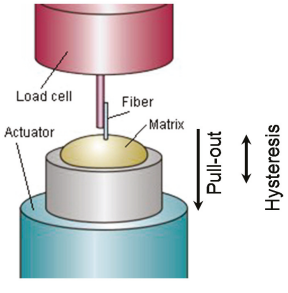

Figure 2. General scheme of used micromechanic tests: quasi-static pull out test and hysteresis tests.

The investigation of the adhesion strength parameters between fiber and polymer matrix is carried out with the pull-out setup [46]. Force-displacement curves are obtained by quasi-statically pulling a single fiber out of a polymer matrix. One distinctive feature of the device is the extremely low pull-out speed down to 10 nm/s. Forces between 1 mN to 5 N can be detected by a load cell. The experiment as well as data acquisition, analysis and statistical evaluation are performed by means of a "traditional approach" [47,48].

For the hysteresis and long-term loading test, the fiber is periodically loaded and the hysteresis loop is analyzed for the failure behavior [49]. The general setup (cf. Figure 2) is optimized for hysteresis measurements (low frequency range: 0–10 Hz) of single-fiber model composites, especially for long-term tests. A piezotranslator in combination with a piezoresistive load cell provides a zero backlash deflection and a long-term stable force measurement. Measurement data are the amplitude of the measured value, hysteresis, root point drift as well as elastic and loss energy. In long-term load tests (e.g., Wöhler, relaxation or load increase tests), the periodic change of the phase angle between force and elongation and the periodic change of stiffness and damping are analyzed.

An atomic force microscope AFM (Bruker, dimension) was used in the tapping mode to characterize the fiber surface and fracture surfaces.

Polarization microscopy is used to study the crystallization behavior of the PP matrix. Matrix material and separated single fibers are sandwiched between two glass plates. The thickness of the layer is determined by spacers (150 µm). The sandwiches are observed by polarization microscopy (Scope A1, Carl Zeiss, Oberkochen, Germany) using a hot plate (LTS350, Linkam, Tadworth, UK). The sandwich structures were heated to 192 °C for five minutes to fully melt the matrix. Then they are cooled to the crystallization temperature at 60 K/min.

2.2. Materials

GF were spun at the IPF spinning device. Yarns of 204 filaments were spun and sized with aqueous sizings. Two sizings are compared:

On the one hand APS-PP containing gamma aminopropyl triethoxisilane (APS) as coupling agent, and a PP film former (maleic acid anhydride grafted PP, MaPP), and on the other hand APS-PU with the coupling agent APS and a polyurethane (PU) film former. They are referred to as APS-PP and APS-PU fibers, respectively. As matrix PP, HD 120MO PP homopolymer (Borealis, MFR 8 g/10 min), a typical injection molding grade, and HH 450 PP homopolymer (Borealis MFR 37 g/10 min) a typical grade for fiber spinning applications were used, and are referred to as hiMW and lowMW PP. The two matrices were functionalized by either 0.5 or 2.1 wt % MaPP Exxelor PO 1020 (ExxonMobil Corp., Irving, TX, USA).

Fibers and matrix were compounded on a twin screw extruder and injection molded into standardized dog bone shaped specimens. The average fiber length was approx. 500 µm in all samples.

Tensile tests were conducted on the Universal Testing Machine Zwick 1456 (Zwick-Roell, Ulm, Germany), according to ISO 527-2/1A/50. Unnotched Izod impact tests were conducted with HIT 50P, Zwick/Roell, Germany according to ISO 179/1eU at room temperature and 50% relative humidity. Each value obtained represents the average of ten specimens.

The single-fiber model composites for quasi-static pull-out, hysteresis and cyclic loading investigations are all prepared in the same manner by using the IPF-made fiber embedding device [50] An 80 mg drop of matrix is melted. The pneumatically held fiber is positioned above the matrix with the aid of two long-distance microscope optics, monitoring the xy-positioning resp. the z-coordinate of the fiber above the matrix. The fiber is embedded with a micro drive (embedding length: 20–1000 µm with 0.1 µm accuracy—however, due to the formation of a meniscus, the embedding length may vary and is therefore optically determined after each pull out test). The complete temperature pattern is controlled by a PC (room temperature (RT) to 400 °C with 1 K accuracy). The chamber may be flushed with Argon.

3. Results

Figure 3 shows polarization micrographs of the single fiber in a neat HH450 PP film. Fibers were heated (10 K/min) to 210 °C for 0.50 min, then cooled at 200 K/min to the isothermal temperature T_{iso} = 135 °C, at which the crystallization behavior was observed.

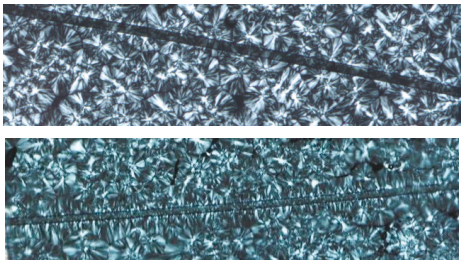

Figure 3. Polarization micrographs of single glass fibers in PP, T_{iso} = 135 °C, scalebar 100 µm. Top image: APS-PU sized fiber, bottom image: APS-PP sized fiber in HH450 PP matrix. The APS-PP sized fiber induces a TC layer.

Between crossed polarizers, the spherulites in the bulk PP film are clearly visible. Around the APS-PP sized fiber, a TC film of about 3 µm thickness is formed. This confirms an earlier differential scanning calorimetry study of the two sized fibers in PP, which showed that the APS-PU sized fiber induces no TC layer, whereas the APS-PP sized fiber induces a distinct TC layer [20].

The size of the spherulites for the two neat polymers is comparable. Adding 2% MaPP increases the nucleation density and therefore reduces the spherulite size, the crystallization is speeded up: the half time $t_{50\%}$ is reduced by 15%.

A series of GF/PP composites were compounded and injection molded with varying MaPP content, with fiber sizing known to induce or suppress a TC layer and differing PP molecular weight. Table 1 shows the mechanical properties of injection molded GF/PP specimens. In GF/PP composites, usually a small percentage of MaPP is added to improve adhesion as the maleic moieties form covalent bonds with the APS or weaker bonds with the OH on the glass surface. A side effect of MaPP is the nucleation of spherulites in the bulk. This side effect reduces the thickness of the TC layer. Therefore, the mechanical properties are determined at two concentrations of MaPP, a technically relevant 2% and a low 0.5%. For both PP grades, there is a slight improvement of tensile strength due to the TC in the 2% MaPP samples. In the case of 0.5% MaPP specimens, the effect of the TC layer is far more pronounced (albeit at a lower mechanical level). The toughness is doubled in the case of the TC interphase in high MW PP. The Young's modulus is increased strongly upon addition of GF, but does not depend on the TC interphase.

Table 1. Mechanical parameters of injection-molded specimens of GF reinforced PP.

		PP HD 120 hiMW			PP HH450 loMW		
		E (GPa)	**σ_m (MPa)**	**a_{cU} (J/m^2)**	**E (GPa)**	**σ_m (MPa)**	**a_{cU} (J/m^2)**
0.5% MaPP	APS-PP TC	6100	79	38	4900	68	21
	APS-PU Non-TC	5700	37	16	5400	38	17
	no fiber	1250	27	142	1300	27	121
2% MaPP	APS-PP TC	6500	93	55	5800	87	55
	APS-PU non-TC	6200	83	44	6100	83	44
	no fiber	1500		107	1300		87

Table 2 shows the results of micromechanical tests on single-fiber model composites. For both matrix PP grades, the local shear strength τ_d, the critical energy release rate of the interface, G_{ic} and

the frictional shear stress after debonding, τ_f, are greater for the TC composites. In this interphase sensitive method, the effect is clearly seen even in composites with 2% MaPP. AFM images of the pulled out fibers show clear differences in the fiber fracture surface, cf. Figure 4. For a TC interphase, the fracture surface is rough, with 500 nm structures dominating the surface morphology. In absence of a TC layer, no such structures are seen. These structures are interpreted as either the outer surface of the TC layer (Section 3 in Figure 1) or the sized fiber surface. A model for the fracture is proposed (right hand sind in Figure 4) where in the case of a TC interphase, the failure occurs outside the TC layer whereas without TC layer it occurs at the fiber surface.

Table 2. Micromechanical pull out tests results on GF /PP samples with 2.0% MaPP, parameters local shear strength, τ_d, the critical energy release rate of the interface, G_{ic}, and the frictional shear stress after debonding, τ_f.

	Sizing	τ_d	G_{ic}	τ_f
HH450	APS-PU	9.0	3.0	4.4
	APS-PP	15.7	8.3	6.1
HD120	APS-PU	10.0	3.4	5.4
	APS-PP	13.4	7.0	6.4

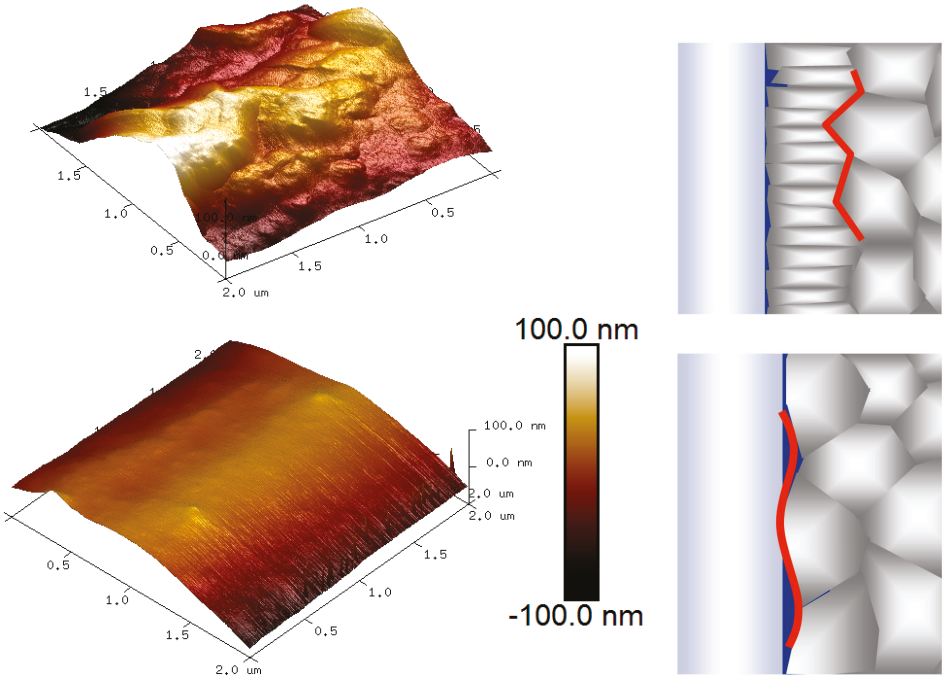

Figure 4. AFM height images of the fracture surfaces of single-fiber model composites after pull-out with HH450, Top: fibers inducing TC interphase, bottom: fibers suppressing a TC interphase. The height and size of the protrusions is 400 nm × 30 nm for the TC fracture surface and 50 nm × 8 nm for the non-TC fracture surface. A model for the fracture (right) is proposed where in the case of a TC interphase, the failure occurs outside the TC layer whereas without TC layer it occurs at the fiber surface.

In addition, micromechanical dynamical [51] and micromechanical hysteresis measurements [49] were performed on single-fiber model composites at two different embedded lengths, (200 µm, 600 µm).

Figure 5 shows the results of the hysteresis measurements for the four fiber matrix combinations high vs. low MW and TC vs. non-TC interphase for 600 µm embedded length. All samples remain intact with only some degradation. As the embedded length and fiber diameter vary, the value of the force as well as the stiffness (force/displacement) is subjected to error. However, the variation of stiffness with cycle number provides information on the degradation of the interphase, as well as the width of the hysteresis curve or the area included in the hysteresis loop, which is equal to the inelastic energy loss during the cycle (Figure 6). The stiffness of the high MW interphases is reduced by 20%, whereas the stiffness of the low MW samples is reduced by 40% at 40,000 cycles. This is independent on the interphase crystallization. The width of the hysteresis loop at zero force is initially higher for high MW than for lower MW, and for non-TC interphase samples than for the TC ones. Energy loss processes are higher for high MW and in the non-TC interphase. With cycle number, the non-TC samples hysteresis decreases whereas the TC interphases have a constant hysteresis width. Some interphase deterioration processes seem to occur in non-TC samples that are suppressed in samples with a TC interphase.

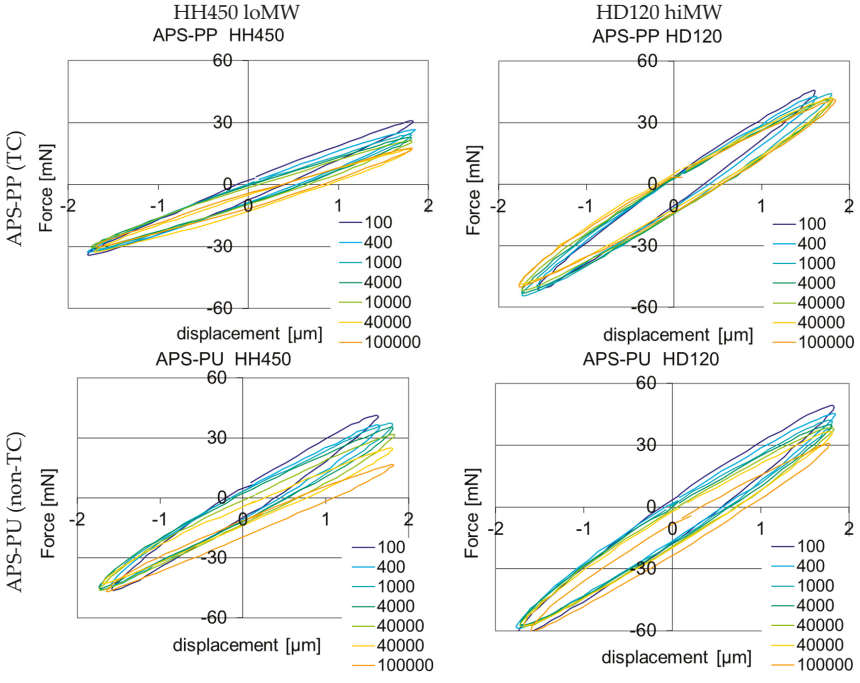

Figure 5. Hysteresis loops of single-fiber model composites loaded with amplitudes of ±1.8 µm at a frequency of 10 Hz (sized glass fibers APS/PP- or APS-PU-embedded in either PP HD120M or PP HH450) after the given number of cycles.

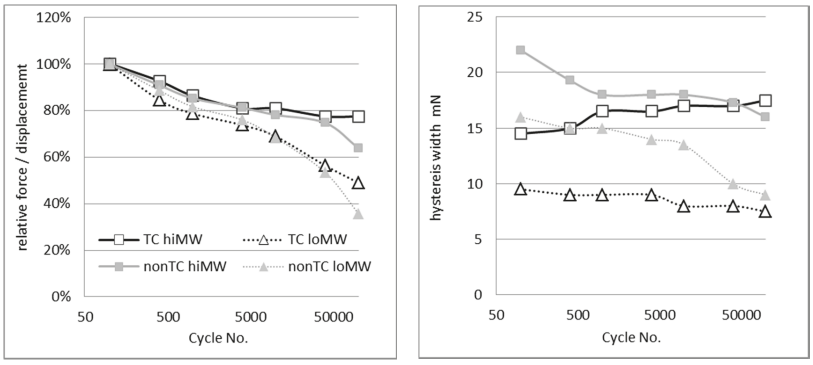

Figure 6. Data evaluated from the hysteresis curves: Relative stiffness (**left**) and width (**right**) of the hysteresis loops. Lines are guide to the eye.

If a smaller embedding length of 200 µm is chosen, the non-TC samples fail, whereas the transcrystalline samples remain intact up to 400,000 cycles.

The AFM images of either APS-PP or APS-PU fibers before embedding show a relatively smooth, homogeneous surface (Protrusions height <30 nm, diameter <100 nm, phase difference <15°). When the fiber is pulled out of the matrix after cyclic loading, the fracture surfaces are significantly more inhomogeneous (Figure 7). On the APS-PP surfaces, structures of the order of magnitude of 500 nm are found that are strongly oriented along the fiber (=load) axis. This longitudinal alignment is also found in the phase image. In the APS-PU sized fiber, the structures are significantly larger (2 µm), and the contrast in the phase image is much higher.

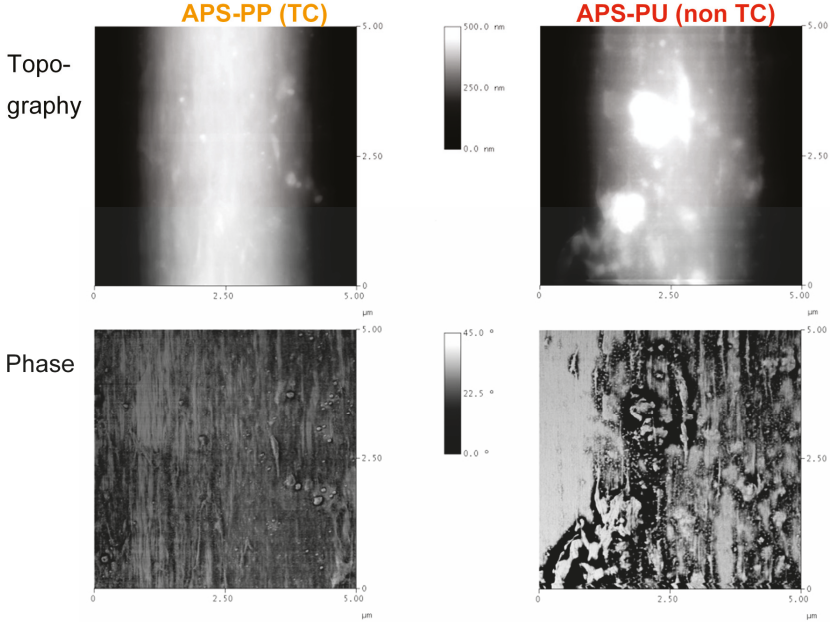

Figure 7. Tapping mode AFM images of fiber surfaces fractured after cyclic tests on single-fiber model composites.

For the APS-PP sized fibers, a TC structure is expected, leading to a fine-grained structure on the surface. The crystals are strongly deformed under load, but there is no material contrast, so the fracture surface is within the PP. In the APS-PU, an alignment of the crystallites is also observed, mainly in the phase image. The phase image also indicates a surface with varying material parameters, i.e., a fracture surface that is located partially in the PP/PU interphase and partially within the PP matrix: a number of larger spherulites adhere to the surface. They might be the cause for the higher friction seen in the micromechanical measurements.

4. Conclusions

A transcrystalline interphase has in the past been observed to improve]mechanical properties, but contradictory results have also been observed. In the present study, an enhancing effect of the transcrystalline layer is shown. However, it may be reduced due to the effect of additives such as MaPP, which is added as a coupling agent between fiber and PP matrix. As MaPP will also induce nucleation in the bulk, it reduces the effect of the transcrystalline layer. For standard MaPP concentration (2%), the effect of the remaining TC layer is weak, tensile strength and toughness are only increased by 5 to 10%. If only 0.5% of MaPP are added, the TC layer is more pronounced, leading to a 70–100% increase of strength and a 25 or 125% increase in toughness, depending on the MW of the matrix polymer. In single-fiber model composite interface-specific tests, such as the single-fiber pull out test or single fiber hysteresis test, the interphase enhancement due to the transcrystallization is evident even at 2% MaPP. For both matrix PP grades, the local shear strength, τ_d, the critical energy release rate of the interface, G_{ic}, and the frictional shear stress after debonding, τ_f, are greater for the TC composites. AFM images reveal a failure at the sizing layer for non-TC samples and failure at the outside of the TC layer in TC model composites.

Acknowledgments: The authors are indebted to Steffi Pressler and Alma Rothe for technical assistance, and to Wolfgang Jenschke for helpful discussions and for improving the micromechanical test setups. The authors thank the German Research Foundation DFG for financial support (Project MA 2311/1-1).

Author Contributions: Hanna Brodowsky and Edith Mäder studied the literature, conceived and designed the experiments. Hanna Brodowsky performed the experiments and analyzed the data; Hanna Brodowsky and Edith Mäder discussed the results, Hanna Brodowsky wrote the paper.

Conflicts of Interest: The authors declare no conflict of interest.

References

1. Ishida, H.; Bussi, P. Surface induced crystallization in ultrahigh-modulus polyethylene fiber-reinforced polyethylene composites. *Macromolecules* **1991**, *24*, 3569–3577. [CrossRef]
2. Billon, N.; Magnet, C.; Haudin, J.; Lefebvre, D. Transcrystallinity effects in thin polymer films. Experimental and theoretical approach. *Colloid Polym. Sci.* **1994**, *272*, 633–654. [CrossRef]
3. Wu, C.-M.; Chen, M.; Karger-Kocsis, J. Transcrystallization in syndiotactic polypropylene induced by high-modulus carbon fibers. *Polym. Bull.* **1998**, *41*, 239–245. [CrossRef]
4. Thomason, J.; Van Rooyen, A. Transcrystallized interphase in thermoplastic composites. *J. Mater. Sci.* **1992**, *27*, 897–907. [CrossRef]
5. Wang, C.; Liu, C.-R. Transcrystallization of polypropylene composites: Nucleating ability of fibers. *Polymer* **1999**, *40*, 289–298. [CrossRef]
6. Thomason, J.; Van Rooyen, A. The transcrystallised interphase in thermoplastic composites. In *Controlled Interphases in Composite Materials*; Springer: Dordrecht, The Netherlands, 1990; pp. 423–430.
7. Wang, C.; Hwang, L. Transcrystallization of ptfe fiber/pp composites (I) crystallization kinetics and morphology. *J. Polym. Sci. Part B Polym. Phys.* **1996**, *34*, 47–56. [CrossRef]
8. Wang, C.; Hwang, L. Transcrystallization of ptfe fiber/pp composites. II. Effect of transcrystallinity on the interfacial strength. *J. Polym. Sci. Part B Polym. Phys.* **1996**, *34*, 1435–1442. [CrossRef]
9. Assouline, E.; Pohl, S.; Fulchiron, R.; Gerard, J.-F.; Lustiger, A.; Wagner, H.; Marom, G. The kinetics of α and β transcrystallization in fiber-reinforced polypropylene. *Polymer* **2000**, *41*, 7843–7854. [CrossRef]

10. Jenckel, E.; Teege, E.; Hinrichs, W. Transkristallisation in hochmolekularen stoffen. *Colloid Polym. Sci.* **1952**, *129*, 19–24. [CrossRef]
11. Bessell, T.; Hull, D.; Shortall, J.B. Interface morphology and mechanical properties of unidirectional fiber reinforced nylon 6. *Faraday Spec. Discuss. Chem. Soc.* **1972**, *2*, 137–143. [CrossRef]
12. Raimo, M. On the origin of transcrystalline morphology in polymers and their composites: Re-evaluation of different views. *Mater. Today Commun.* **2015**, *3*, 137–140. [CrossRef]
13. Varga, J.; Karger-Kocsis, J. The occurence of transcrystallization or row-nucleated cylindritic crystallization as a result of shearing in a glass-fiber-reinforced polypropylene. *Compos. Sci. Technol.* **1993**, *48*, 191–198. [CrossRef]
14. Feldman, A.; Gonzalez, M.F.; Marom, G. Transcrystallinity in surface modified aramid fiber reinforced nylon 66 composites. *Macromol. Mater. Eng.* **2003**, *288*, 861–866. [CrossRef]
15. Clark, R.L.; Kander, R.G.; Sauer, B.B. Nylon 66/poly (vinyl pyrrolidone) reinforced composites: 1. Interphase microstructure and evaluation of fiber–matrix adhesion. *Compos. Part A Appl. Sci. Manuf.* **1999**, *30*, 27–36. [CrossRef]
16. Clark, R.L.; Craven, M.D.; Kander, R.G. Nylon 66/poly (vinyl pyrrolidone) reinforced composites: 2: Bulk mechanical properties and moisture effects. *Compos. Part A Appl. Sci. Manuf.* **1999**, *30*, 37–48. [CrossRef]
17. Levitus, D.; Kenig, S.; Kazanci, M.; Harel, H.; Marom, G. Effect of transcrystalline interface on the mechanical properties of polyethylene/polyethylene composites. *Adv. Compos. Lett.* **2001**, *10*, 61–65.
18. Chou, S.; Chen, S.-H. Effect of high temperature nucleating agent on adhesion of glass fibers to nylon 6-6. *Polym. Polym. Compos.* **2000**, *8*, 333–343.
19. Clark, R.; Kander, R.; Srinivas, S. Morphological changes in polyamide/pvp blends. *Polymer* **1998**, *39*, 507–516. [CrossRef]
20. Pompe, G.; Mäder, E. Experimental detection of a transcrystalline interphase in glass-fiber/polypropylene composites. *Compos. Sci. Technol.* **2000**, *60*, 2159–2167. [CrossRef]
21. Assouline, E.; Wachtel, E.; Grigull, S.; Lustiger, A.; Wagner, H.; Marom, G. Lamellar orientation in transcrystalline γ isotactic polypropylene nucleated on aramid fibers. *Macromolecules* **2002**, *35*, 403–409. [CrossRef]
22. Shi, H.; Zhao, Y.; Dong, X.; He, C.; Wang, D.; Xu, D. Transcrystalline morphology of nylon 6 on the surface of aramid fibers. *Polym. Int.* **2004**, *53*, 1672–1676. [CrossRef]
23. Hoffman, J.D.; Miller, R.L. Kinetic of crystallization from the melt and chain folding in polyethylene fractions revisited: Theory and experiment. *Polymer* **1997**, *38*, 3151–3212. [CrossRef]
24. Strobl, G. A new approach to polymer crystallization used in an analysis of data of syndiotactic polypropylene. *Acta Polym.* **1997**, *48*, 562–570. [CrossRef]
25. Schoolenberg, G.; Van Rooyen, A. Transcrystallinity in fiber-reinforced thermoplastic composites. *Compos. Interfaces* **1993**, *1*, 243–252.
26. Beehag, A.; Ye, L. Fiber/Matrix Adhesion in Thermoplastic Composite: Is Transcrystallinity a Key. In Proceedings of the Eleventh International Conference Composite Materials (ICCM-11), Gold Coast, Australia, 14–18 July 1997; pp. 723–730.
27. Wu, C.-M.; Chen, M.; Karger-Kocsis, J. Micromorphologic feature of the crystallization of isotactic polypropylene after melt-shearing. *Polym. Bull.* **1998**, *41*, 493–499. [CrossRef]
28. Varga, J.; Karger-Kocsis, J. Interfacial morphologies in carbon fiber-reinforced polypropylene microcomposites. *Polymer* **1995**, *36*, 4877–4881. [CrossRef]
29. Cartledge, H.C.; Baillie, C.A. Studies of microstructural and mechanical properties of nylon/glass composite part i the effect of thermal processing on crystallinity, transcrystallinity and crystal phases. *J. Mater. Sci.* **1999**, *34*, 5099–5111. [CrossRef]
30. Chen, E.J.; Hsiao, B.S. The effects of transcrystalline interphase in advanced polymer composites. *Polym. Eng. Sci.* **1992**, *32*, 280–286. [CrossRef]
31. Huson, M.; McGill, W. The effect of transcrystallinity on the behavior of fibers in polymer matrices. *J. Polym. Sci. Part B Polym. Phys.* **1985**, *23*, 121–128. [CrossRef]
32. Wagner, H.; Lustiger, A.; Marzinsky, C.; Mueller, R. Interlamellar failure at transcrystalline interfaces in glass/polypropylene composites. *Compos. Sci. Technol.* **1993**, *48*, 181–184. [CrossRef]

33. Cartledge, H.C.; Baillie, C.A. Studies of microstructural and mechanical properties of nylon/glass composite part ii the effect of microstructures on mechanical and interfacial properties. *J. Mater. Sci.* **1999**, *34*, 5113–5126. [CrossRef]
34. Folkes, M.; Wong, W. Determination of interfacial shear strength in fiber-reinforced thermoplastic composites. *Polymer* **1987**, *28*, 1309–1314. [CrossRef]
35. Rolel, D.; Yavin, E.; Wachtel, E.; Wagner, H. Experimental study of transcrystallinity in uhmwpe/lldpe composites. *Compos. Interfaces* **1993**, *1*, 225–242.
36. Carvalho, W.S.; Bretas, R.E. Thermoplastic/carbon fiber composites: Correlation between interphase morphology and dynamic mechanical properties. *Eur. Polym. J.* **1990**, *26*, 817–821. [CrossRef]
37. Lopez-Manchado, M.; Arroyo, M. Crystallization kinetics of polypropylene part 4: Effect of unmodified and azide-modified pet and pa short fibers. *Polymer* **1999**, *40*, 487–495. [CrossRef]
38. Klein, N.; Marom, G.; Pegoretti, A.; Migliaresi, C. Determining the role of interfacial transcrystallinity in composite materials by dynamic mechanical thermal analysis. *Composites* **1995**, *26*, 707–712. [CrossRef]
39. Karger-Kocsis, J. Interphase with lamellar interlocking and amorphous adherent—A model to explain effects of transcrystallinity. *Adv. Compos. Lett.* **2000**, *9*, 225–230.
40. Gao, S.-L.; Mäder, E. Characterisation of interphase nanoscale property variations in glass fiber reinforced polypropylene and epoxy resin composites. *Compos. Part A Appl. Sci. Manuf.* **2002**, *33*, 559–576. [CrossRef]
41. Folkes, M.; Hardwick, S. Direct study of the structure and properties of transcrystalline layers. *J. Mater. Sci. Lett.* **1987**, *6*, 656–658. [CrossRef]
42. Assouline, E.; Grigull, S.; Marom, G.; Wachtel, E.; Wagner, H. Morphology of α-transcrystalline isotactic polypropylene under tensile stress studied with synchrotron microbeam X-ray diffraction. *J. Polym. Sci. Part B Polym. Phys.* **2001**, *39*, 2016–2021. [CrossRef]
43. Schultz, J.; Nardin, M. Interfacial adhesion, interphase formation and mechanical properties of single fiber polymer-based composites. In *Controlled Interphases in Composite Materials*; Springer: Dordrecht, The Netherlands, 1990; pp. 561–567.
44. Teishev, A.; Marom, G. The effect of transcrystallinity on the transverse mechanical properties of single-polymer polyethylene composites. *J. Appl. Polym. Sci.* **1995**, *56*, 959–966. [CrossRef]
45. Folkes, M.; Hardwick, S. The mechanical properties of glass/polypropylene multilayer laminates. *J. Mater. Sci.* **1990**, *25*, 2598–2606. [CrossRef]
46. Mäder, E.; Grundke, K.; Jacobasch, H.-J.; Wachinger, G. Surface, interphase and composite property relations in fiber-reinforced polymers. *Composites* **1994**, *25*, 739–744. [CrossRef]
47. Zhandarov, S.; Mäder, E. Characterization of fiber/matrix interface strength: Applicability of different tests, approaches and parameters. *Compos. Sci. Technol.* **2005**, *65*, 149–160. [CrossRef]
48. Mäder, E.; Mörschel, U.; Effing, M. Quality assessment of composites. *JEC Compos. Mag.* **2016**, *102*, 49–51.
49. Brodowsky, H.M.; Jenschke, W.; Mäder, E. Characterization of interphase properties: Microfatigue of single fiber model composites. *Compos. Part A Appl. Sci. Manuf.* **2010**, *41*, 1579–1586. [CrossRef]
50. Mäder, E.; Gao, S.-L.; Plonka, R.; Wang, J. Investigation on adhesion, interphases, and failure behavior of cyclic butylene terephthalate (cbt®)/glass fiber composites. *Compos. Sci. Technol.* **2007**, *67*, 3140–3150. [CrossRef]
51. Brodowsky, H.M.; Jenschke, W.; Mäder, E. Characterization of interphase properties by frequency-dependent cyclic loading of single fiber model composites. *J. Adhes. Sci. Technol.* **2010**, *24*, 237–253. [CrossRef]

MDPI
St. Alban-Anlage 66
4052 Basel
Switzerland
Tel. +41 61 683 77 34
Fax +41 61 302 89 18
www.mdpi.com

Fibers Editorial Office
E-mail: fibers@mdpi.com
www.mdpi.com/journal/fibers

MDPI
St. Alban-Anlage 66
4052 Basel
Switzerland

Tel: +41 61 683 77 34
Fax: +41 61 302 89 18

www.mdpi.com

ISBN 978-3-03936-915-7